# Modeling, Optimization and Hardware-in-Loop Simulation of Hybrid Electric Vehicles

By

Ehsan Tara

A thesis submitted to the Faculty of Graduate Studies of
The University of Manitoba
in partial fulfilment of the requirements for the degree of

Doctor of Philosophy

Department of Electrical and Computer Engineering
University of Manitoba
Winnipeg, Manitoba

December 2012

# Abstract

This thesis investigates modeling and simulation of hybrid electric vehicles with particular emphasis on transient modeling and real-time simulation. Three different computer models, i.e. a steady state model, a fully-detailed transient model and a reduced-intensity transient model, are developed for a hybrid drive-train in this study.

The steady-state model, which has low computational intensity, is used to determine the optimal battery size and chemistry for a plug-in hybrid drive-train. Simulation results using the developed steady state model show the merits of NiMH and Li-ion battery technologies. Based on the obtained results and the reducing cost of Li-ion batteries, this battery chemistry is used throughout this research.

A fully-detailed transient model is developed to simulate the vehicle behaviour under different driving conditions. This model includes the dynamics of the power train components such as the engine, the power-electronic converters and vehicle controllers of all levels. The developed transient model produces an accurate representation of the drive-train including the switching behaviour of the power electronic converters.

A reduced-intensity transient model (also referred to as a dynamic average model) is developed for real-time hardware-in-loop simulation of the vehicle. By reducing the computational demand of the detailed transient model using averaging techniques, the reduced-intensity model is implemented on a real-time simulator and is interfaced to an external subsystem such as an actual battery.

The setup can be used to test existing and emerging battery technologies, which may not have an accurate mathematical model. Extensive tests are performed to verify the accuracy and validity of the results obtained from the developed hardware-in-loop simulation setup.

# Acknowledgments

I would like to express my warmest thanks to my advisor and my friend, Professor Shaahin Filizadeh, for his excellent guidance, care, patience, encouragement and support in my studies, work, and personal life.

I would like to thank Professor Gole who was always very supportive to me. He has definitely a great role in strengthening friendships within the power systems group by gathering students and staff for interesting conversations in coffee breaks.

I would like to thank my examining committee members, Prof. Mi, Prof. Gole, and Prof. Anderson who have taken the time to go through my thesis and have given me valuable feedbacks to improve it.

I wish to express my appreciation to Dr. Shahidinejad for his help, support, and brilliant ideas for this research.

I owe my deepest gratitude to my lovely parents and brothers (Amin and Hamed) who constantly supported me in my life, provided all the means for me to succeed, put up with my absence, and always encouraged me to excel.

Finally, I am grateful to my dear wife, Maryam, for her true love, for being beside me during hard moments and for her encouragements and supports. Without her help and encouragement, this study would not have been completed.

*To*

*My Beloved Parents*

*and*

*My Dear Maryam*

# Table of Contents

# List of Figures

# List of Tables

# Chapter 1

# Introduction

The transportation industry has revolutionized the way people travel every day. In less than two centuries, travelling on horseback on unpaved terrain has been replaced with traveling in modern vehicles on highways that connect distant places. It has also changed the size of cities significantly. With faster and more comfortable transportation, cities have expanded. This has changed the life style of many city dwellers.

Transportation industry as a whole is a massive entity. The number of vehicles in operation worldwide surpassed one billion units in 2010 [1]. It is also predicted that this number increases to 2.5 billion by 2050 [2]. More than 9 million people around the world work directly in manufacturing vehicles and their parts to meet the demand of more than 60 million new vehicles every year. By adding the number of indirect jobs related to the automotive industry, such as service and maintenance, sales and service, etc., the automotive industry is supporting more than 50 million jobs, which makes it one of the most important economic sectors in the world [3].

Modern transportation is a result of continued effort of many scientists, engineers and workers whose collective effort has made traveling a pleasant experience. More importantly, the transportation industry supports the backbone of economy in the modern world, where goods, materials, and manufactured products are constantly in transit.

Since its introduction, the automotive industry has essentially relied on fossil fuels. Serious issues such as diminishing oil supplies and air pollution are increasingly challenging the present state of the automotive industry. Researchers constantly seek ways to overcome these issues and make less consuming, less polluting and more environmentally friendly vehicles, to allow them to continue to provide the service the society has come to depend on so heavily.

In pursuit of cleaner transportation, developing all-electric vehicles is the ultimate goal. Using electricity allows making zero-emission vehicles and also eliminates gas consumption in the vehicle. However current all-electric vehicles lack high energy battery packs with fast-charge ability. This has limited the all-electric vehicle market at the present time. However, hybrid-electric vehicles and plug-in hybrid-electric vehicles are successful interim vehicle technologies. Using (plug-in) hybrid electric vehicles, the efficiency of the drive-train is significantly improved significantly and the range of the vehicle is also extended. The driver is not limited by the battery technology limitations and at the same time benefits from the advantages of electric vehicles. The research presented in this thesis contributes to the improvement of hybrid vehicles by developing techniques and algorithms for their enhanced modeling, simulation and optimization.

This chapter continues with a brief history of the automotive industry. It shows how the primary means of transportation of the past evolved into today's modern transportation industry. It also shows how electric vehicles appeared in the early era of automobiles, how they vanished and how they have returned to the scene.

After a brief history, the important challenges modern transportation is facing today are explored. It is also shown that hybrid-electric vehicles, plug-in hybrid vehicles and eventually all electric vehicles are viable solution for these difficulties.

The motivations and goals of this thesis are described in the last section of this chapter. This section also highlights the steps taken to complete this research and outlines the remaining chapters of the thesis.

## 1.1 History of the Automobile

### 1.1.1 Steam-Engine Powered Vehicle

History of the automobile dates back to 1769 when the first steam-engine powered vehicle was introduced in Britain [4]. Steam-engine powered vehicles became more popular and widely accepted in the late 1780's. Stanley Steamer was a steam-engine powered vehicle with an outstanding success. This vehicle could reach speeds of more than 200 km/h and was easy to operate [5]. Although internal combustion engine vehicles and even primitive electric ones existed, they had poor performance and could not compete with steam-engine vehicles.

Despite its relative success and popularity, the steam-engine powered vehicle had several disadvantages. The steam-engine took a while to warm up and there were always concerns of boiler explosions. Moreover carrying enough water for long trips was virtually impossible, which implied short operating range and therefore limited use in long-haul transportation. These disadvantages pushed engineers to develop more convenient and reliable vehicles.

### 1.1.2 Electric Vehicles

Electric vehicles have a history as long as other types of vehicles. In fact they appeared in early 1890's; they however disappeared quickly because they were not able to compete with their competitors in terms of performance.

The first electric vehicle was built by Gustave Trouvé in 1881. It was a tricycle powered by a small dc motor fed by lead–acid batteries [6]. The creation of this vehicle was then followed by the development of more electric vehicles using larger electric motors and battery packs. Improvements in batteries and electric motors made electric vehicle one of the vehicles of choice between 1900 and 1905. However the limited speed and travel range of these vehicles failed the attempts to keep them in the market. Immature battery technology contributed the most to the failure of electric vehicles.

### 1.1.3 Internal Combustion Engine Powered Vehicles

In 1806 François Isaac de Rivaz built an internal combustion engine (ICE) powered by an oxygen and hydrogen mixture. More engines were developed after that and they all used gas fuel rather than the liquid fuel commonly used today.

Around 1870, Siegfried Marcus built a simple vehicle using a liquid-fuelled ICE. This was the first vehicle that used gasoline as the fuel. The ICE was then perfected by Gottlieb Daimler, Karl Benz, Wilhelm Maybach, and Rudolf Diesel during 1870's; but this engine was still noisy, shaky and difficult to start and could not compete with steam-engine powered vehicles and electric vehicles. More developments and marked improvements in ICE-powered vehicles finally shifted the market towards these vehicles,

and inevitably led to the demise of other technologies that had a much slower rate of improvement. ICE-powered vehicles set out to dominate the market for almost a century.

### 1.1.4 Modern Electric Vehicles

ICE powered vehicles started to offer better performance and reliability than their competitors in the early 1890s. Offering more advantages than any other vehicle, they have since dominated the market and hence stayed as the mainstream vehicle.

Although ICEs can meet the demands of the automotive industry in terms of performance, other factors are pulling back the electric vehicles to the market. The increasing price of oil and concerns about air pollution are the main reasons of returning to electric vehicles as described later in this chapter.

The era of modern (hybrid-)electric vehicles started by introducing the first hybrid electric vehicles, the Toyota Prius in 1997 and Honda Insight in 1999. Other car manufactures joined this movement towards electric vehicles, and today consumers have a handful of hybrid, plug-in hybrid and all-electric options from nearly every major manufacturer.

## 1.2 Modern Transportation Issues

Diminishing oil supplies, environmental pollution and greenhouse gas emissions are the main concerns for policymakers and the resulting policies push the related industries towards developing less consuming and more environmentally friendly products. Among all industries, transportation industry, and road transportation in particular, highly relies on fossil fuels and also produces the largest amount of greenhouse gases [7]. To

overcome these issues, the transportation industry has to go through fundamental changes in vehicular technologies. The changes will affect not only the energy sources that are used to provide energy, but also the design of the drive-trains.

Internal combustion engines have been the main type of power conversion unit in vehicles for many decades. These engines are inefficient and produce significant emissions, which intensify the concerns over long-term availability of oil supplies and the pollution caused by their operation.

With the diminishing resources of fossil fuels and escalating levels of pollution and with consideration of the impact of such emissions (e.g. $CO_2$, NOx, etc.) on the global climate change, the transportation industry is at a turning point where significant research and development is being carried out to create new propulsion systems with higher efficiency, less emissions and less reliance on vanishing fossil fuels.

The share of the transportation industry in production of greenhouse gases varies from jurisdiction to jurisdiction; however it is expected that it will hold a major share for all developed regions with sizeable transportation economy. For example, a research done in British Columbia, shows that the transportation industry produces the largest amount of greenhouse gas emissions among all the industries in that province. According to this study, transportation industry makes 37% of the greenhouse gas emissions in BC [7]. This is much higher than the next polluting industry, which has a share of 22%. **Fig. 1.1** shows the share of each industry in greenhouse gas emissions in British Columbia.

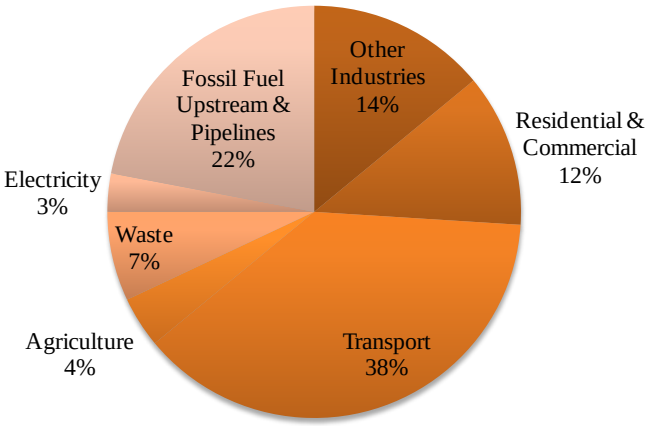


**Fig. 1.1 Greenhouse gas emissions in B.C. by sector in 2005 [7].**

The same study shows that in the transportation sector, road transportation is responsible for 60% of greenhouse gas emissions, which is the largest share among all means of transportation. Therefore, reducing pollution in the transportation sector will have a significant impact on total pollution reduction.

Another problem faced by the transportation industry is the diminishing supply of fossil fuels. **Fig. 1.2** shows the world oil production since 1930. As the trend in **Fig. 1.2** suggests, the declining trend in oil production will continue and there will be no increase in oil production.

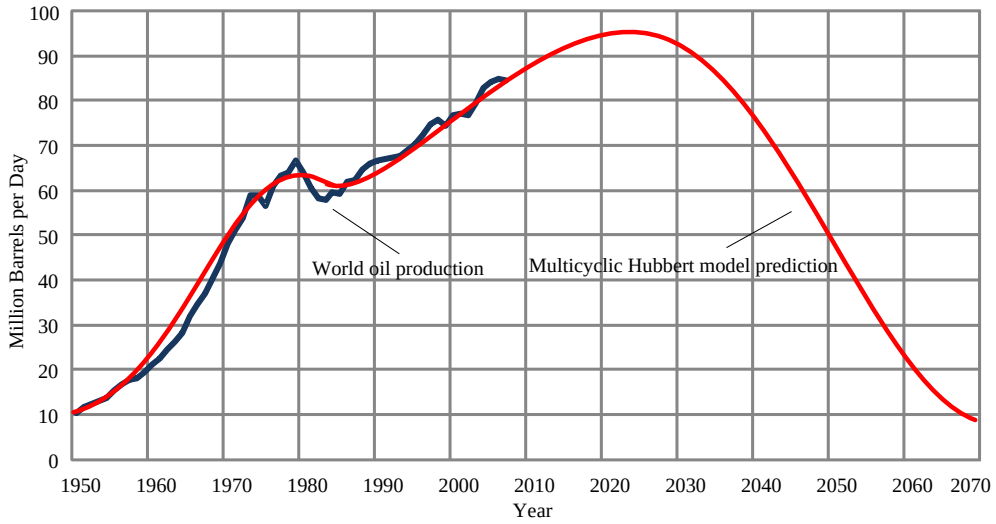


**Fig. 1.2 World oil production since 1950 [8].**

In addition, with the growing world population and growing economies, the demand for oil increases. The trend for oil demand is in the opposite direction of new oil source discoveries. This leads to a severe oil shortage in the near future. In 2006, the worldwide use of petroleum was 80 mbd (million barrels per day), of which 53 mbd was used for transportation as a whole and 29 mbd was used for road transportation [9]. The transportation sector uses a large amount of oil every day; therefore, the shortage of oil will have a serious and crippling impact on this industry. Conversely, if the oil consumption in the transportation sector can be reduced, shortage of oil can be kept under control for a longer period of time until alternative and renewable sources of energy are discovered and their pertinent technologies mature.

## 1.3 Solutions for the Current Transportation Issues

An obvious solution to address both the emissions and fuel consumption due to vehicles is to reduce, or ideally entirely eliminate, the amount of fuel consumed by road vehicles. Several alternative drive-train topologies are presently proposed to achieve improved efficiency and to reduce or eliminate fuel consumption of conventional vehicles. Electric, hybrid and plug-in hybrid vehicles are the most prominent alternatives proposed for conventional vehicles. These drive-train topologies are briefly described in the following sub-sections.

### 1.3.1 All-Electric Vehicles (EVs)

Electric vehicles use electricity as the only source of energy for their propulsion. An All-electric vehicle is therefore the ultimate solution for elimination of the dispersed pollution

caused by vehicles. An all-electric drive-train will have superior efficiency to a conventional gas-powered vehicle, due to the higher efficiency of electrical components such as electric motors and converters, and will have no emissions. However, even with all-electric vehicles, the primary source of energy will likely continue to be, at least for some time, fossil fuels, until renewable sources are developed to fully take over their place. This is because the battery storage of an all-electric vehicle needs to be charged through electricity that will be supplied by power plants using predominantly fossil fuels.

In an all-electric drive-train the electrical energy is stored either in batteries or ultra-capacitors. So far the battery industry has not been able to offer suitable batteries to the automotive industry to allow complete adoption of all-electric vehicles. Batteries for electric vehicles need to provide high *power* to meet the vehicle demand (e.g. during acceleration and deceleration) and they should also have high *energy* density to give the electrical vehicle enough range[1]. Today, batteries are able to meet the power demand of vehicles but their low energy density is still a bottleneck for electric vehicles [6]. This implies that a current all-electric vehicle will be able to match the acceleration of a conventional vehicle but will not have a comparable range. For example, a recently developed all-electric vehicle, Nissan Leaf, has a top speed of 144 km/h, which is comparable to a conventional ICE-powered vehicle in the same class. However its range is limited between 75km to 220km (depending on driving condition) [10]. Conventional ICE-powered vehicles have a range of 500-1000 km. The time required to re-fill the energy storage is another important characteristic of a vehicle. While the gas-tank of a conventional ICE-powered vehicle can be filled within minutes, charging the battery

[1] The range of a vehicle is the distance it travels with a full tank of gas, or with fully charged batteries in case of an electric vehicle.

storage of an electric car requires significantly longer periods. For example, charging the batteries of the Nissan Leaf takes 30 minutes using fast chargers (50kW charger) in dedicated charging stations and 6 hours using an ordinary power outlet (5kW charger).

### 1.3.2 Hybrid Electric Vehicles (HEVs)

An intermediate solution during transition from conventional vehicles to all-electric vehicles is a hybrid drive-train. Particularly, a hybrid-electric vehicle (HEV) combines an electric drive system with a conventional gas or diesel engine to provide propulsion [11]. Improved fuel economy is obtained by eliminating wasteful engine idling, recapturing the kinetic energy of the moving vehicle through regenerative braking, and by using the conventional gas engine in operating points where it is more efficient [12]. This leads to less fuel consumption and less reliance on non-renewable sources of energy for transportation, although it does not lead to its ideal elimination.

In a conventional gas-powered vehicle the engine speed depends on the vehicle speed, as the wheels are mechanically tied to the engine through the transmission system. Therefore, the ICE operates over a wide speed and torque range, which results in efficiencies ranging from 10% to about 30%. **Fig. 1.3** (a) shows efficiency of a typical ICE in different operating points using a graph called the efficiency map. Contour lines show operating points with the same efficiency. Operating points corresponding to a given output power are shown on the map using dark dots. Since the output power is determined by the product of the engine speed (engine rpm) and its developed torque, various combinations of the two lead to the same output power. As this figure indicates, the efficiency for supplying the same amount of power can be as low as 10% or as high

as 30%, depending on the operating engine rpm (determined by the vehicle speed) and its torque.

In a hybrid drive-train the operating point of the engine can be set arbitrarily and independent of the vehicle speed. This is done by storing and extracting energy to and from the on-board battery at appropriate times. **Fig. 1.3** (b) shows how the operating points in lower efficiency regions can be pushed to more efficient regions in a hybrid drive-train.

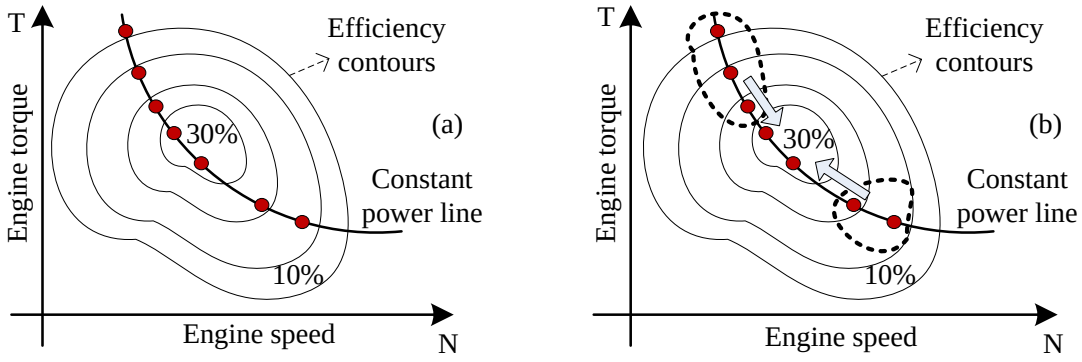


**Fig. 1.3 Operating points of engine in (a) conventional vehicle, (b) hybrid-electric vehicle.**

### 1.3.3 Plug-in Hybrid Electric Vehicles

The next generation of HEV, which is a plug-in HEV or PHEV, is believed to be the most promising platform for the transportation fleet [13], [14] for the foreseeable future. A PHEV is essentially a hybrid electric vehicle with extra electric energy storage that can be charged through direct connection to a utility network [15]. It complements the improved efficiency and fuel economy of an HEV with the possibility of re-charging the vehicle's on-board electric energy storage, and extends the all-electric range of the vehicle. Charging the batteries from an external source enables use of cleaner and more

environmentally friendly energy sources in the vehicle, which results in less polluting and less consuming vehicles.

In an ideal situation where re-charging can be done entirely using electricity produced from renewable sources (e.g. wind) a PHEV is a strong solution for further penetration of renewable energies. Under ordinary circumstances, where charging uses electricity from a combination of renewable and non-renewable sources, a PHEV's extended electric-range offers superior emission and fuel consumption indices to an HEV.

Depending on the method used for generating the electricity in a power network, the overall emissions of a plug-in hybrid may vary. **Fig. 1.4** shows the amount of $CO_2$ emissions for various types of vehicles and different electricity generation types.

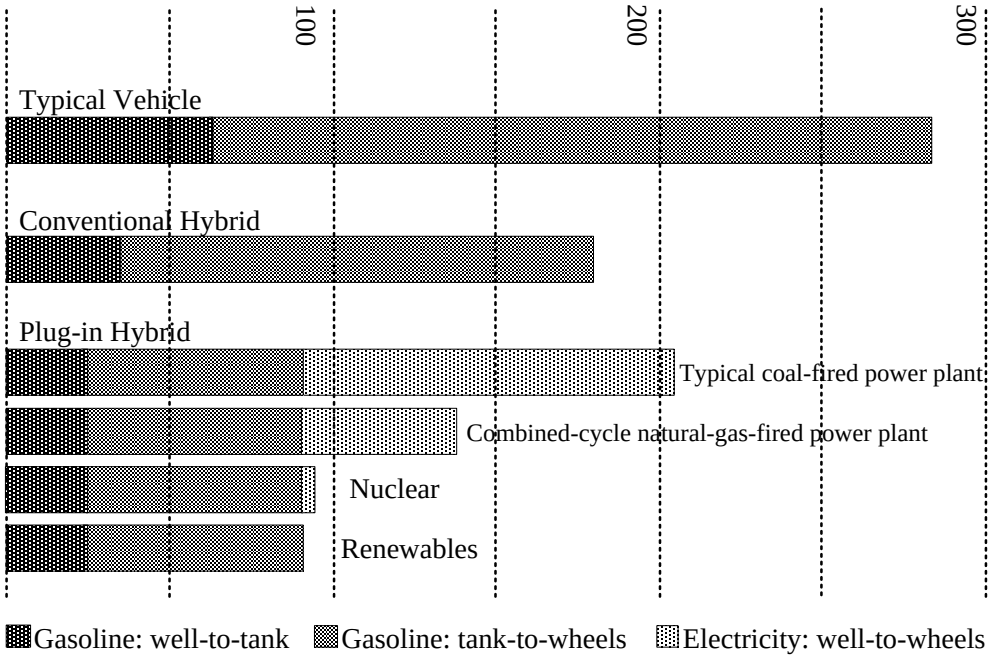


**Fig. 1.4 Well-to-wheel greenhouse gas emissions (grams of $CO_2$ per km) [16].**

A conventional hybrid vehicle has far less overall emissions in comparison with a typical gas-powered vehicle. It also has less emission compared with a PHEV charged

with the electricity generated in a typical coal-fired plant. The PHEV is superior to conventional hybrid when there are less polluting generation stations in the power grid such as combined cycle, nuclear or renewable plants.

PHEVs are emerging technologies and are expected to gain more popularity particularly with the increasing appeal of renewable energies. A promising aspect of a PHEV is that it can be adopted for both existing HEVs (in a retrofit design) or for an entirely new design.

## 1.4 Objectives of the Research

The primary objective of this thesis is to develop an HIL simulation setup for plug-in hybrid electric vehicles. Actual batteries are utilized in this setup and an amplifier interfaces batteries with the drive-train model inside a real-time simulator. Several intermediate research questions, however, had to be answered before. The subordinate objectives are listed below.

The first subordinate objective of the research is to have a better understanding of hybrid drive-trains, the flow of energy within the drive-train and also determining the most suitable battery technology and size for a plug-in hybrid electric drive-train. This objective is fulfilled by developing a steady-state model for the drive-train and finding the optimal battery storage chemistry and size for the drive-train as explained later in the next chapter.

To develop the HIL setup, a detailed model of the drive-train is first developed. However the real-time simulator is not able to run this model in real-time. This introduced an intermediate objective to the research that is developing a reduced-intensity

model of the drive-train. This is done using average-modeling technique for the power electronic converters within the drive-train.

### 1.4.1 Steady-State Modeling and Optimal Battery Sizing

A steady-state model can simulate the flow of power within the hybrid drive-train without considering all the details. This gives a good understanding of the drive-train by showing the way that demand power is distributed between the power sources within the drive-train. It is also a good tool to find the optimal battery for the drive-train since the model is not dealing with excessive details and can simulate a long drive in a short time and determine the fuel efficiency of the vehicle.

A steady-state model is developed for a passenger vehicle in the first step. This model mainly addresses the power exchange between different components of the drive-train and gives an estimation of vehicle range for a given driving cycle. This model is then used to determine the optimal component sizes of a drive-train.

Any study of a vehicular system requires knowledge of the intended use of the vehicle, which is typically given as a driving cycle. Given the statistical variations in the way users operate their vehicles, statistical analysis of a design becomes an important consideration. In this thesis, a statistically derived driving cycle is used. Driving profiles are gathered by installing GPS units on 30 vehicles over one year; these driving profiles are then combined using statistical techniques to produce two average driving cycles, one repressing a typical weekday commute and one for weekend (see Appendix A for details). The weekday and weekend cycles are then augmented to form a weekly driving cycle. Derivation of this driving cycle is done by a team of researchers from the University of Winnipeg in collaboration with researchers from the University of

Manitoba. The steady-state modeling and the driving cycle are explained in Chapter 3 of this thesis.

### 1.4.2 Hardware-in-Loop Simulation

Modeling the drive-train requires modeling of different elements in the system. This includes the electric machines, combustion engine, gear box, batteries, chargers, etc. Accurate mathematical models for almost all of the drive-train components are accessible. The major problem in vehicle modeling is developing an adequately accurate, yet computationally moderate, model for the battery. A battery is an electrochemical device and does not have a precise mathematical model with modest computational intensity. Battery models normally include look-up tables [17] to store variations of the internal voltage and resistance with variables such as temperature and battery state of charge; these models are not able to accurately represent the battery behaviour during transient states. For this reason, in this research a hardware-in-loop system is developed, which uses real batteries outside the simulation environment. A four quadrant power amplifier is used to sink and source power to/from a battery pack. The battery pack used in HIL simulation is a scaled down pack. This is to eliminate working with high voltages and limiting the size and cost of power amplifier. Using this technique the inaccuracy of battery modeling will be eliminated and will not have any adverse effect on the results of the simulation.

A detailed model for the vehicle is first developed. The model includes switching behaviour of the power electronic converters. Although this model is the most accurate to be used in an HIL setup, it is too detailed for the real-time simulator to simulate in real-time. Therefore, a reduced intensity model is developed for the drive-train using averaged

modeling technique as described in Chapter 5. The reduced intensity model is implemented in Opal-RT real-time simulator. The simulator is interfaced with a four quadrant amplifier, which is connected to a battery pack. The amplifier can provide/ absorb power to/from the battery to simulate the driving condition simulated within the simulator.

## 1.5 Thesis Outline

This chapter presented a review of the benefits and limits of hybrid electric and plug-in hybrid electric vehicles. Chapter 2 gives a technical view to the commonly used hybrid-electric drive-train topologies and presents advantages and disadvantages of each topology.

Converting a hybrid vehicle to a plug-in hybrid vehicle is known as retrofitting hybrid vehicles. In Chapter 3 a backward steady-state model for Toyota Prius is developed. Using this model, retrofitting the vehicle using different battery technologies is studied and optimal size of battery storage for different battery technologies is determined.

A detailed model of the drive-train is developed in Chapter 4. This model is used to model the transients of the drive-train which are neglected in the steady-state model. The transient model can also be used to model the vehicle in real-time to make a hardware-in-loop setup. The model is developed in Opal-RT real-time simulator. The simulation is then connected to the hardware using I/O board to make a hardware-in the loop (HIL) setup. The HIL setup and results of the studies carried out using it are described in Chapter 6.

# Chapter 2

# Hybrid and Plug-in Hybrid Drive-Trains

Hybrid-electric drive-trains consist of an internal combustion engine (ICE), electric machines (motor and generator), a battery pack and power electronic converters that interface various electrical components of the system and provide control of the power flow, and a gearbox that provides the mechanical connection of electric machines and the engine. There are, however, various ways these components can be arranged and interfaced to form a working drive-train [18], [19].

There are two basic templates for hybrid-electric drive-trains, namely the series and the parallel configurations [20]. More complex drive-train topologies can be obtained by combining properties from these two templates [21]. A combined drive-train, known as the power-split gear (PSG) [22], is widely used in commercially available hybrid electric vehicles. In the next three sections these different drive-train topologies, their characteristics, advantages and limitations are discussed.

## 2.1 The Series Drive-Train

In the series drive-train topology, propulsion is provided entirely by the electric motor(s) [6]. The energy required to operate these electric motors is primarily provided by an on-board battery pack. Since a battery can only store a limited amount of energy, an on-board internal combustion engine is included to charge the battery and to provide

additional power for propulsion when the state-of-charge of the battery does not allow its sole engagement in supplying power to the wheels. A generator is coupled to the ICE to convert its output power to the electric power required for charging the battery through an intermediate power electronic converter. **Fig. 2.1** shows the series drive-train topology. Arrows on the figure show the direction of the power flow among various components of the system during the operation of the vehicle. The normal direction of the power flow is from the energy storage or the engine/generator path to the wheels. White arrows in this figure show the normal direction of power flow. However during braking periods, the energy can also be removed from the wheels and be re-directed into the batteries. This mode of operation is called regenerative braking and is a major advantage of hybrid electric vehicles over conventional gas-powered ones, in which the kinetic energy of the moving vehicle is dissipated as heat during braking periods [23]. In the regenerative braking mode, the electric machines mechanically connected to the wheels will operate as generators and the wheels operate as their prime mover. This direction of power flow in this mode is shown using shaded arrows in **Fig. 2.1**. A converter makes this recovered energy suitable for energy storage by converting (e.g. from ac to dc, if necessary) and by providing controlled voltage.

Using the series topology the combustion engine is mechanically decoupled from the wheels. This allows the engine to operate in the narrow high-efficiency region of its efficiency map, which in turn improves the overall vehicle efficiency [24]. The series drive-train has simple structure and easy packaging (generator, batteries and electric motor are connected by electrical cables). The traction torque comes from an electric motor, which has ideally suited torque-speed characteristics and eliminates the use of multi-gear transmission or variable gear ration transmission systems [18]. Using electric

motors for propulsion also makes implementing the control strategies easier. For example in case individual motors are installed for each wheel, the conventional differential can be replaced by an electronic differential [25].

The other benefit of the series drive-train is that a relatively small combustion engine can be used.

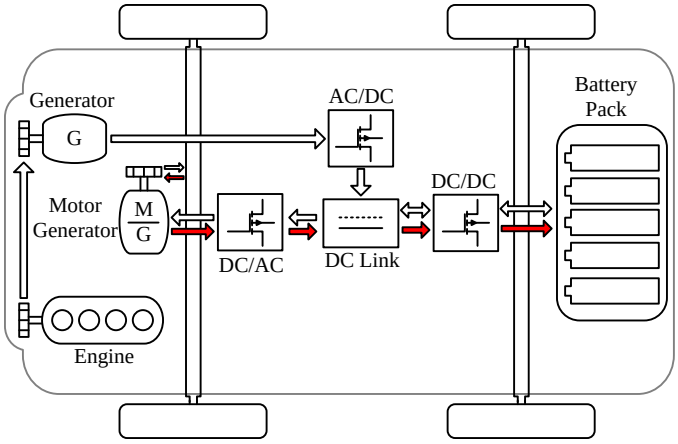


**Fig. 2.1 Series drive-train topology.**

The sizing of the combustion engine for a vehicle is usually based on the desired acceleration of the vehicle. Since the power demand during acceleration is far higher than what is required to maintain a given speed, the combustion engine size will be larger than what is necessary for normal driving conditions. Its extra power is needed for acceleration periods only. In a series drive-train, the combustion engine does not need to be oversized since it does not directly provide power for the wheels. Therefore, the series drive-train needs a small combustion engine, which is operated in close vicinity of its optimal operating point. The electric motor is the source of propelling force. Electric motors are easy to control and their characteristics better fit vehicular needs. This also results in a less complicated mechanical transmission system. On the other hand,

converting energy from mechanical to electrical form and back again to mechanical introduces higher losses in the converter stage, which can result in some loss of efficiency in the series drive-train. Therefore in the series drive-train the compromise is between improved efficiency due to operating the engine at an efficient point and the loss of efficiency due to power conversion from mechanical in the engine to electrical in the energy storage and again back to mechanical to the wheels.

The problem of efficiency reduction in a drive-train due to power conversion is addressed in some drive-train topologies using a torque coupler. A torque coupler is a mechanical device that allows part of the mechanical power to flow directly to the wheels. This direct flow of mechanical power mitigates the losses introduced in the system by repeated power conversions. A basic drive-train that incorporates the idea of using a torque coupler is the parallel drive-train and is described next.

## 2.2 The Parallel Drive-Train

The parallel drive-train provides two paths for the energy to flow the wheels [26]. The first path is a mechanical one in which the engine power goes directly to the wheels without being converted to electrical power. The second path is an electrical one, where mechanical energy is first converted to electrical by a generator. This energy is either stored in the battery pack or immediately converted back to mechanical to propel the vehicle using an electric motor. The electric motor and the internal combustion engine are coupled by means of a torque coupler that adds up the torque components provided by each. The resulting torque is delivered to the wheels for propulsion.

**Fig. 2.2** shows a conventional parallel hybrid drive-train topology. Note that in the parallel drive-train, the flow of energy can be directly from the engine to the wheels (white arrows). However a portion of this flow can be directed to the battery packs and be stored (shaded arrows). It is also possible to use the stored energy in the batteries for propulsion using the electric motor and the torque coupler [23].

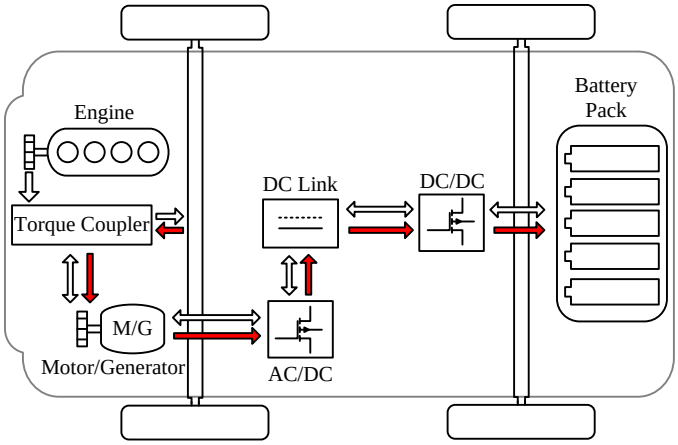


**Fig. 2.2 Parallel drive-train topology.**

Regenerative braking is also possible in this topology by operating the electric machine in the generator mode [27]. This absorbs power from the wheels and stores it in the battery pack. Note that this power is entirely dissipated as heat in a conventional internal combustion engine-based vehicle. Its re-storage in the battery pack adds to the overall efficiency of the drive-train.

Fewer steps of power conversion from one form to another in the parallel drive-train result in a higher efficiency compared to a series one [18]. This advantage is achieved by sacrificing the ability to choose the ICE's operating point freely, which may result in a lower efficiency for some operating conditions. Moreover, introducing the torque coupler makes the mechanical design of the system more complicated [24]. Therefore, in

selecting one drive-train between the series topology and a parallel one, the compromise is between operating the engine at the best efficiency point versus fewer stages of energy conversion. In some driving conditions, the series drive-train offers better efficiency and less fuel consumption while in some other driving conditions the parallel is superior. For example, in a city driving cycle with long idling times, a series configuration works better. Under these conditions, the series drive-train provides most of the required energy from the battery pack and if the driving cycle is not too long, it is likely that the vehicle works in all-electric mode only. The engine starts running if the battery-state-of-charge goes low. The engine will work in its most efficient operating point to charge the batteries.

Parallel topology is superior in highway driving conditions. Highway driving requires large amounts of power and energy and engaging engine is necessary. Parallel drive-train has more efficiency compared with series drive-train since the engine power directly goes to the wheels rather than being converted back and forth between mechanical and electrical types, which is the case in the series topology.

However, using combined drive-trains [24] the benefits of both basic topologies can be realized. The *power-split gear* (PSG) drive-train is a combination of the series and parallel drive-trains and offers benefits of both [28].

## 2.3 The Power-Split Gear Drive-Train

Series and parallel templates are basic drive-trains that have been modified by different manufactures to best fit a particular vehicle. Toyota Prius, for example, utilizes a

combined drive-train known as power-split gear drive-train[1] [29], [30].This drive-train is neither entirely series nor parallel but offers the benefits of both through the use of a power-split gear (PSG).

A power-split gear system is a three gear device, which connects the internal combustion engine, an electric motor and an electric generator together. **Fig. 2.3** shows a cross sectional view of a power-split gear system.

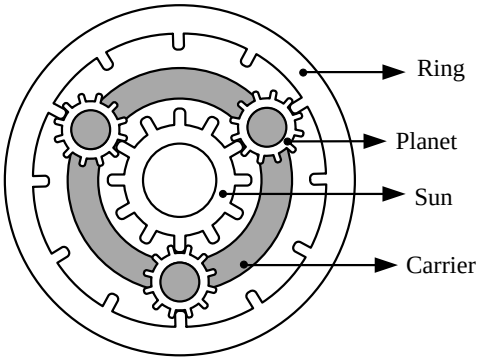


**Fig. 2.3 Cross-sectional view of a power-split gear.**

The outer gear is called the ring, which is connected to an electrical machine in a power-split gear drive-train. The ring is also coupled to the wheels through an additional gear and the differential. The inner gear is called the sun, and is connected to another electrical machine in the drive-train. The middle ring, which carries three smaller gears known as planets, is called the carrier and is connected to the ICE in the drive-train and transfers power to the sun and the ring though planet gears [31]. A detailed description of the PSG is given in Chapter 4, where its modeling is described.

**Fig. 2.4** shows connections between components in a power-split gear drive-train. Arrows on this figure show the flow of power within the drive-train. The internal

[1] Also known as Toyota Hybrid System (THS)

combustion engine (ICE), motor-generator 1 (MG1) and motor-generator 2 (MG2) are coupled together by means of a power-split gear system. MG2 provides propelling force for the vehicle in all-electric driving mode. MG2 also assists the engine when the engine power is not adequate for providing the propulsion force. This is called the electric-assist mode of operation of the drive-train.

MG1 is used to charge the on-board battery pack and also to provide power for MG2. MG1 and MG2 are connected to a common dc bus using power-electronic converters. Another converter is used to connect the on-board battery to the common dc bus. The voltage of the dc bus is usually higher than the battery terminal voltage, thus a bidirectional dc/dc converter is used to boost the battery voltage to the dc bus level.

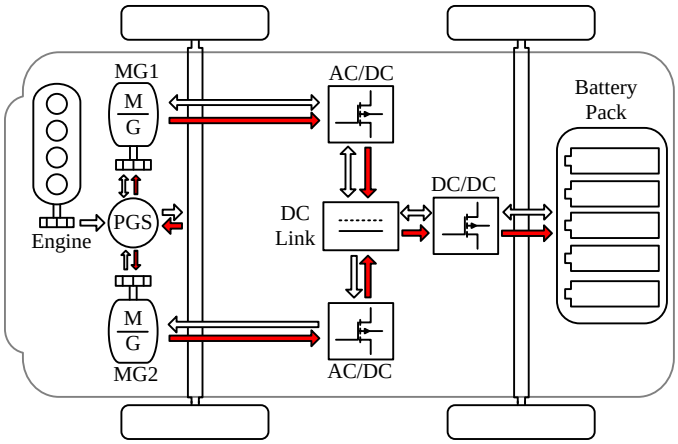


**Fig. 2.4 Power-split gear drive-train.**

The power-split gear drive-train combines the benefits of the series and the parallel topologies. In this drive-train, the engine is coupled to the wheels by means of a power-split gear system. This mechanical connection resembles the parallel drive-train topology. The power-split system delivers part of the engine power directly to the wheels and eliminates repetitive power conversion from one form to another. This method of vehicle

propulsion is similar to the one deployed in the parallel drive-train using a torque coupler. Additionally in this drive-train one can change the operating point of the internal combustion engine (for example to its optimal-efficiency point) by changing the operating point of MG1; a property that is unavailable in the parallel template. This characteristic of the power-split drive-train resembles the main benefit of a series drive-train, which increases the drive-train's overall efficiency and improves the vehicle range. The benefits of the power-split drive-train make it a suitable option for commercially available hybrid vehicles and future hybrid and plug-in hybrid vehicles [15]. Therefore, this topology is selected for modeling, simulation and studies done in this thesis.

## 2.4 Plug-in Hybrid Drive-Trains

A plug-in hybrid drive-train is similar to a conventional hybrid drive-train with a larger battery pack. The fundamental difference between a hybrid drive-train and a plug-in hybrid drive-train is the capability of a plug-in hybrid drive-train to charge its battery storage from an external electric source, e.g. utility network.

There are two types of plug-in hybrid vehicles on the road. The first type is the one that is manufactured as a plug-in hybrid drive-train. This type has one battery pack that can be charged either using the internal energy source, i.e. the combustion engine, or by plugging the vehicle.

The second type is the retro-fitted plug-in hybrid vehicle. These vehicles are manufactured as hybrid electric vehicles and are then converted to plug-in hybrid cars by third party companies or individuals. These vehicles usually have two battery storages onboard, the internal and the external battery packs. The internal battery storage is the

one installed by the original manufacturer. It is charged using the onboard generator and does not accept charge form an external energy source. The external battery storage is the one installed in the retro-fitting process. It can provide power to the drive-train, but accepts charge only from an external source, i.e. from the plug [32]. This research mainly addresses the hybrid drive-train. However both plug-in drive-trains can also be modeled and studied with minor changes to the models developed in this thesis.

In chapter 3 to study different battery technologies, a retro-fitted power-split gear-based plug-in hybrid drive-train is studied. The drive-train uses two battery packs, namely the internal and the external ones. The internal battery storage unit is identical to the on-board battery storage in a hybrid drive-train. It can be charged using the on-board generator and also through regenerative braking. The external battery pack, on the other hand, is the extra battery storage, which can be charged only by plugging the vehicle in. This extra battery storage improves the range and efficiency of the vehicle.

# Chapter 3

# Steady-State Modeling of Vehicular Systems

## 3.1 An Overview of Vehicular Modeling Methods

Drive-train modeling is an essential step in studying a vehicle's performance under different conditions and also in finding the optimal sizes of components inside the drive-train. Various modeling approaches are presented in the literature, including steady-state models and physics-based transient models. These modeling techniques are different in the level of details they take into consideration, thus becoming suitable for studies with different objectives. For example, as its name suggests, a steady-state model mainly deals with the steady-state behaviour of the vehicle and its drive-train components [26], [33], [34]. This makes steady-state modeling relatively simple and inexpensive from a computational point of view. Simulation of a steady-state model does not require small time steps, which in turn leads to fast simulations. The results obtained from steady-state models are useful in high-level design of a vehicular drive-train. Sizing of major components, estimation of expected fuel consumption, and selection of a high-level vehicle control strategy are examples of the studies that can be done using a steady-state modeling approach [35]-[37].

Transient vehicular models, on the other hand, provide a detailed representation of the vehicle and the short-term dynamics of its drive-train components. Transient models are mathematically involved and their time-domain simulation requires small time steps,

which leads to time-consuming simulations. This is especially important in hybrid-electric vehicles and plug-in hybrid-electric vehicles, which contain power electronic circuits with fast transients that have to be included in a transient model [38], [39]. Transient simulation results explain the time-domain behaviour of each component and are useful for studying the performance of drive-train components, for example batteries, as well as designing or tuning the drive-train controllers [40]. An important benefit of transient models is that they lend themselves to implementation on real-time simulators, which then allows incorporation of actual hardware components to form a real-time hardware-in-loop (HIL) simulator. This aspect of transient modeling forms a center-piece of this research and will be explored in further detail in Chapter 4.

In this chapter a steady-state model for a retro-fitted plug-in hybrid electric vehicle is developed. This model is then used to find the optimal battery type and size for such a vehicle in an average-size North American city, i.e. Winnipeg. Although there are similar studies in the literature [35], [36], they are all based on standard driving cycles, which do not represent the actual driving conditions. The importance of this study is applying the Winnipeg driving cycle (developed by researchers at University of Winnipeg and University of Manitoba) to find the battery type and size.

Batteries to be tested are Lead-acid, NiMH and Li-ion chemistries. A comparison between NiMH and Li-ion chemistries is presented in [41]. It explains the difference in chemistry, life time, energy and power density, price, environmental impacts and other aspects of the two technologies. It shows that with the prices at the time of the mentioned study (2008), NiMH is a better technology for the electric vehicles. However if the manufacturing cost of Li-ion decreases, it will be better choice for hybrid electric vehicles.

## 3.2 Steady-State Vehicle Modeling Methods

Steady-state vehicle models can also be categorized as forward and backward [33], referring to the way power flow calculation is performed. Forward modeling resembles the actual driving of a vehicle. It starts from the driver and goes all the way to the wheels. A forward model, shown schematically in **Fig. 3.1**, accepts a reference speed as the input. A reference torque is generated in the driver model based on the reference speed to cause the vehicle to reach and follow the desired speed. The driver model is usually a proportional-integral (PI) controller. Controller gains determine the driving habits. Calculated torque is then translated to accelerator and brake pedal commands (positive torque denotes acceleration and negative torque denotes braking), which are sent to the vehicle controller and to all other components afterwards. Therefore, a forward model is useful for studying the performance of the vehicle and the objective of the study is usually more than merely finding the fuel economy. With a forward model, one can observe the performance of the vehicle when the acceleration pedal is pressed. Depending on the level of details in a forward model, one can observe the response of different components within the drive-train. For example, with a fully-detailed transient model, one can study the performance of power-electronic converters and their controllers. If the purpose of study is only the vehicle controller, a less-detailed model will suffice as well.

A backward model conducts the calculations in the opposite direction. It assumes that the vehicle has been driven in a way such that the reference speed is accurately matched. This eliminates the need for the driver model. A backward model discards all the

dynamics of the vehicle due to driving habits of the driver and focuses on the fuel economy.

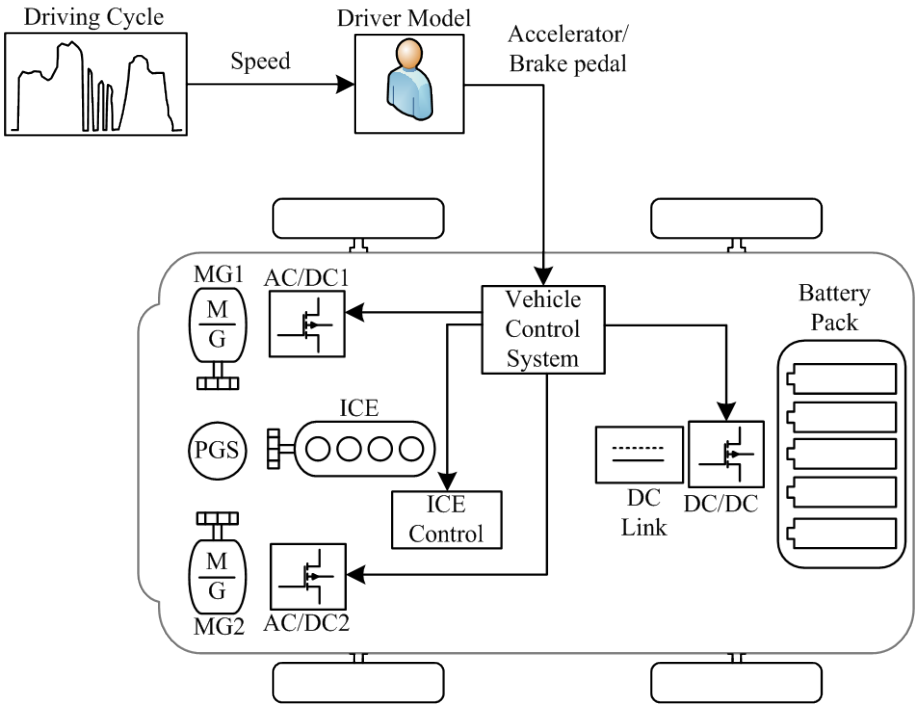


**Fig. 3.1 Forward model diagram.**

A backward model for a PSG drive-train is shown in **Fig. 3.2** [42]. In this figure, speed is the input for the model; based on the speed and parameters of the vehicle the required output power to achieve the speed is calculated in the vehicle controller. This controller then determines the contribution of each source of power in providing the output power based on the driving condition and also other parameters such as state-of-charge of the battery. Vehicle fuel consumption is then determined using these powers and efficiency of different drive-train components.

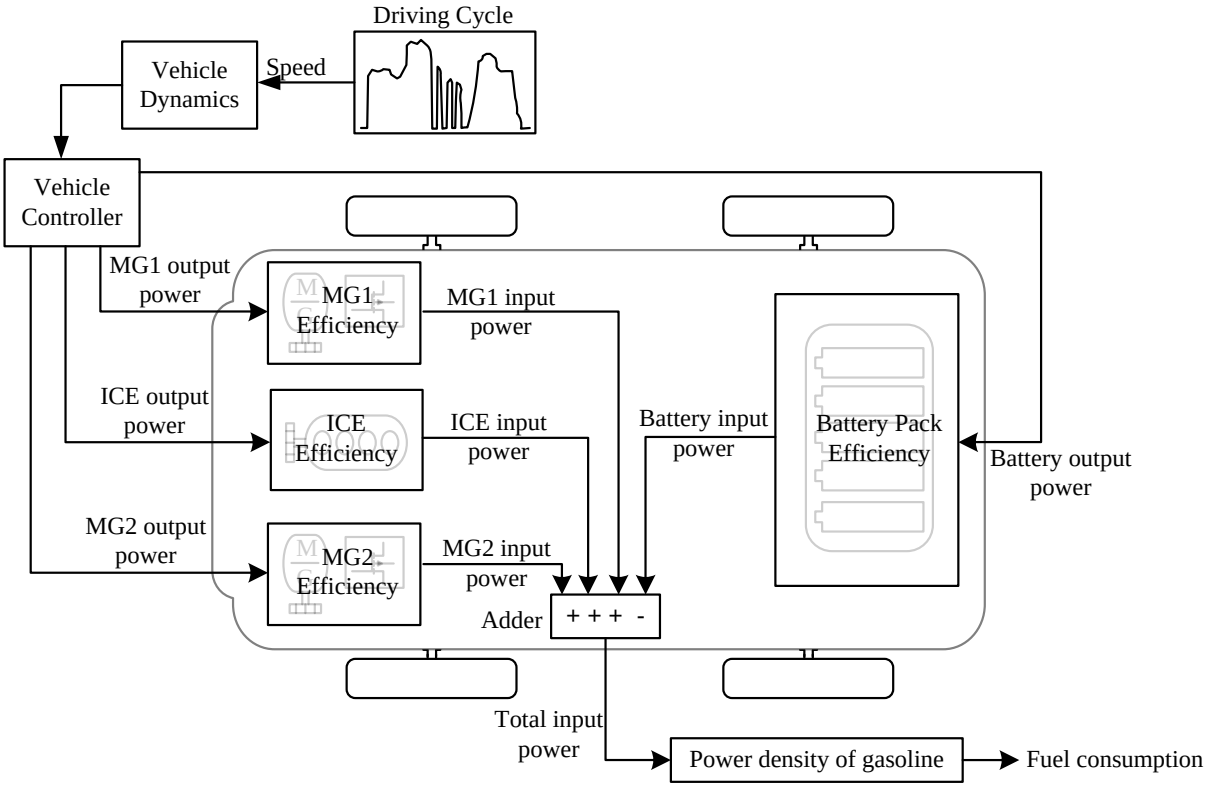


**Fig. 3.2 Backward model diagram.**

A backward model is a computationally fast one that finds the fuel consumption of the vehicle. The simulation speed of this model is achieved by neglecting all dynamics of the system. Backward models are usually used for optimising the size of drive-train components and also evaluation of the fuel consumption of the vehicle under different driving conditions.

In this thesis a backward steady-state model and a forward transient model are developed for a power-split gear drive-train. The steady-state model is able to estimate the range of the vehicle for different driving cycles and for different drive-train component sizing including battery, electric machines and the engine. The objective of the steady-state model is to determine the optimal sizing of the additional battery storage for a retro-fitted plug-in hybrid electric vehicle. This model can also be used in order to

find the optimal sizing of the electric machines as well as the combustion engine, although this thesis does not include such studies.

## 3.3 Description of a PHEV Steady-State Model

In this research a steady-state model for a retro-fitted plug-in hybrid electric vehicle is developed in order to find the optimal sizing of the additional battery pack in the drive-train. Since the problem of optimizing the size of the battery pack is related to the efficiency and energy losses within the drive-train over long periods of time (for example over a week or a month) the transient behaviour of the components in the drive-train is not the point of interest. Moreover, unnecessary levels of detail in the model make it computationally intensive and result in time-consuming simulations. Therefore, a steady-state model of the drive-train is developed. In this model, steady-state models for drive-train components are developed and properly interfaced. The model for each component estimates its energy losses and efficiency. In a backward model, each component receives the output power (which the component has to generate in order to follow the driving-cycles) and calculates the required input power. Losses and efficiency for some components such as the power electronic converters are considered to be constant for all operating points while the efficiency of other components, e.g. the internal combustion engine, dynamically changes with the changes in the operating point of the component. Starting from the propelling power required by the vehicle to perfectly follow the driving-cycle and moving backwards, the model calculates the energy taken from each energy source, i.e. gasoline tank, on-board battery pack and external battery pack.

**Fig. 3.3** shows a block diagram of the steady-state model developed in this research. The driving/charging cycle block in this model includes two parts. The driving cycle block provides the pattern of a typical weekly commute. This typical pattern is gathered by UofW and UofM researchers over a period of one year by installing positioning systems (GPS) on the vehicles of 30 volunteers in the city of Winnipeg. Many parameters are then derived based on the collected data. These parameters include average speed over entire driving cycle, average running speed, average acceleration, etc. (refer to Table A-1). Statistical methods are then applied to the collected data in order to derive an average driving cycle for the city of Winnipeg (this driving cycle and its development are discussed in Appendix A of this thesis). This part is done in a different project at the department of mechanical engineering at UofM and the results of this study are used in this thesis.

The charging cycle part of driving/charging block contains the times that the vehicle is plugged. Two scenarios are studied in this research: Overnight charging only and overnight plus opportunity charging. In overnight charging only, the vehicle is plugged only overnight. In the second scenario, the vehicle is plugged overnight plus any other time that the vehicle is parked for more than three hours.

Based on the driving cycle one can calculate the acting forces on the vehicle and the power needed to meet the requirements of the given driving pattern. These calculations are done in the vehicle dynamics block. The mathematical details of the model are presented in Section 3.3.2.

In a power-split gear drive-train, a mechanical and an electrical path deliver the propelling power to the wheels. The power in the mechanical path is provided directly from the ICE and the power in the electrical path originates from either the battery

storage or MG1. The flow of power within the drive-train is controlled by a vehicle controller. It determines the amount of power to be exchanged between different components in the mechanical and electrical paths. Proper power distribution increases the vehicle efficiency and improves battery storage life by eliminating unnecessary charge/discharge cycles. The vehicle controller used in this research is explained in detail in Section 3.3.3.

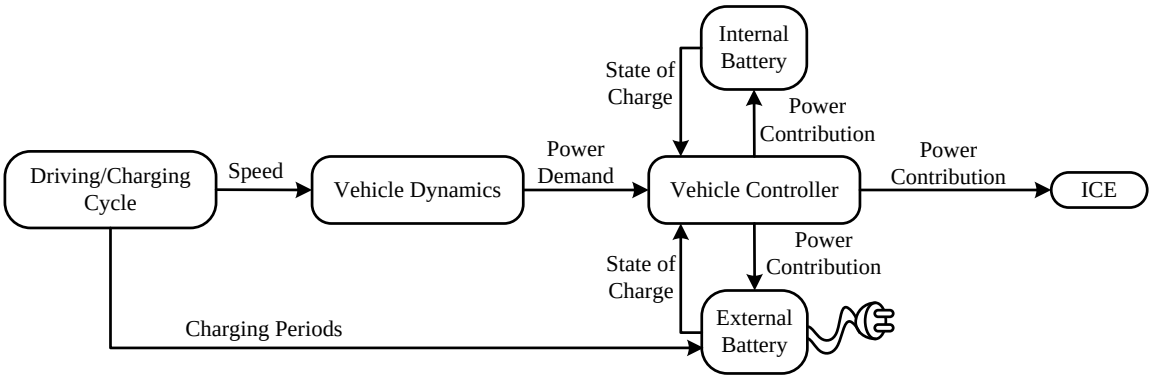


**Fig. 3.3 Block diagram of the developed backward steady-state model.**

The electrical energy storage in the drive-train consists of two battery storage units, i.e. the on-board battery pack and the additional or external battery pack. There are various battery chemistries used in the automotive industry with markedly different characteristics. Three main battery chemistries are the Lead-acid, Lithium ion (Li-ion) and Nickel-metal hydride (Ni-MH). Lead-acid battery is the most inexpensive battery technology and can provide adequate power for vehicular applications. However the weight and size of this type of battery are significant, which limit the application of this battery. It also has relatively small energy density, thus is unable to provide energy for any realistic driving range. Ni-MH batteries offer higher power and energy density compared with the lead-acid type. Therefore a small pack of Ni-MH battery can have the

same performance as a much larger lead-acid battery pack. However the cost of Ni-MH battery is significantly higher than lead-acid type. Li-ion battery storage offers higher energy density compared to the Ni-MH type, although their power density is in the same range. This makes Li-ion batteries more suitable for applications that need a large storage, like plug-in hybrid vehicles and all-electric vehicles. It is however the most expensive battery chemistry. The steady-state drive-train model developed in this thesis is used to study the performance of each battery technology in a plug-in hybrid topology. For this purpose, a steady-state model for the battery is developed. Using proper values in the model, it can represent different battery chemistries. This model is explained in Section 3.3.4.

### 3.3.1 Driving Cycle

A driving cycle represents the variations in the speed of a vehicle over a given period of time. Standard driving cycles are based on statistical data and represent typical driving conditions for specific vehicle types and vehicle usage profiles. For example the urban dynamometer driving schedule (UDDS) represents typical urban driving conditions for a passenger vehicle for a 1369-second driving period [19]. It should be noted that standard driving cycles do not necessarily represent the actual, real-world daily power demand of a vehicle. Similar vehicles can be used in markedly different manners by different drivers according to their daily commute patterns. Another shortcoming of standard driving cycles is that their durations are typically far too short to represent long-term usage profiles, including vital information such as prolonged parking times when grid charging may happen in the case of a plug-in hybrid electric vehicle.

In order to perform modeling in a more realistic manner, actual daily driving profiles for 30 vehicles in the city of Winnipeg have been recorded using GPS loggers. Usage profiles have been recorded for a prolonged period of time to allow detailed analysis of their statistical variations. Enhanced average driving cycles (one for the weekday and one for the weekend pattern) have then been produced that closely match the average of the behaviour of the recorded cycles in terms of a large number of characteristic measures. The recording and analysis of the data has been done by a team of researchers from the University of Winnipeg in collaboration with researchers from the University of Manitoba. By applying statistical methods, a driving cycle for an average driver in the city of Winnipeg is developed. A detailed representation of the methods used to analyze and derive the enhanced average driving cycle is given in Appendix A.

### 3.3.2 Vehicle Dynamics

The vehicle dynamics block in the developed steady-state model calculates the required power to meet the instantaneous driving condition given by the driving cycle. Forces acting upon the moving vehicle are calculated and the demand power to maintain the speed of the vehicle is the output of this block. In a moving vehicle, the most important forces needed to be considered are the propelling force and the resistive forces that include the aerodynamic drag, rolling resistance, and grading resistance [43].

The steady-state model accepts the vehicle speed as the input and calculates various forces based on the speed and vehicle parameters. Vehicle acceleration is calculated using two consecutive samples of speed as follows.

$$a = \frac{v(t) - v(t - \Delta t)}{\Delta t} \tag{3.1}$$

where $a$ is the vehicle acceleration in m/s$^2$, $v$ is the vehicle speed in m/s and $\Delta t$ is the sampling time of the driving cycle in seconds. The propelling force of the vehicle, which is the force required to give the vehicle the above acceleration, is calculated using Newton's second law of motion as follows.

$$F_p = M_v a \tag{3.2}$$

where $F_p$ is the propelling force and $M_v$ is the mass of the vehicle. Acceleration and consequently the propelling force are considered constant between two consecutive speed samples in the driving cycle.

The average speed of the vehicle between two consecutive samples of speed is calculated as follows and this value is considered as the vehicle speed between the two sampling points.

$$V = \frac{v(t-\Delta t) + v(t)}{2} \tag{3.3}$$

where $V$ is the vehicle average speed and $v(t)$ and $v(t-\Delta t)$ are two consecutive speed samples in the driving cycle.

As the vehicle travels in the air, there is a resistive force against its movement. This opposing force is called the aerodynamic drag and depends on the frontal area of the vehicle, the shape of the vehicle, air density, vehicle speed and wind speed. The aerodynamic drag is calculated as follows:

$$F_{ad} = \frac{1}{2}\rho A_f C_D (V + V_w)^2 \tag{3.4}$$

where $F_{ad}$ is the aerodynamic drag force, $\rho$ is the air density in kg/m$^3$, $A_f$ is the frontal area of the vehicle in m$^2$, $C_d$ is the drag coefficient which depends on the shape of the vehicle, $V$ is the vehicle speed and $V_w$ is the wind speed (both in m/s). In this study wind speed is assumed to be zero.

The other opposing force against the movement of a vehicle comes from the tire-road junction. The elasticity of tire causes tire deformation when it rotates. The faster the tire rotates the more deformation the tire will undergo. The deformed elastic material of the tire tends to return to the original shape and this makes an opposing force against the movement of the vehicle. This resistive force is called the rolling resistance and is calculated as follows [6].

$$F_{roll} = C_0(1 + C_1 V) \cdot N \tag{3.5}$$

where $F_{\text{roll}}$ is the rolling resistance, $V$ is the vehicle speed and N is the normal weight on the tire. On an even surface total normal weight on all tires is equal to the weight of the vehicle. ($M_v \times g$). Constants $C_0$ and $C_1$ depend on the vehicle type, road condition and inflation pressure. For a passenger car on concrete road and for most common inflation pressure, these coefficients are both equal to 0.01 [6]. The total required force is the algebraic sum of propelling force and all the opposing forces. Note that the analysis is done with the assumption of moving on a flat and horizontal surface. In case the vehicle is moving on a slope, a component of force, referred to as the road grade, should be incorporated accordingly. Due to lack of slope data for the driving cycle and also considering the fact that data is collected in Winnipeg, which is a fairly flat city, road slope is assumed to be zero for in calculations presented in this thesis. The net force (in the absence of the road grade) is calculated as follows.

$$F_{net} = F_p + F_{ad} + F_{roll} \tag{3.6}$$

where $F_{net}$ is the net required force, $F_p$ is the propelling force, $F_{ad}$ is the aerodynamic drag force and $F_{roll}$ is the rolling resistance force. The power demand is calculated based on the calculated forces and the vehicle speed as follows.

$$P_{demand} = F_{net} \cdot V \tag{3.7}$$

In this equation, $P_{demand}$ is the demand power, $F_{net}$ is the net force applied to the vehicle (3.6) and $V$ is the vehicle speed (3.3).

The calculated power demand is sent to the vehicle controller. The vehicle controller determines the contribution of different sources of power, i.e. electrical motor and the ICE in providing the demand power. Different distribution of power between the two sources affects the vehicle performance and efficiency.

### 3.3.3 The Vehicle Controller

At every point on a driving cycle, the power demand of the vehicle must be met by the engine, the electrical motor or a combination of both. Distributing the demand power between different sources of power, i.e. the electrical motor and the combustion engine, is done by an on-board control system, known as the vehicle controller. The vehicle controller decides how much power should be supplied from the electrical part of the drive-train and how much should be supplied from the engine in order to achieve the best overall efficiency and to meet the driving condition at the same time. In the power-split gear drive-train considered in this study, it is assumed that the electrical motor and the engine work independently and their power is added up using a power-split gear device [30].

Commercially available hybrid vehicles all use proprietary vehicle controller algorithms, which are not made available to the public. Generally, distribution of power can be done in multiple ways. The vehicle controller can be designed in such a way to use either the electricity (i.e. the electrical path) or the fuel (i.e. the ICE path) as the main source of energy. Due to energy limitations of the on-board batteries, the period of time where the electrical path can be used as the sole source of energy, i.e. the all-electric mode of operation, is often limited. This implies that the ICE path must be deployed to provide the required propulsion power as well as the power to re-charge the batteries. Therefore the electrical source has to be deployed in a way that results in better efficiency and longer range.

The expression used for the vehicle controller logic in this study is given in (3.8)-(3.10). A weighting factor $w$ is used to determine the share of the electrical and the ICE paths in providing the power demanded by the driving cycle. By increasing the weighting factor from zero to unity, the vehicle controller increases the involvement of the ICE in the production of power for the drive-train. For low power demands ($P_{demand}$) the power distribution is as follows.

$$\begin{cases} P_b = (1-w)\cdot P_{demand} \\ P_e = w \cdot P_{demand} \end{cases} \tag{3.8}$$

where $P_b$ is the battery power, $P_e$ is the ICE power and $w$ is the weighting factor. For higher power demand, if the engine power hits the level corresponding to the highest efficiency point of the engine, the distribution of power changes as follows.

$$\begin{cases} P_b = (1-w)\cdot P_{demand} \\ P_e = P_{e,eff\ \max} \end{cases} \tag{3.9}$$

where $P_{e,effmax}$ is the engine power corresponding to its maximum efficiency point. This is to operate the engine in the most efficient region for a longer time and to increase the overall efficiency and range of the vehicle. For higher power demands, when battery reaches its maximum possible power, engine must be operated at higher power, with a view to provide the required power with the best efficiency possible. The power distribution for this case is as follows.

$$\begin{cases} P_b = P_{b,\max} \\ P_e = P_d - P_{b,\max} \end{cases} \tag{3.10}$$

where $P_{b,max}$ is the maximum battery power. Power distribution curves for different values of $w$ are depicted in the following figures. Fig. 3.4 shows the power distribution scheme for $w = 0$.

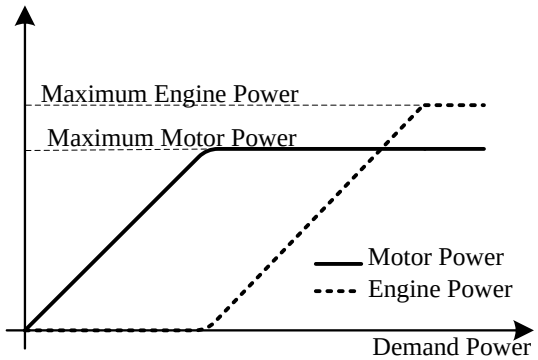


**Fig. 3.4 Power distribution, $w$=0.**

Since for this case, the engine has the least significant role as the primary source of power, it will not operate as long as the electrical part, i.e. the battery and the electric motor, is able to provide the demand power. Notice that this power distribution scheme is valid is for the period that the state of charge of the battery is in the desirable range and the battery can be further discharged. If the state of charge is lower than a minimum

value, the engine will provide the power demand in addition to the charging power for the battery. **Fig. 3.5** shows the controller logic for implementing this distribution.

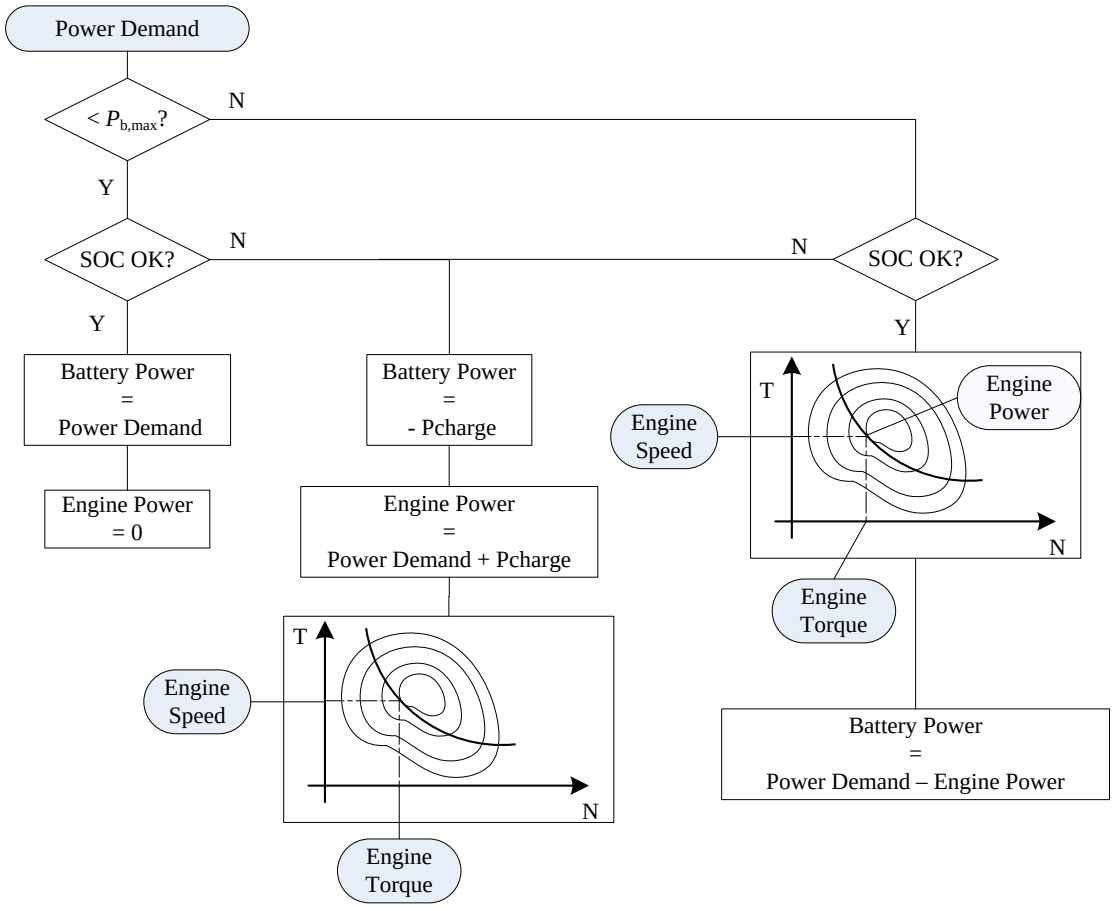


**Fig. 3.5 Controller logic for implementing power distribution with *w*=0.**

As shown in this figure, if the demand power is smaller than the battery maximum power and also if the battery has sufficient charge, all the power comes from the battery and the engine is off. When demand power is larger than the battery's maximum power, the engine starts contributing to power generation. If the battery does not have enough charge to contribute power, it will be charged using the power coming from the engine.

**Fig. 3.6** shows the $w = 1$ case. In this case the engine is the main source of power and electrical part is only used to assist the engine. In this power distribution scheme, the

engine provides the demand power until it reaches its maximum efficiency power level. After that point, the electric motor operates until it reaches its maximum power, beyond which the engine provides additional power until it also reaches its maximum power. This case is also valid when the battery has enough charge and could be discharged.

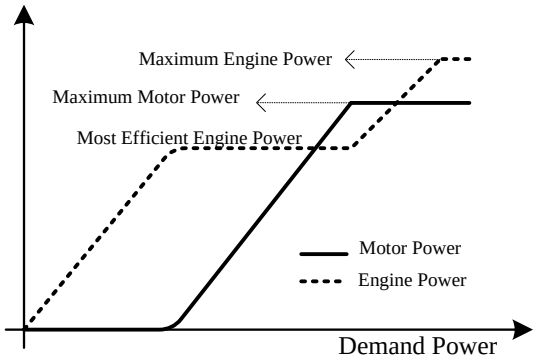


**Fig. 3.6 Power distribution, *w*=1.**

For a weighting function between 0 and 1, the motor and engine both contribute to provide the demand power. This case is shown in **Fig. 3.7** for $w = 0.5$.

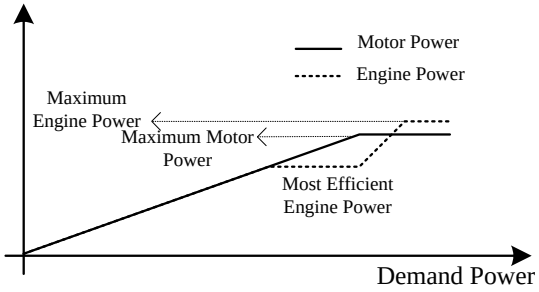


**Fig. 3.7 Power distribution, *w*=0.5**

In this mode, the demand power is distributed evenly between the electric motor and the engine. When engine power reaches the most efficient power for the engine, the engine reference power is kept constant and more power is demanded from the electric motor. This is to improve the vehicle efficiency and range. When the electric motor

power is reached its maximum value, the engine power is increased to meet the demand power.

### 3.3.4 Battery Model

Battery modeling is a major issue in modeling the drive-train. Batteries are electro-chemical elements and their behaviour depends on chemical reactions inside them, therefore describing their behaviour in terms of mathematical expressions is not an easy and precise practice. The way batteries are modeled is typically by using look-up tables [17]. A look-up table stores various parameters of the battery under different conditions. For example a look-up table may include the internal resistance and terminal voltage of a battery for different values of its state-of-charge. However for the purpose of steady-state modeling, a simpler model can be used. This model assumes that the battery is equipped with a proper climate control system. Assuming a constant temperature for the battery, the variations of the parameters of the battery due to changes in temperature can be ignored. In addition, it is assumed that the state-of-charge of the battery is confined to a limited range. Based on thesis assumption, the variations of the parameters of the battery due to changes in the state-of-charge can also be ignored. In the steady-state model developed for the battery, charge/discharge power is not allowed to exceed the battery ratings. Charge/discharge power is determined by the vehicle controller described in 3.3.3 and it is always limited to the power constraints of the battery.

Considering the assumptions above, the battery is able to provide a constant current as long as its state-of-charge is within the allowed range. Therefore, the output power of the battery model is in the interval of zero and its maximum allowed power output. The power is the maximum if the state of charge is within the desired range ($P_{b,max}$ in Fig.

3.5). If the state-of-charge is outside the desired range, the output power of the battery is zero and battery should be charged (refer to Fig 3.5).

There are two battery storage units within the drive-train, the internal pack and the external one. Charging power for the on-board battery pack may come from two sources, i.e. engine or regenerative brake. Charging power for the external battery pack comes from the plug-in charger unit. Charging algorithm is explained in the next section.

Battery efficiency is modeled by multiplying the charging power by the efficiency figure. Having charge/discharge power for the battery, charge/discharge current can be calculated by dividing the power by the battery's terminal voltage. Using the battery current, the battery state-of-charge can be calculated as follows.

$$SOC = SOC(0) - \frac{1}{C_b}\int_0^t i_b dt \qquad (3.11)$$

where $SOC$ is the battery state-of-charge, $i_b$ is the battery current and $C_b$ is the battery capacity (refer to Table 3-1).

Note that the assumptions listed above are to allow a convenient model of the battery to be constructed. Since various battery technologies tend to show markedly different behaviour, the most accurate approach to their incorporation into a simulation environment is to use actual battery packs in a hardware-in-loop setup. This will be pursued later and is a prominent direction of the research. However for this preliminary analysis a simplified model as described above is adequate.

The steady-state model of the battery consists of battery cells, which together form a battery pack. The number of cells in the battery pack is changed to find the optimal number of these cells. **Table 3-1** shows the typical cell characteristics that are used for

each of the battery technologies considered in this study. Note that large deviations from these typical characteristics may exist within each battery type. This is particularly true for the Li-ion chemistry, which is currently under significant development.

**Table 3-1 Battery module specifications**

| Battery Type | Lead Acid | Ni-MH | Li-Ion |
|---|---|---|---|
| Cell Voltage [V] | 6 | 1.2 | 3.6 |
| No of cells per module | 2 | 6 | 3 |
| Capacity [Ah] | 12 | 6.5 | 6 |
| Module weight [kg] | 4.79 | 1.04 | 0.99 |
| Specific energy density [Wh/l] | 90 | 175 | 200 |
| Efficiency (at 1C charge/discharge) [%] | 80 | 90 | 95 |
| SOC swing range [%] | 20 | 70 | 70 |
| Cost [$/kWh] | 145 | 365 | 1000 |

## 3.4 Battery Charging Algorithms

When the on-board battery pack depletes to its minimum allowable SOC, power must be drawn from the internal combustion engine to re-charge it. Battery charging normally takes place when the vehicle is in motion, implying that the ICE has to provide both the propulsion and the charging power. Charging during idle time, e.g. when the vehicle is stopped at an intersection, may be allowed although it is disabled in the developed model here. The other charging occasion is regenerative braking. Regenerative braking saves the kinetic energy of the moving vehicle instead of wasting it in mechanical brakes, as explained next.

### 3.4.1 Regenerative Braking

Regenerative braking is a way to save part of the kinetic energy of the moving vehicle in batteries rather than dissipating it as heat as is the case with conventional mechanical

brakes. Regenerative braking is only applicable when the state of charge of the battery allows the control system to recharge it. If the SOC of the battery is already at the maximum allowable limit, the kinetic energy must be dissipated through the mechanical brakes. The other limitation for the regenerative braking is the charging current limit for the battery. In other words, the kinetic energy flow back to the batteries should not exceed the batteries' allowable charging limits. During hard braking incidents the mechanical brake will dissipate the excess energy in order to provide the required braking torque. In the steady-state model, it is assumed that regenerative braking is done with a given efficiency, representing that of the mechanical to electrical conversion process involved.

### 3.4.2 Plug-in Charging

A retro-fitted plug-in hybrid electric vehicle can also be charged from an outlet. During the charging periods power from the outlet goes to the external battery pack only. Two charging strategies are considered, namely (a) overnight charging and (b) overnight and opportunity charging. In the overnight charging strategy the external battery pack is charged via the utility grid only during the nightly parking hours. Opportunity charging allows the additional battery pack to be charged during periods of vehicle parked-time during the day as well. In this study, opportunity charging is done whenever the vehicle is parked for at least three hours.

## 3.5 Vehicle Parameters and Fuel Economy

In this research, parameters of Toyota Prius are used in the retro-fitted plug-in hybrid electric vehicle model. Vehicle parameters such as vehicle weight, frontal area, and aerodynamic coefficient are required to calculate applied forces to the vehicle in the steady-state and transient models. These parameters are listed in **Table 3-2.**

**Table 3-2 Vehicle parameters**

| Parameter | Value |
|---|---|
| Curb weight ($M_v$) | 1330 [kg] |
| Passenger weight | 80 [kg] |
| Frontal area ($A_f$) | 2.23 [$m^2$] |
| Aerodynamic coefficient ($C_d$) | 0.26 |
| Air density ($\rho$) | 1.204 [$kg/m^3$] |
| Gravitational acceleration ($g$) | 9.8 [$m/s^2$] |

The drive-train of the vehicle consists of two electric machines, i.e. MG1 and MG2 plus the internal combustion engine. These components are connected to the power-split gear device. The output power from PSG is then delivered to the wheels via the transmission system. The efficiency of each component is required in the steady-state model to calculate the power flow in the drive-train. These efficiencies are listed in **Table 3-3.**

**Table 3-3 Component efficiencies**

| Parameter | Efficiency [%] |
|---|---|
| Motor + Converter | 80 |
| Generator + Converter | 80 |
| Regenerative braking | 70 |
| Transmission | 85 |

Note that although the efficiency of the electric machines and power-electronic converters change with the changes in their operating point, these changes are small comparing to the efficiency change in the engine [44], [45]. Therefore, a constant efficiency is considered for the electric drive system. Engine efficiency in this model is not constant and is subject to change with changes in its operating point. The efficiency map of the engine is shown in **Fig. 3.8**. As shown, engine efficiency varies from efficiencies as low as 5% to efficiencies more than 30%. The objective of the vehicle controller is to operate the engine at its most efficient areas. The operating point of the engine for each point of the driving cycle is calculated based on the efficiency of the engine on that point and the energy density of gasoline.

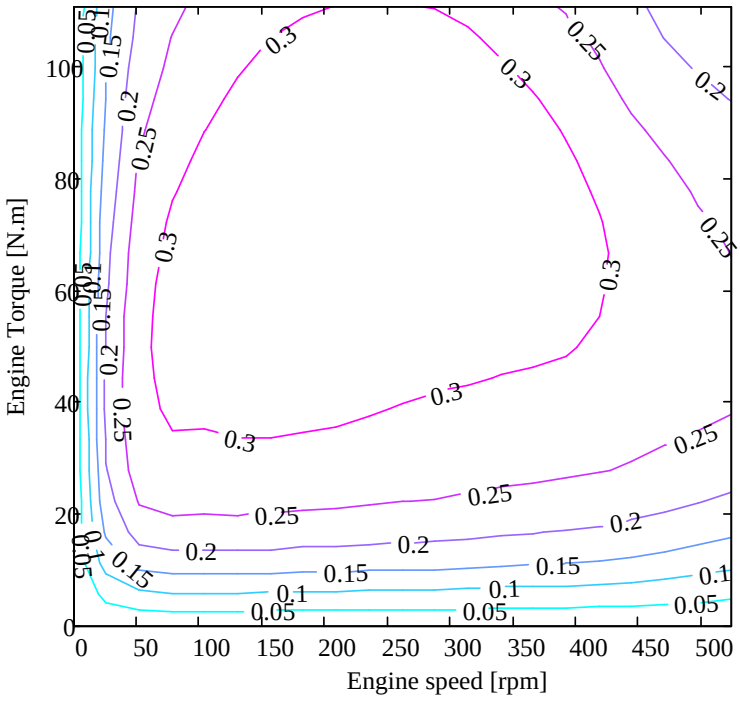


**Fig. 3.8 Efficiency map of the ICE.**

# 3.6 Model Assembly, Verification and Simulation Results

The developed transient model has two battery storage units. The first is the on-board battery pack, which comes with the conventional hybrid electric vehicle. The second one is the external pack, which is the additional battery storage used in retrofit conversion of the hybrid electric vehicle to plug-in. A simulation-based approach is adopted to determine the optimal size of the external battery storage. Block diagram of the developed model is shown in **Fig. 3.9**.

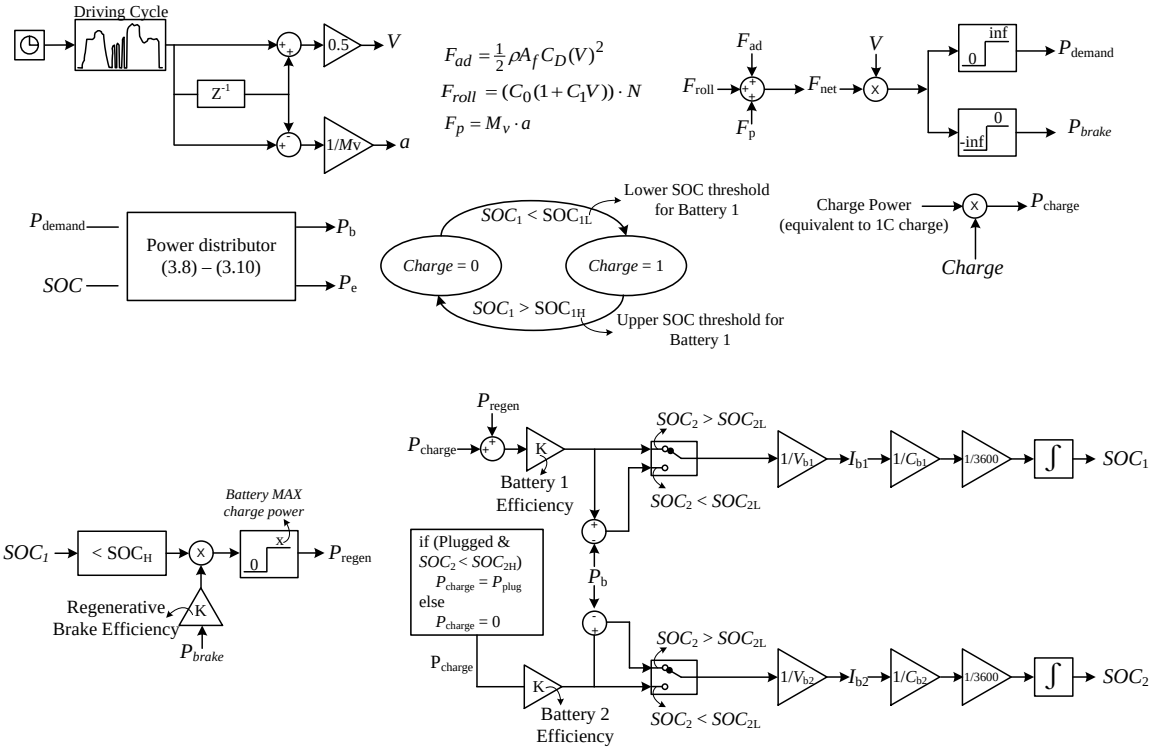


**Fig. 3.9 Block diagram of the steady-state model**

Vehicle speed, *V*, and acceleration, *a*, are calculated first using (3.3) and (3.1). Acting forces on the vehicle are calculated based on the vehicle speed, acceleration and vehicle parameters. These forces are, $F_{ad}$ (3.4), aerodynamic drag, $F_{roll}$ (3.5), rolling resistance, $F_p$ (3.2), propelling force. Total force, $F_{net}$ is calculated by adding all the calculated forces

(3.6). Demand and braking power, $P_{demand}$ (3.7) and $P_{brake}$, are calculated using the total force and vehicle speed, as shown in this figure. Demand power and state-of-charge of the batteries are sent to the power distributer subroutine to calculate the batter discharge power, $P_b$ and engine power, $P_e$. The method of calculation is explained in section 3.3.3. Brake power calculated in the previous step is used to calculate the regenerative brake power, $P_{regen}$. Note that battery state-of-charge, $SOC_1$ and maximum allowable battery power are also considered in this calculation. Battery discharge power and battery charge powers from different sources are used to calculate the battery currents ($I_{b1}$ and $I_{b2}$) and state of charge ($SOC_1$ and $SOC_2$). In this calculation, terminal voltage of the batteries ($V_{b1}$, $V_{b2}$) and their capacities ($C_{b1}$, $C_{b2}$) are used. Note that the on-board battery back is off-line as long as external battery pack is able to provide power ($SOC_2 > SOC_{2L}$).

When the external battery pack is depleted ($SOC_2 \leq SOC_{2L}$) the on-board batter pack is engaged. The internal batter pack is used until its state-of-charge goes below the minimum limit ($SOC_1 < SOC_{1L}$). At the point the battery pack goes into charge mode until its SOC hits the upper limit ($SOC_1 > SOC_{1H}$). The internal battery pack mode of operation is stored in a binary variable, *charge*. Charge power for the battery pack is 1C (6.5A for NiMH battery according to Table 3-1).

This study considers three major classes of batteries, i.e. the lead-acid, Ni-MH and Li-ion for the external battery. As mentioned above, the external battery receives its energy from the plug only. Therefore, charging strategy has a significant effect on vehicle performance. Two charging strategies are considered, i.e. (a) overnight charging and (b) overnight and opportunity charging.

The state-of-charge (SOC) swing ranges for the external battery should be selected suitably in order to ensure that the pack will sustain an acceptably large number of

charging cycles. In order to have a life of minimum 3000 cycles, the swing range for the lead-acid battery is chosen to be 20% [46]. The swing range for Li-Ion and NiMH battery is 70%. The initial SOC of the battery packs will adversely impact the simulation results if the driving cycle is not adequately long. To eliminate the impact of the initial SOC a weekly driving cycle is used. This driving cycle consists of more than 7 hours of driving during a typical week. The simulations were also conducted with a weekly and a monthly driving cycle and it was determined that the weekly cycle is long enough to eliminate the impact of any initial charge.

**Fig. 3.10**(a) shows the expected fuel economy of the retro-fitted vehicle as a function of its cost with the three external battery packs, with overnight grid charging of the PHEV. As shown, for the same cost an NiMH battery pack yields a markedly larger MPG rating compared with the other two technologies. For a given amount of investment in the external battery, the significant cost of a Li-ion pack does not allow a sufficiently large number of modules to be acquired resulting in a small capacity for the external battery pack. Conversely, a large lead-acid based external battery pack can be acquired; however the SOC swing range of a lead-acid pack is severely limited resulting in a small available effective capacity. The NiMH technology has a moderate cost and an adequately large swing range, and thereby provides the most suitable solution. For example for an estimated 112 MPG rating, the cost for the NiMH technology is around $2000, and the same investment will yield an MPG of 68 and 59 for the lead-acid and Li-ion chemistries, respectively as shown in **Fig. 3.10**(a).

The trends of the curves also indicate the return on investment (in terms of improved MPG for the dollar amount spent). As shown the NiMH technology has a steeper slope, which implies that the improvements in the fuel economy of the PHEV (relative to the

original hybrid) are larger for the same amount of investment in the extended battery pack.

**Fig. 3.10**(b) shows the volume of the battery pack as a function of its cost. This graph depicts another limitation of the lead-acid technology, which is its relatively large volume per kWh, which imposes a severe restriction on its applicability in the limited space available on-board a vehicle. Contrary to the common perception that the lead-acid technology is primarily limited by its weight, the simulations show that the use of this technology in the context of a PHEV is essentially hindered by its limited SOC swing range (to ensure longevity) and its large relative volume.

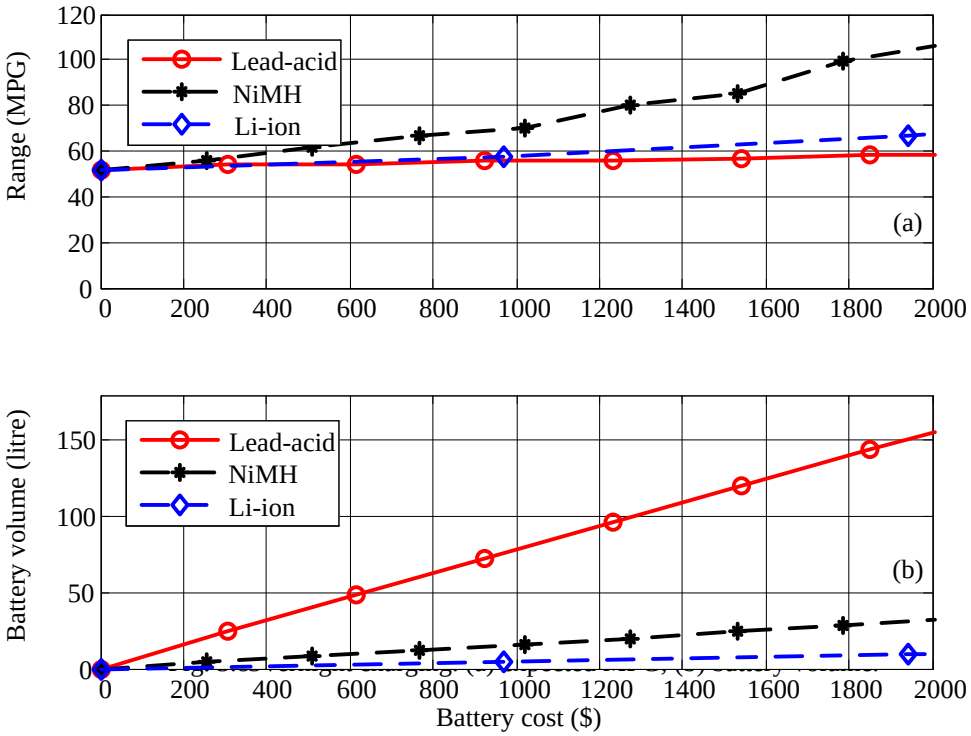


**Fig. 3.10 Overnight charging. (a) expected MPG; (b) battery volume.**

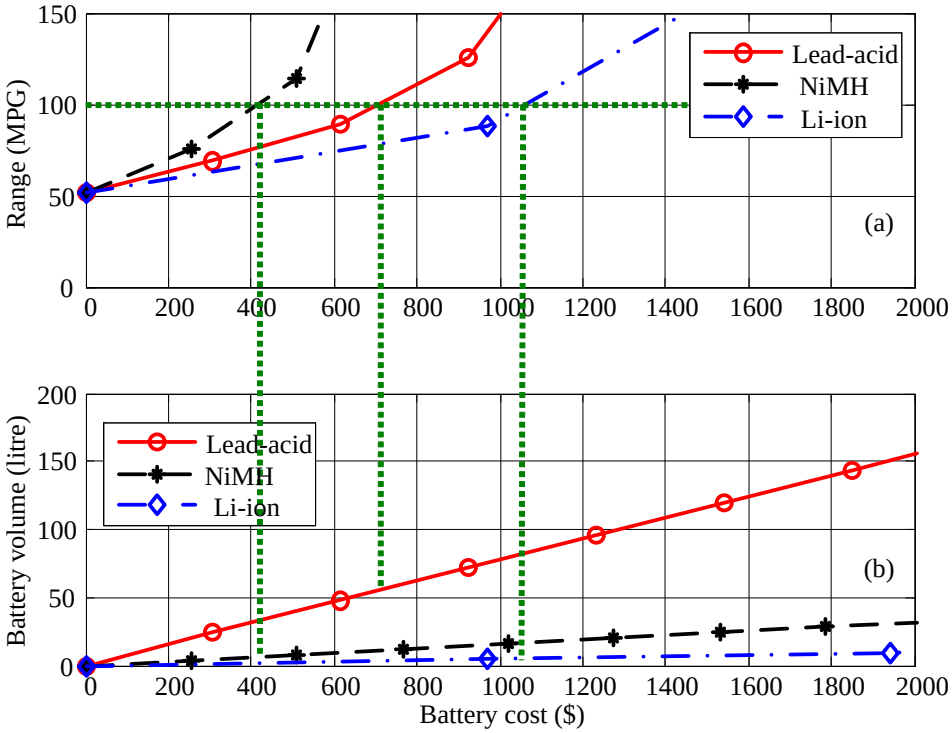


**Fig. 3.11 Opportunity charging. (a) expected MPG; (b) battery volume.**

Fig. 3.11 (a) and (b) shows similar trends for the PHEV battery pack when opportunity charging (during vehicle parked periods of at least 3 hours) is added to the original overnight charging. As expected, opportunity charging allows the external battery pack to become more available than the overnight charging scenario, thus improving the expected MPG ratings of the PHEV. For example, it is observed that the 100 MPG fuel economy is expected to occur for about $400 for the NiMH chemistry and at a volume of 15 litres.

The steady-state model is suitable for energy-related studies. The transient behaviour of the components in the drive-train is neglected in such studies. Transient models on the other hand, consider high levels of detail and are suitable for component and controller design for a drive-train. In this study, a transient model is developed for a power-split

gear drive-train and a hardware-in-loop simulation setup is then developed based on that. This setup uses real batteries in the simulation loop instead of battery models, which makes the simulations more accurate and expandable to emerging battery technologies. The transient modeling of the drive-train and the development of the hardware-in-loop setup is explained in Chapters 4, 5 and 6.

## 3.7 Chapter Summary and Contributions

The goal of this chapter was to determine the most-suited battery technology for a retro-fitted hybrid electric vehicle. Although there are studies reported in the literature with the same target, the method used in this thesis is different in its modeling technique and also in the drive-train used for sizing. One of the contributions of this thesis is developing a steady-state model for the hybrid drive-train. This model can simulate the vehicle performance for a given battery technology and size for a given driving cycle. Using this model, three battery technologies, i.e. Lead-acid, NiMH and Li-ion are tested. Battery size is changed for each battery type and the resulting vehicle range is calculated.

Another contribution of this thesis is using a new driving cycle developed by researchers at university of Winnipeg and University of Manitoba. This driving cycle represents the driving cycle for an average driver in the city of Winnipeg and can be used as a reference driving cycle for similar North American cities. Using this driving cycle, the results of this study are closer to reality in comparison to other studies, which use standard driving cycles for optimum battery sizing [35], [36].

Simulation results show that the energy density of the lead-acid battery is too small for hybrid electric vehicles. An excessively large battery pack should be installed in the vehicle in order to obtain a reasonable all-electric driving range.

NiMH and Li-ion batteries both have high energy densities. NiMH battery is less expensive and offers a slightly smaller energy density. Li-ion presently costs more, but its manufacturing costs are reducing. Considering the values used for this study, NiMH battery seems to be a more reasonable choice for the hybrid-electric drive-train.

This portion of the work was done in mid-2009. Every indication shows that Li-ion battery should drop in price. Therefore, Li-ion battery chemistry is used for the rest of this thesis. Li-ion battery is also used in the hardware-in-loop setup developed later in 2011. At that time the price of Li-ion batteries was indeed significantly lower than mid-2009.

# Chapter 4

# Transient Modeling and Simulation of Vehicular Systems

The focus of steady-state modeling of vehicular systems is on the overall efficiency and losses in the vehicle and it is useful in power-related studies such as estimating the range of a vehicle. In this research the problem of determining the optimal number of battery cells for a retro-fitted plug-in hybrid electric vehicle was solved using a steady-state model (refer to Chapter 3). However the steady-state model is not suitable for the study of fast dynamics of the vehicle. For these studies, developing a transient model is necessary. A transient model includes more details than a steady-state model and enables the user to examine dynamical behaviour of subsystems such as the electric motors, converters, etc. A transient model can also be used to design and tune fast-acting controllers such as converter controllers.

There are off-the-shelf simulators available for vehicular studies and many studies are done by these simulators [47]-[53]. Most of the available simulators are high-level ones [33] and are not suitable for low-level hardware-in-loop simulations. The transient simulators on the other hand may not be compatible with the available real-time simulator (i.e. Opal-RT simulator). In addition, using such simulators does not give a good understanding of the model since the details of modeling are not available to the user.

Other researchers who did hardware-in-loop simulation also had to go through the same path. For example in [54] a detailed model for a series drive-train is developed and implemented. For PSG based drive-train, there are studies that explain parts of the drive-train [22], [30], [40], but none of them covers the whole system. In this thesis, a transient model for a power-split gear based hybrid electric vehicle is developed in Matlab/Simulink for the first time. A prominent use of this transient model is its implementation on a real-time simulator and interfacing with real hardware components in a hardware-in-loop (HIL) setup. In the particular HIL setup developed in this research, actual batteries are interfaced with the simulator; this will allow to study the transient behaviour of the battery as well as to test emerging new battery technologies. Due to the complexity of batteries, obtaining an accurate model is often considered a bottleneck in modeling systems where battery storage systems are used. Including actual batteries in the loop of a real-time simulator alleviates the need for approximate mathematical modeling and thus improves the overall credibility of the simulation results.

The block diagram of the transient model is shown in **Fig. 4.1**. The model is a forward one that accepts the driving cycle and simulates the drive-train dynamics. This model can generate different types of outputs, ranging from fast response of power-electronic converters to fuel economy and slow dynamics of the vehicle.

The drive-train can be divided into two main subsystems, i.e. the mechanical subsystem and the electrical subsystem. A driver model is also developed to control the vehicle in a way that follows a certain driving cycle. This section describes the model components, their role in the model and their mathematical model derivation.

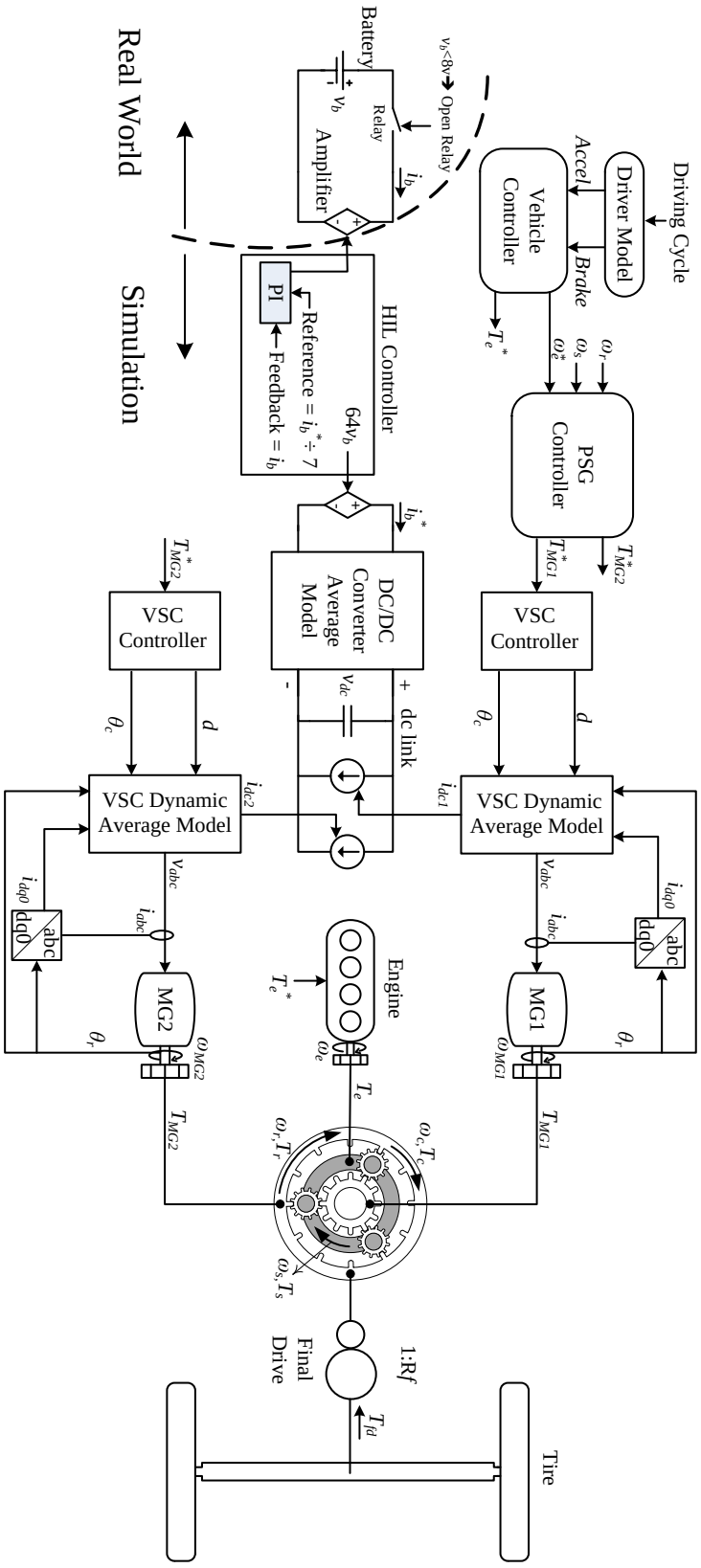


**Fig. 4.1 Block diagram of the detailed model.**

# 4.1 The Driver Model

In a real vehicle, the driver sends the torque command to the vehicle controller by pressing the accelerator and brake pedals. In the absence of a real driver in the developed transient model, a mathematical component that translates the input speed reference to a torque command is created and called the driver model. **Fig. 4.2** shows the block diagram of the driver model. As shown, a proportional-integral (PI) controller is used to find the required torque to reach the reference speed (including the braking periods when a negative torque is applied). The output of the PI controller is fed into a rate limiter, which limits the rate of change in the acceleration/brake requests. This makes the behaviour of the PI controller similar to a real (and responsible) driver, who does not apply sudden and violent acceleration or braking to the vehicle. Driving habits (mild or aggressive) can be modeled by changing the limit on the rate limiter. The acceleration and brake commands are also limited to their maximum allowable limits before being given to the vehicle model.

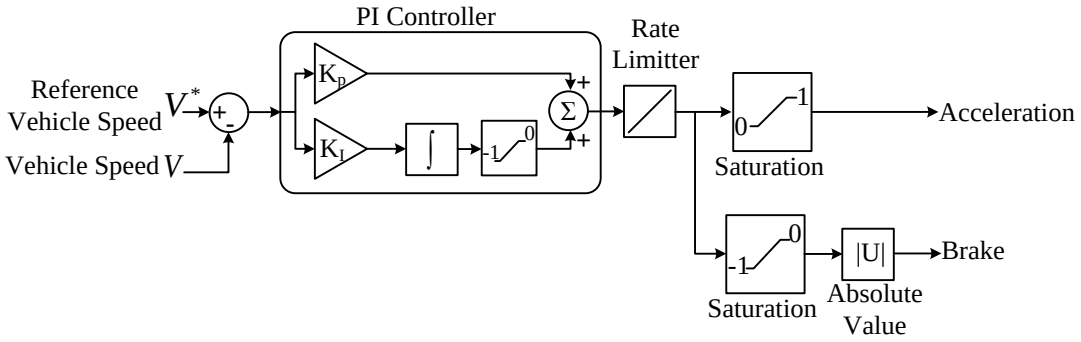


**Fig. 4.2 Driver model.**

## 4.2 Mechanical Subsystem

The mechanical subsystem of the drive-train includes vehicle dynamics (vehicle body), engine, power split gear device and tires. Each component is modeled using a transient model and interfaced with the rest of simulation. Details of modeling are presented in the following sub-sections.

### 4.2.1 Vehicle Dynamics

The vehicle dynamics block calculates the speed of the vehicle based on the propelling and resistive forces. Propelling force is provided by the wheel model. It depends on the propelling torque applied on the axel, wheel parameters and road condition. The vehicle dynamics block calculates the resistive forces as described in section 3.3.2. Vehicle acceleration is then calculated using Newton's second law of motion, as follows.

$$a = \frac{F_p - F_{res}}{M_v} \tag{4.1}$$

where $a$ is the vehicle acceleration, $F_p$ is sum of propelling forces from front and rear wheels, $F_{res}$ is sum of resistive forces (aerodynamic drag, rolling resistance and grade resistance) and $M_v$ is the vehicle mass. Using the calculated acceleration, the vehicle speed is calculated as follows.

$$V = \int_0^t a(\tau)d\tau + V_0 \tag{4.2}$$

where $V$ is the vehicle speed and $V_0$ is initial vehicle speed, specified by user.

The vehicle dynamic block also calculates the distribution of the normal weight of vehicle on the front and rear wheels. This distribution is then used in the tire model. The normal weight is calculated as follows [6].

$$N_f = \frac{L_b}{L}(Mg\cos\theta) - \frac{h}{L}\left(F_f + F_r - F_{roll}\left(1 - \frac{R_w}{h}\right)\right)$$
$$N_r = \frac{L_a}{L}(Mg\cos\theta) + \frac{h}{L}\left(F_f + F_r - F_{roll}\left(1 - \frac{R_w}{h}\right)\right) \quad (4.3)$$

where $N_f$ is the normal weight on front wheels, $L$ is the distance between from and rear axles, $L_b$ is the rear axle distance from center of gravity, $L_a$ is the front axle distance from centre of gravity, $g$ is the gravitational acceleration, $\theta$ is the road angle, $h$ is the center of gravity distance from ground, $F_f$ is the front wheels' propelling force (in previous step), $F_r$ is the rear wheels' propelling force, $F_{roll}$ is the total rolling resistance and $R_w$ is the effective wheel radius. Total propelling force is sum of front wheel and rear wheels' propelling forces.

$$F_{prop} = F_f + F_r \quad (4.4)$$

Fig. 4.3 shows the applied forces and dimensions used in (4.3). **Fig. 4.4** shows the inputs and outputs of the vehicle dynamics block (Note that the total propelling force is used in this model instead of individual front and rear propelling forces).

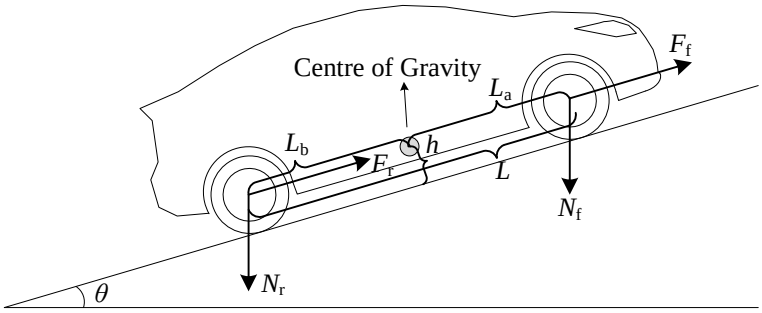


**Fig. 4.3 Dimensions of vehicle used in vehicle dynamic model**

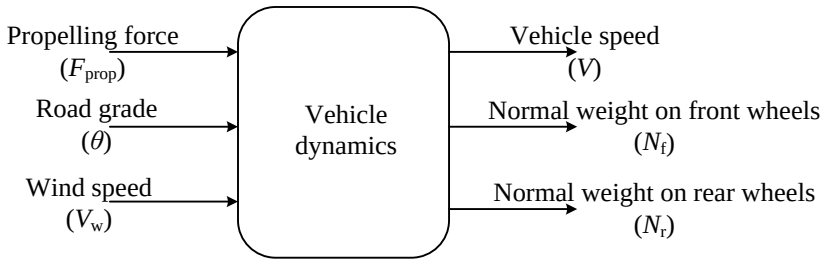


**Fig. 4.4 Vehicle dynamics block**

### 4.2.2 Internal Combustion Engine (ICE)

Accurate modeling of an ICE requires a broad range of experimental data. This model can simulate the transient of ICE based on the available experimental data. Since the objective of this research does not include studying the transient behaviour of the ICE, a simplified model for ICE is used. This model accepts the reference torque of the ICE and calculates the output torque of this component. Ideally the ICE should output a torque equal to its reference value instantaneously; however due to physical delays, the transition from one torque output to another is accompanied with some delay. The transient model of the ICE, therefore, consists of a time delay, representing the response time of the engine. This delay can be simply modeled by a first-order transfer function, as follows.

$$T_e = \frac{1}{1+\tau s} T_{e,ref} \tag{4.5}$$

where $T_e$ is the ICE output torque, $\tau$ is the time constant of engine response, and $T_{e,ref}$ is the reference torque for engine. This method for modeling the internal combustion engine is also used in [55]. The time constant of engine is typically around 0.5 seconds [56]. **Fig. 4.5** shows the engine block used in the model.

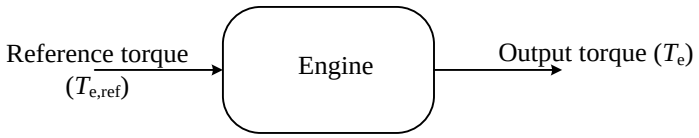


**Fig. 4.5 Engine block**

### 4.2.3 Power-Split Gear (PSG) Device

The most important part of the modeled drive-train is the power-split gear device, which couples MG1, MG2 and engine. A power-split gear device is a three gear mechanical element.

The connections to a power-split gear device in a hybrid electric vehicle are shown in **Fig. 4.1**. As shown, MG1 is connected to the sun gear, and provides charging power for the batteries; it is also used as a starter to start the ICE. The other important role of MG1 is to control the operating point of the ICE at the most efficient operating region (for the given power) on its efficiency map. The carrier of the power-split gear device is connected to the ICE. Therefore, the ICE is coupled to both sun and ring gears and can provide power for both. The outer gear of the power-split gear device, the ring, is connected to MG2. MG2 provides propelling toque for the vehicle in its different modes of operation, which will be discussed later. **Fig. 4.1** also shows the sign convention for respective torque and speed values. Arrows on the figure show the assumed positive direction of applied torques and the assumed positive direction of rotation of each gear. In a power-split gear device, the fundamental relationship between ring, carrier and sun speed comes from the topology of the PSG and is expressed as follows.

$$\omega_s S + \omega_r R = (R + S)\omega_c \tag{4.6}$$

where $\omega_s$, $\omega_r$ and $\omega_c$ are sun, ring and carrier speeds, respectively, and $R$ and $S$ are the numbers of teeth on the ring and sun gears, respectively. The dynamic model for this

device is developed using dynamic speed equations for each gear. The dynamic equation for the ring gear is as follows.

$$J_r \frac{d\omega_r}{dt} = T_r - \frac{1}{\rho} T_{sun} - \frac{1}{R_f} T_{fd} \tag{4.7}$$

where $J_r$ is the total inertial of the connected components to the ring including the MG2 and final drive, $T_r$ is the torque applied to the ring by MG2, $T_{sun}$ is the net torque applied to the sun gear and $\rho$ is the power-split gear ratio defined as $\rho = \frac{S}{R}$. This maps the net torque on the sun to the value that affects the motion of the ring gear. $R_f$ is the final drive's gear ratio and $T_{fd}$ is the final drive's opposing torque due to wheel-road junction. The carrier speed dynamic equation can be written as follows.

$$J_c \frac{\omega_c}{dt} = T_c + (1 + \frac{1}{\rho}) T_{sun} \tag{4.8}$$

where $J_c$ is the combined carrier and engine inertia and $T_c$ is the applied torque to the carrier from engine. The applied torque to the sun gear, which is used in (4.7) and (4.8) can be expressed as follows.

$$T_{sun} = T_{MG1} - J_s \frac{d\omega_s}{dt} \tag{4.9}$$

where $T_{MG1}$ is the applied torque to the sun gear form MG1 and $J_s$ is the sun gear and generator inertia. Using (4.6) to (4.9) and some mathematical simplifications, one can write the state space equations of the PSG as follows.

$$\begin{aligned} \frac{d\omega_c}{dt} &= A_1 T_{MG1} + A_2 T_e + A_3 T_{MG2} + A_4 T_{fd} \\ \frac{d\omega_r}{dt} &= B_1 T_{MG1} + B_2 T_e + B_3 T_{MG2} + B_4 T_{fd} \end{aligned} \tag{4.10}$$

where $T_e$ is the engine torque applied to the carrier, $T_{MG2}$ is MG2 torque applied to the ring gear. Constant coefficients $A_1$ to $A_4$ and $B_1$ to $B_4$ are derived by simplifying equations. These coefficients are listed in Appendix C. Once the carrier and the ring gear

speeds are found, the sun gear speed can be calculated using (4.6). The net propelling torque on the ring gear is calculated as follows.

$$T_{ring} = T_{MG2} - \frac{1}{\rho} T_{sun} \tag{4.11}$$

The transient model of the power-split device is developed using equations (4.6), (4.10) and (4.11). **Fig. 4.6** shows the power-split gear device block used in the model. This block accepts torque from MG1, MG2, ICE and the final drive and calculates speed of electric machines and ICE and also the propelling torque. The calculated speeds are sent to the corresponding component models and the propelling torque is sent to the wheel model to calculate the propelling force.

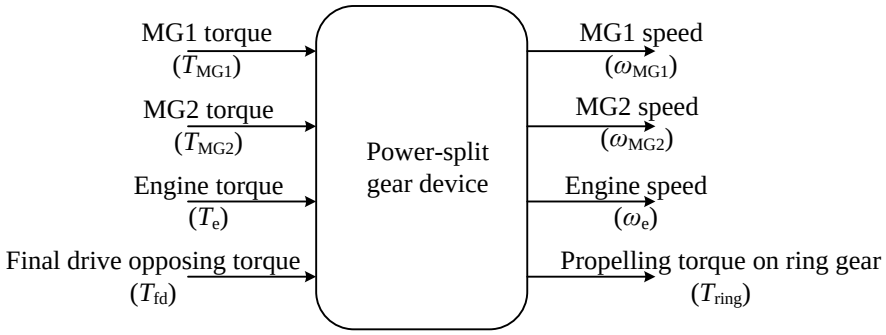


**Fig. 4.6 Power-split gear device block**

### 4.2.4 Tire Model

The power-split gear model calculates the propelling torque applied to the ring gear. This torque is applied to a final drive and eventually to the wheels. This torque, called the tractive torque, rotates the wheels, generates the propelling force, and propels the vehicle. The amount of propelling force depends on the applied torque to the wheel, wheel dimensions, wheel material and road type and condition.

If the tractive force of the vehicle exceeds the limitation of maximum tractive force due to the adhesion characteristics between the tire and the ground, the drive wheels will

start spinning on the ground. This is especially true when the vehicle is driven on wet, icy, snow-covered, or soft soil roads. In such cases, excessive tractive torque on the wheel causes the wheel to have significant slippage on the ground. This phenomenon is modeled in the transient model of the drive-train using Pacejka magic formula [57]. To model the tire, the tire slip is first calculated as follows.

$$\begin{aligned} \lambda &= \left(1-\frac{V}{r\omega}\right) \quad \text{(during acceleration)} \\ \lambda &= \left(1-\frac{r\omega}{V}\right) \quad \text{(during braking)} \end{aligned} \tag{4.12}$$

where λ is the tire slip, $V$ is the vehicle speed, $r$ is the tire radius, $\omega$ is the tire angular velocity. During acceleration $r\omega$ is larger than $V$ and during braking, $V$ is larger than $r\omega$. Tire slip, $\lambda$, is always between zero and one. When $\lambda$=0, tire has no deformation with a circular cross-section. When $\lambda$=1, tire is spinning but vehicle does not move ($V$=0). Using λ, tractive force coefficient, $\mu$, can be calculated using Pasejka formula as follows.

$$\mu = D\sin\left(C\tan^{-1}\left(B(1-E)\lambda + E\tan^{-1}(B\lambda)\right)\right) \tag{4.13}$$

where $B$, $C$, $D$ and $E$ are Pacejka coefficients, which describe the characteristics of the road.**Table 4-1** lists these parameters for different road conditions.

**Table 4-1 Pacejka coefficients**

| Surface | B | C | D | E |
|---|---|---|---|---|
| Dry Tarmac | 10 | 1.9 | 1 | 0.97 |
| Wet Tarmac | 12 | 2.3 | 0.82 | 1 |
| Snow | 5 | 2 | 0.3 | 1 |
| Ice | 4 | 2 | 0.1 | 1 |

Using $\mu$, the tractive force can be calculated as follows.

$$F = \mu \cdot N \tag{4.14}$$

where $N$ is the normal weight on the wheels calculated in the vehicle dynamics block. Note that the vehicle dynamics block calculates the normal weight on the front and rear axles. Assuming that the weight is equally distributed between right and left wheels, the normal force for each front tire is $\frac{1}{2}N_f$ and it is $\frac{1}{2}N_r$ for each rear tire.

The tractive force calculated in this block is sent to the vehicle dynamics model as the propelling force and used for vehicle speed calculation. **Fig. 4.7** shows the tire block used in the model. It accepts vehicle speed and normal weight on the wheel from vehicle dynamic model and wheel speed and propelling torque from power-split gear device model. The output of this block is the propelling force, which is sent to the vehicle dynamics block.

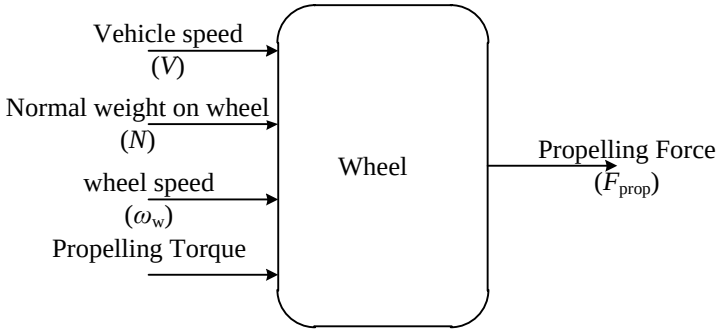


**Fig. 4.7 Tire block**

## 4.3 Electrical Subsystem

Electrical subsystem includes battery, dc/dc converter, VSC1, VSC2, MG1 and MG2 in **Fig. 4.1**. The battery in this system is the energy-storage device in the drive-train. The battery is interfaced to the dc-link via a bi-directional dc-dc converter. The dc-dc converter regulates the dc-link voltage and uses the charge from the battery during the electric drive and electric-assist modes, and charges the battery when its state-of-charge

is low. It also absorbs the energy during the regenerative braking and transfers it to the battery.

The dc-link is connected to two voltage-source converters (VSCs). Each VSC is connected to a permanent magnet synchronous machine (MG1 and MG2). This section explains the components used in the electrical subsystem and their dynamic model derivation.

### 4.3.1 The Battery Model

Battery models can be globally divided into three main types of (i) experimental, (ii) electrochemical and (iii) electric circuit-based models. The electric circuit based model is the most suited one to represent the electrical characteristics of the battery [58]. The simplest circuit-based battery model comprises an ideal fixed voltage source in series with a fixed resistance [59]. However this model does not consider the state-of-charge (SOC) of the battery and its impact on both the internal voltage and the effective series resistance of the battery. It is well known that variations in the state-of-charge affect both the internal voltage and the internal resistance. Modeling these effects is a cumbersome task and needs mathematically involved models [60]. Depending on the accuracy needed for the application at hand, the model can be simplified to neglect the effect of SOC on internal resistance of the battery [17], [61]. Its impact on the internal voltage is, however, more profound and is therefore modeled.

To model the state-of-charge of the battery accurately, one should model the electrochemical behaviour of the battery. Such modeling is done in [61], which introduces mathematical equations that describe the electrochemical behaviour of the battery in charging and discharging conditions and at the same time calculates the state-

of-charge of the battery. This model is modified in [62] and [58] to make it more suitable for numerical simulations. The battery model used in this research is an electric circuit-based model similar to the one developed in [58]. The model represents the battery dynamics using a voltage source and a series resistor, as shown in **Fig. 4.8**. In this figure, $E_b$ is the battery internal voltage, $R$ is the battery internal resistance, $V_b$ is terminal voltage and $i_b$ is the battery current. The internal resistance of the battery is assumed to be constant and the internal battery voltage changes according to battery current and state-of-charge.

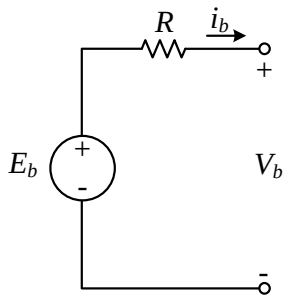


**Fig. 4.8 Battery model**

Most of the battery parameters can be derived from the discharge curve of the battery. In this research a Li-ion battery pack is used as the energy-storage device in the drive-train. A typical discharge curve of this battery type is shown in Fig. 4.9.

In this figure, $Q_{exp}$ is the capacity of the battery in exponential region, $Q_{nom}$ is the nominal capacity of the battery, $Q$ is the full capacity of the battery, $V_{full}$ is the full-charge terminal voltage and $V_{exp}$ and $V_{nom}$ are terminal voltages corresponding to $Q_{exp}$ and $Q_{nom}$, respectively. As this figure shows, by discharging the battery the terminal voltage drops exponentially in the beginning in the region known as exponential region. The voltage

drop becomes linear in the nominal region. After exceeding the nominal capacity of the battery, the voltage rapidly collapses.

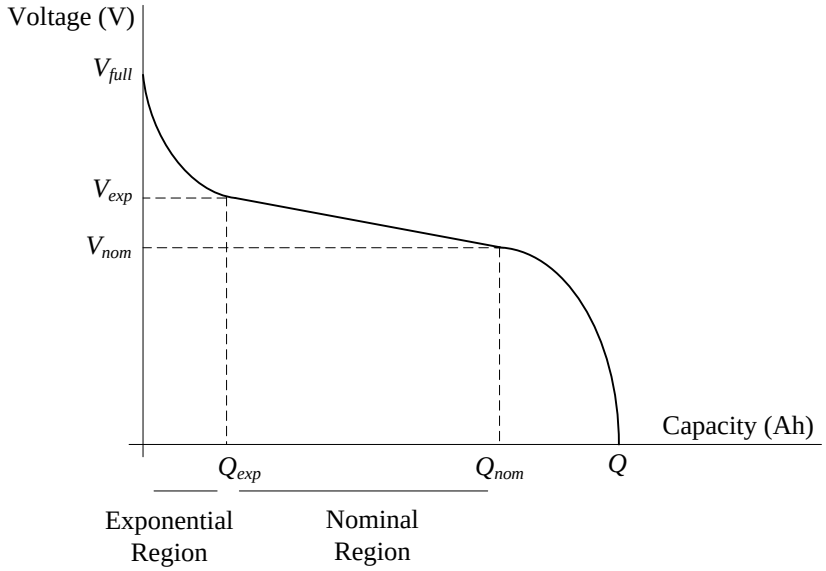


**Fig. 4.9 Typical discharge curve of the battery**

In the battery model, the internal voltage will change in a way that the terminal voltage follows the discharge curve. The internal voltage for charge and discharge conditions is calculated as follows [58].

$$\begin{aligned} &\text{Discharge}: \quad E_b = E_0 - K\frac{Q}{Q - i\cdot t}\left(i\cdot t + i^*\right) + A\exp(-B\cdot i\cdot t) \\ &\text{Charge}: \quad E_b = E_0 - K\frac{Q}{i\cdot t - 0.1\cdot Q}\cdot i^* - K\frac{Q}{Q - i\cdot t}\cdot i\cdot t + A\exp(-B\cdot i\cdot t) \end{aligned} \tag{4.15}$$

where $E_0$ is the battery constant voltage (V) which should be measured in an experiment for a given battery technology. $K$ is the polarization resistance ($\Omega$). This is also an experimental parameter. Polarization resistance is a coefficient that determines the effect of battery current on its internal voltage. $Q$ is battery capacity (Ah), $A$ is exponential zone amplitude (V), $B$ is exponential zone time constant inverse $(\text{Ah})^{-1}$, $i$ is battery current (A) and $i^*$ is filtered current (A). A low-pass filter is used to obtain a ripple-free battery current. Details of this modeling and equation derivation are reported in [58]. **Table 4-2**

lists the parameter values that are used to describe the battery cell used in this research. The cell is a 3.2V, 2.6Ah Li-ion battery. The battery pack includes 7 parallel branches of 64 cells (448 cells in total) as shown in **Fig. 4.10**

**Table 4-2 Battery model parameters [58]**

| Parameter | Value | Unit |
|---|---|---|
| $E_0$ | 3.37 | V |
| $R$ | 0.01 | Ω |
| $K$ | 0.0076 | Ω |
| $A$ | 0.26422 | V |
| $B$ | 26.5487 | $(Ah)^{-1}$ |

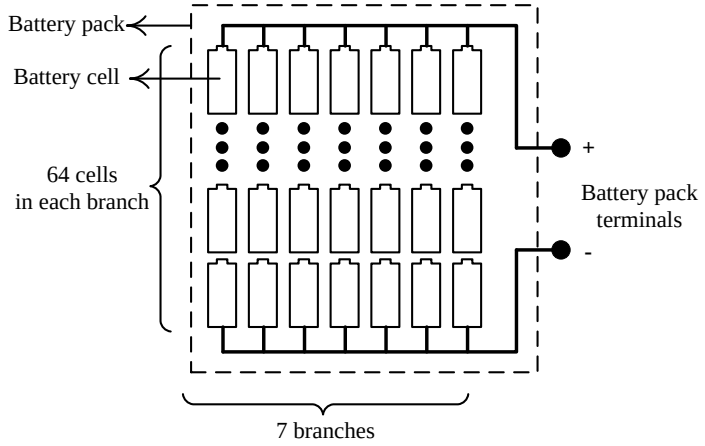


**Fig. 4.10 Battery pack including 448 battery cells.**

## 4.3.2 DC-DC Converter

The dc-dc converter shown in **Fig. 4.11** is a bidirectional converter. Using this converter power can travel in both directions, i.e. from battery to dc link or from dc link to the battery. Since in the developed model the dc link has a higher nominal voltage than the battery, the converter operates as a boost (step-up) converter when it delivers power from the battery to the dc link (forward direction), and as a buck (step-down) converter when it delivers power from the dc link to the battery (reverse direction) as shown in **Fig. 4.12** and **Fig. 4.13**.

This converter is modeled using standard models for IGBT and diodes available in MATLAB/Simulink. These models include conduction losses and ignore the switching losses of the component [63].

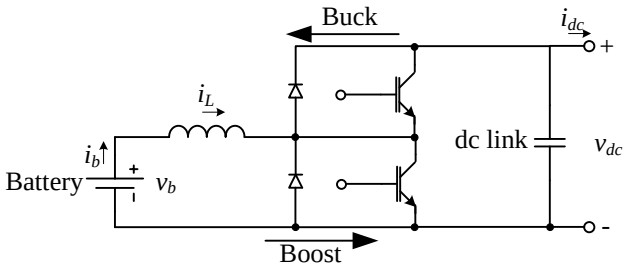


**Fig. 4.11 Diagram of the bidirectional dc-dc converter used in the electrical subsystem.**

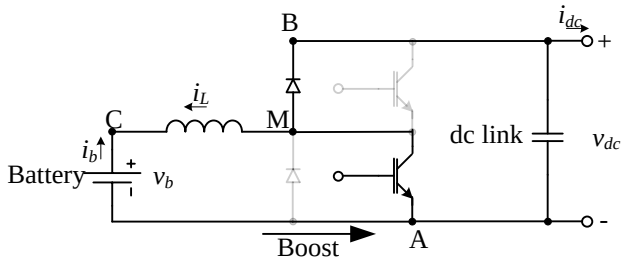


**Fig. 4.12 The dc-dc converter in boost mode of operation.**

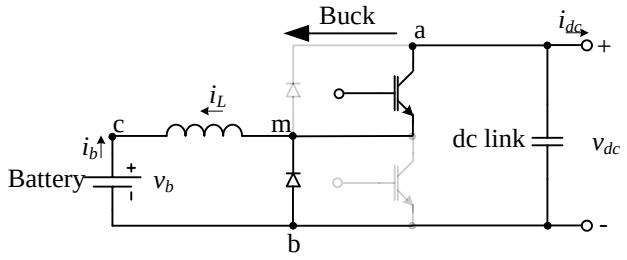


**Fig. 4.13 The dc-dc converter in buck mode of operation.**

### 4.3.3 Voltage Source Converters

A schematic diagram of a two-level VSC used in the drive-train is shown in **Fig. 4.14**. The converter is connected to the dc-link on the dc side and to an electric machine on the ac side. The VSCs in the hybrid drive-train considered herein employ standard sinusoidal pulse-width modulation (PWM) to synthesize the three-phase voltages with desired

magnitude and frequency at the terminal of the motor. Modeling of this scheme including its switching is straightforward and well documented [64], [65]. The sinusoidal PWM is based on comparison of a fundamental-frequency sinusoidal reference with a high-frequency triangular carrier waveform for each of the legs of the VSC. The high-frequency switching instants of the converter transistors are determined by the multiple crossings of the two waveforms.

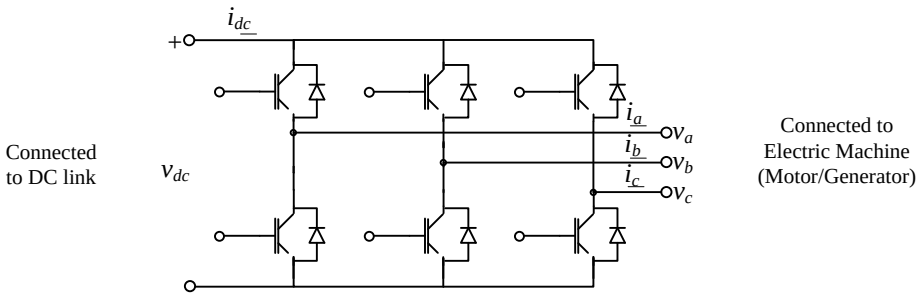


**Fig. 4.14 Schematic diagram of a two-level voltage-source converter.**

### 4.3.4 The Electric Machines (MG1/MG2)

MG1 and MG2 are both permanent magnet (PM) synchronous machines. These machines are identical to the ones used in the drive-train of the commercial Toyota Prius (second generation). The PM machine model used in this study is the standard transient model expressed in a synchronously-rotating dq0 reference frame [64]. Modeling and control strategy for these machines are explained in Appendix B.

## 4.4 Controllers

The controllers in the drive-train vary from high-level controllers, which control the flow of power in the vehicle (vehicle controller), to low-level controllers that control the electric machines (MG1 and MG2) and dc-link in a proper way so that the required

power flow in the drive-train occurs. This section explains controllers in the drive-train as well as connections and communications between these controllers.

### 4.4.1 Vehicle Controller

The vehicle controller is the highest level of control in the vehicle. This controller determined the power flow in the vehicle in order to meet the driver's demand with highest efficiency and minimum fuel consumption. The vehicle controller used in the transient model is identical to the vehicle controller used in the steady-state model described earlier in Section 3.2.3. As mentioned in the previous chapter, the vehicle controller accepts the power demand as the input and calculates reference power for the battery and the operating point for the ICE. The power required to maintain a constant speed is calculated using the vehicle speed and resistive forces calculated in vehicle dynamic model. This power is then augmented by a feedback loop to make sure that the power going to the wheels from the battery meets the reference battery power determined by the vehicle controller (**Fig. 4.15**).

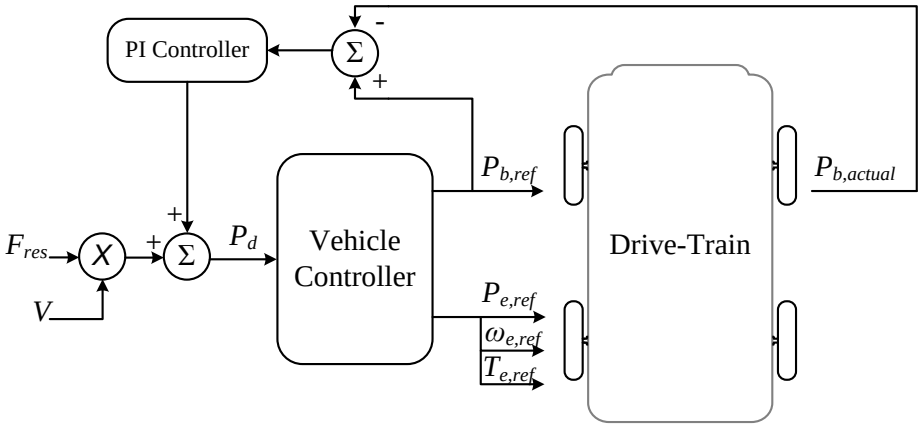


**Fig. 4.15 Power demand calculation in transient model.**

In this figure, $F_{res}$ is the resistive force against the vehicle movement, $V$ is the vehicle speed, $P_d$ is demand power, $P_{b,ref}$ is reference battery power, $P_{e,ref}$ is reference engine power, $\omega_{e,ref}$ is engine reference speed, $T_{e,ref}$ is engine reference torque and $P_{b,actual}$ is the actual battery power. The power required to maintain a constant speed is the product of resistive forces and vehicle speed. The demand power is sum of propelling power and power losses within the drive-train. Compensation for power system losses is done using a PI controller. This controller smoothly changes the demand power in a way that the actual battery power matches the battery reference power. The demand power fed to the vehicle controller has the correct value when these powers match.

### 4.4.2 Power-Split Controller

The vehicle controller is a high-level controller, which determines the flow of power within the drive-train. A low-level controller in the transient model, i.e. the power-split controller, controls the power-split gear device in a way that the appropriate flow of power, determined by the vehicle controller occurs. The power-split gear controller controls MG1, MG2 and ICE. **Fig. 4.16** shows the block diagram of this controller.

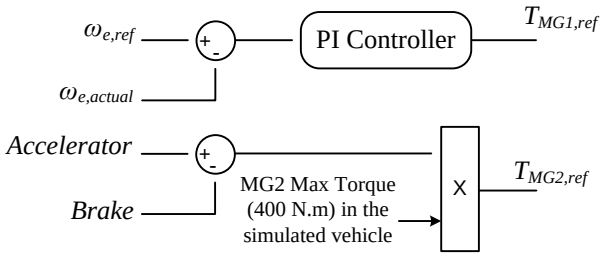


**Fig. 4.16 Power-split gear controller.**

In this figure, $\omega_{e,ref}$ is the engine reference speed, $\omega_{e,actual}$ is engine actual speed, $T_{MG1,ref}$ is MG1 reference torque, *"Accelerator"* is the accelerator pedal input, *"Brake"* is

the brake pedal input and $T_{MG2,ref}$ is MG2 reference torque. MG2 torque is calculated based on the driver input. This makes the "feeling" of driving a PHEV similar to feeling of driving a conventional car in which the accelerator pedal is the torque controller. Engine reference speed and torque come from the vehicle controller. The engine speed is controlled using MG1. This machine will rotate at the proper speed so that the engine works at the speed determined by the vehicle controller.

### 4.4.3 DC-Link Controller

The main objective of dc-link controller is to maintain the dc-link voltage constant. This is done by transferring the power either from the battery to the dc-link or from the dc-link to the battery. When the dc-link voltage drops, controller aims to increase the voltage by drawing current from the battery and transferring power to the dc-link. If the dc-link voltage exceeds the reference value (for example, in regenerative brake instants), the controller aims to decrease the voltage by absorbing the power from the dc-link and sending it to the battery. This controller is shown in **Fig. 4.17**.

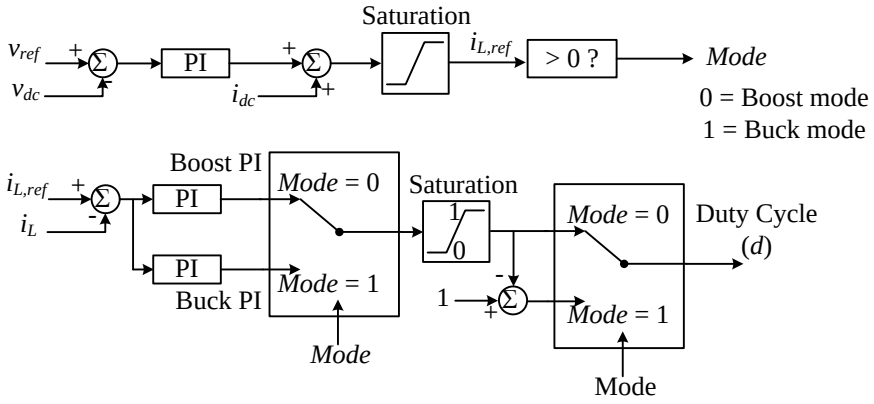


**Fig. 4.17 The dc-link controller**

In this figure, $v_{ref}$ is the dc-link voltage reference, $v_{dc}$ is the dc-link voltage, $i_{dc}$ is the current going to VSCs (refer to **Fig. 4.1**). $i_{L,ref}$ is the reference inductor current, $i_L$ is the inductor current, *Mode* is the mode of operation of the converter (buck or boost) and *d* is the duty cycle of the converter. The duty cycle directly determines the reference waveform for a PWM controller which controls signals going to the gates of the dc-dc converter.

### 4.4.4 VSC Controller

Voltage source converters interface the dc-link with electric machines. MG1 and MG2 are controlled with the VSC controller to generate the required torque determined by the PSG controller. **Fig. 4.18** shows the block diagram of VSC controller.

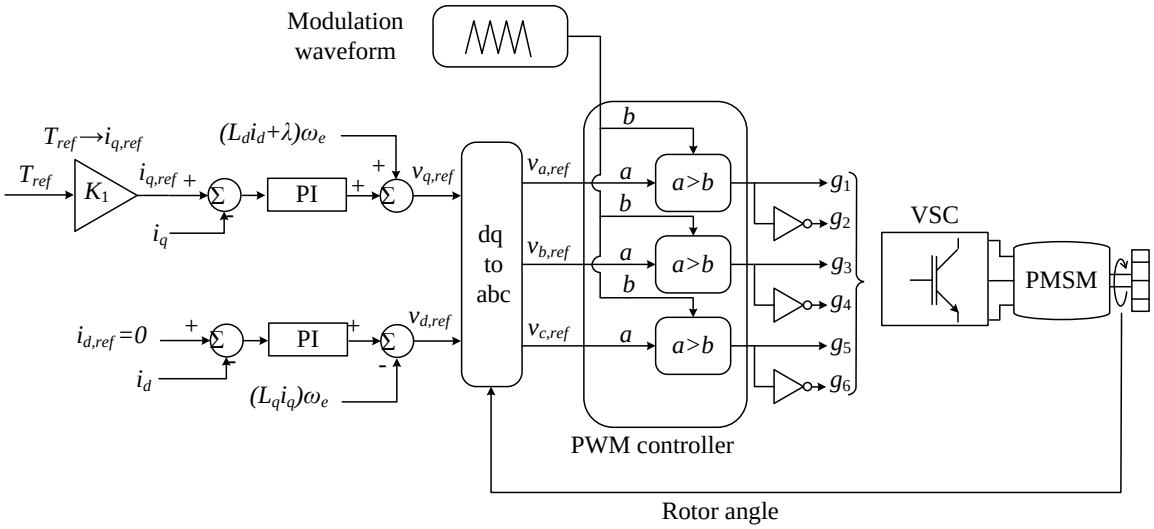


**Fig. 4.18 The VSC controller**

The controller receives the reference torque from PSG controller and determines the reference voltages on *d* and *q* axes. These reference voltages are then translated to abc voltages and eventually to the gate commands as shown in **Fig. 4.18**.

## 4.5 Vehicle Parameters

Basic vehicle parameters used in its transient simulation are listed in **Table 4-3**. These parameters are identical to the parameters of a Toyota Prius. The body parameters such as curb weight and frontal area are used in the vehicle dynamics block to calculate the applied forces to the vehicle. Distance of the center of gravity from the ground and front and rear axles distance from center of gravity are used to calculate the weight distribution of the vehicle on each axel. Wheel parameters are used in the tire model to calculate wheel speed and the propelling force. This force is then sent to the vehicle dynamic model and used for vehicle speed calculations.

**Table 4-3 Vehicle parameters in transient model**

| Parameter | Value |
|---|---|
| Curb weight ($W$) | 1330 [kg] |
| Passenger weight | 80 [kg] |
| Frontal area ($A_f$) | 2.23 [$m^2$] |
| Aerodynamic coefficient ($C_d$) | 0.26 |
| Air density ($\rho$) | 1.204 [$kg/m^3$] |
| Gravitational acceleration ($g$) | 9.8 [$m/s^2$] |
| Front axle distance from center of gravity ($L_a$) | 0.75 [m] |
| Rear axle distance from center of gravity ($L_b$) | 0.75 [m] |
| Center of gravity distance from ground ($h$) | 0.4 [m] |
| Wheel radius ($R_w$) | 0.2797 [m] |
| Wheel viscous coefficient ($B_f$) | 0.02 |
| Wheel inertia ($J_w$) | 4.5 [$kg.m^2$] |

Two permanent magnet synchronous machines, MG1 and MG2 are used in the drive-train. **Table 4-4** lists the power and torque rating for these machines and also the ICE parameters.

**Table 4-4 Power rating of motor, generator and the ICE**

| Parameter | Value |
|---|---|
| Engine maximum power | 57 [kW] |
| Engine maximum torque | 115 [N.m] |
| Motor maximum power | 50 [kW] |
| Motor maximum torque | 400 [N.m] |
| Generator maximum power | 25 [kW] |
| Generator maximum torque | 200 [N.m] |

The power-split gear device and transmission specifications are listed in **Table 4-5**. These parameters are used in the power-split block of the drive-train model.

**Table 4-5 Transmission specifications**

| Parameter | Value |
|---|---|
| Number of Ring gear teeth ($R$) | 78 |
| Number of Sun gear teeth ($S$) | 30 |
| Final drive ratio ($R_f$) | 4.113 |

## 4.6 Drive-Train Modes of Operation

Using the controllers explained in section 4.4, the drive-train is able to operate in different modes from a power-flow point of view. These modes of operation are explained in the following subsections.

### 4.6.1 Electric Mode

The primary goal of the vehicle controller is to provide the main part of the demand power from the battery storage in order to reduce the involvement of the ICE in propulsion. Therefore, assuming that the battery state-of-charge is in the desired range

and that the power demand is less than the maximum limit of battery power, the vehicle controller prefers to only engage the battery. The electric mode is the cleanest mode of operation. The propelling torque in this mode is generated by MG2 alone. The internal combustion engine does not operate in this situation, which reduces the fuel consumption to zero. However the vehicle controller only deploys this mode when the demand power is below the maximum battery power and when the state of charge allows. This usually happens in slow driving conditions such as traffic jams or driving in congested urban areas. Note that this mode of operation reduces the vehicle emissions significantly compared to a conventional vehicle, as the internal combustion engine has the lowest efficiency and highest amount of emissions in low speed operation [66], [67]. **Fig. 4.19** shows the flow of power in the electric mode of operation.

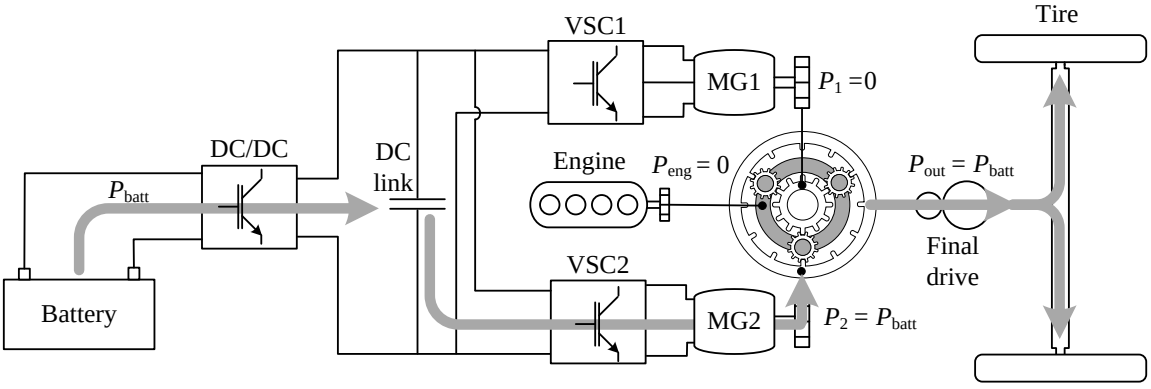


**Fig. 4.19 Energy flow diagram for electric mode.**

When the drive-train operates in this mode, VSC2 draws current from the dc-link. This causes the dc-link voltage to drop. The dc-dc controller tries keeps the dc-link voltage constant by transferring energy from battery to dc link. This can happen only when the battery state of charge is in the desired range and the battery current is not exceeding the maximum value. If the power demand increases, for instance when the

vehicle accelerates, the dc-link voltage may not be maintained by the battery and the vehicle controller has to engage the engine.

### 4.6.2 ICE + Battery Mode

When the power demand exceeds the maximum battery power, the ICE is also used to assist in providing the propulsion. The engine provides part of the demand power (assigned by vehicle controller) with the maximum possible efficiency [68], [69]. This means that the engine has to operate in the operating point calculated by the vehicle controller. This is achieved by appropriate control of MG1, as explained in section 4.4.2. **Fig. 4.20** shows the energy flow diagram in this mode of operation. As shown, the engine and the electric motor both provide power to the wheels.

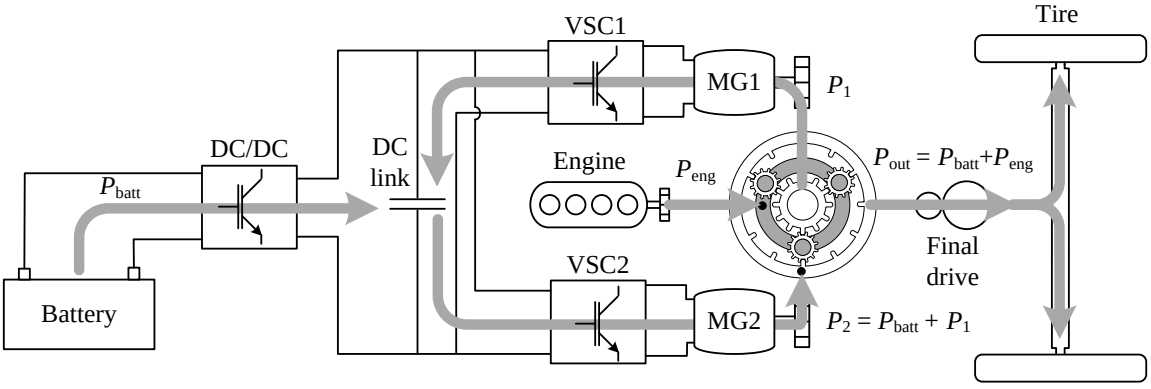


**Fig. 4.20 Controller for ICE + battery mode.**

In this mode, VSC1 injects current to dc-link while VSC2 is absorbing current. Therefore dc-link controller will absorb less current from the battery and the battery current remains in a safe level. Note that by circulating the power between the two electric machines, the ICE's operating point is controlled.

### 4.6.3 Regeneration (Regenerative Braking)

Regenerative braking is one of the advantages of HEVs and PHEVs over conventional gas-powered vehicles. Regenerative braking saves part of the vehicle's kinetic energy during braking intervals and improves the vehicle efficiency. The energy flow diagram of the vehicle in regenerative braking mode is shown in **Fig. 4.21**. Note that in this figure the flow of power is from the wheels to the battery and MG2 will operate as a generator.

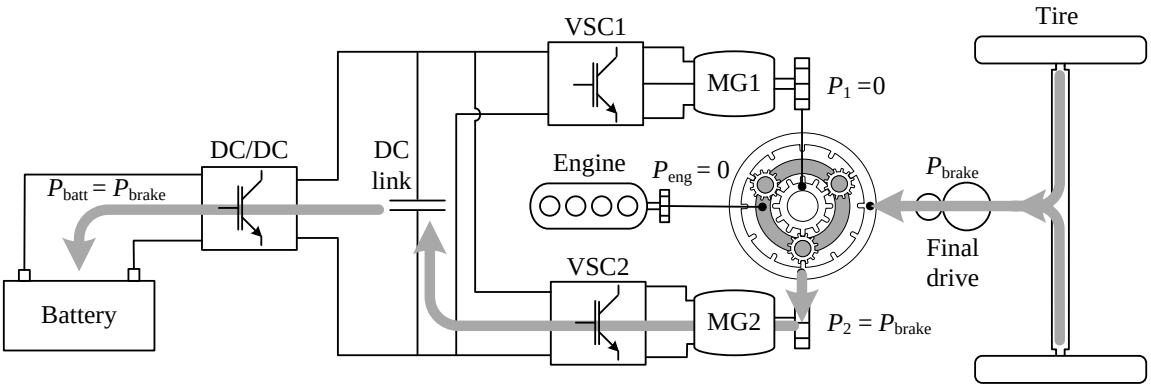


**Fig. 4.21 Energy flow diagram for regenerative brake mode.**

### 4.6.4 Driving and Charging

When the battery state-of-charge is below the desired level, the battery storage must be charged, with charging power coming from the ICE. A portion of the ICE power is converted to electrical form using MG1 and then stored in the battery. The extra power from the ICE is again converted back to mechanical form in MG2, and is given to wheels. **Fig. 4.22** shows the power flow diagram of the drive-train in this mode of operation.

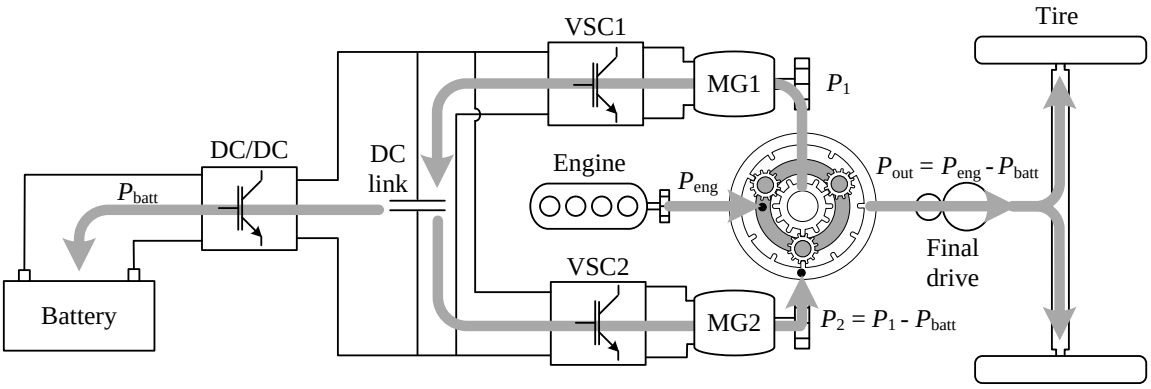


**Fig. 4.22 Power flow in the driving and charging mode.**

## 4.7 Simulation Results and Discussion

This section presents and discusses the simulation results for different components and the system as a whole. A short driving-cycle consisting of slow, moderate and fast speed is used for this simulation. **Fig. 4.23** shows the reference speed and the actual speed of the vehicle for this driving-cycle.

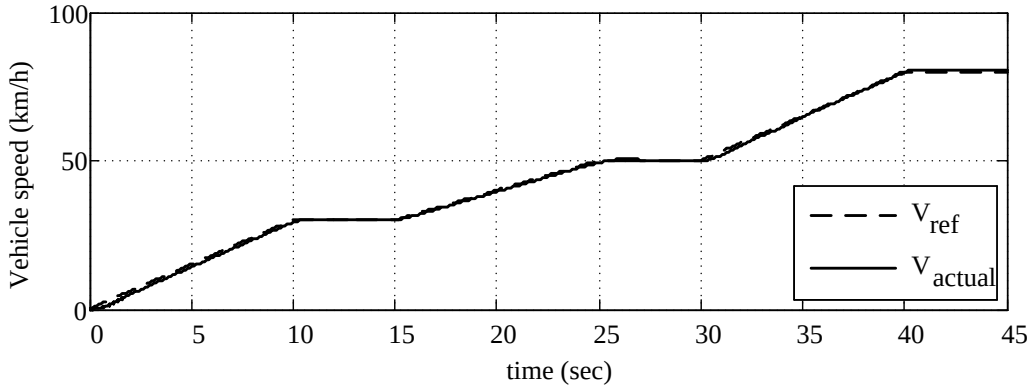


**Fig. 4.23 Vehicle speed**

The driving-cycle has a period of slow driving (30 km/h) over [10,15] sec, a moderate speed period (50 km/h) over [25,30] sec, and a fast driving period (80 km/h) over [40,45] sec. The drive-train can follow the reference speed as shown in the figure above.

The vehicle controller controls the power distribution in the drive-train to achieve the maximum efficiency. The power distribution is shown in **Fig. 4.24**. In the low speed region of the driving-cycle the demand power is in the range that the battery can provide the power. In the moderate region, the power demand momentarily exceeds the maximum battery power. As shown in this figure, the engine reference power becomes non-zero momentarily right after $t$=32 sec. When the demand power cannot be met using battery, the vehicle controller starts the engine and the engine provides additional power for propulsion.

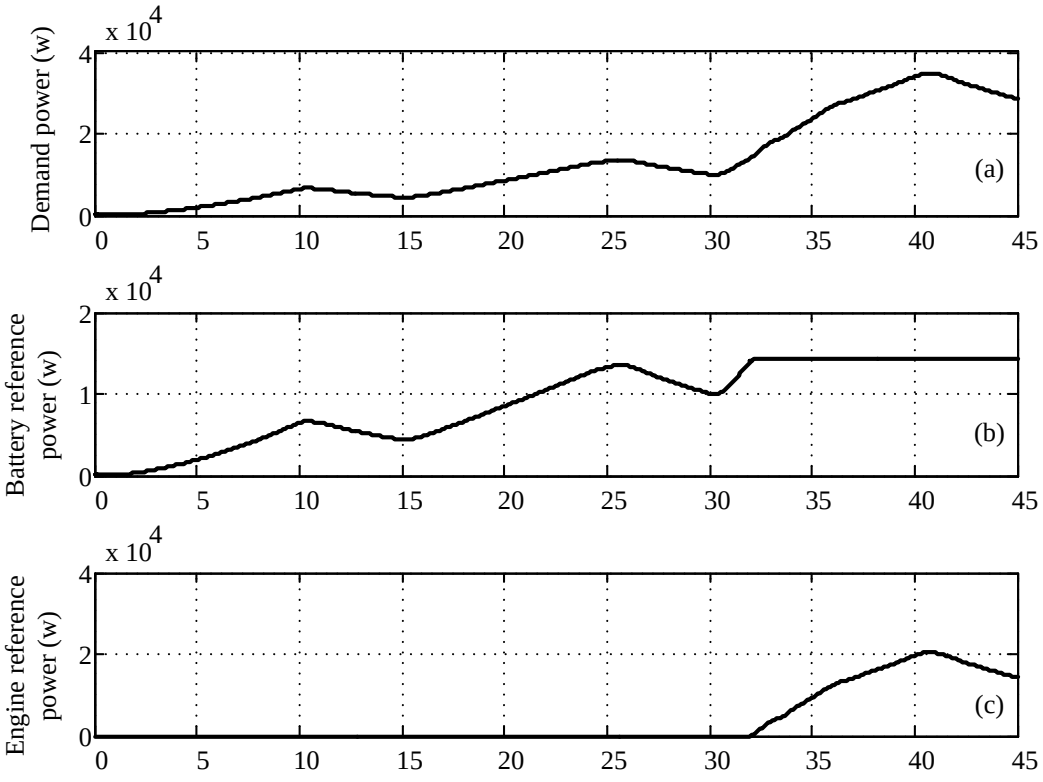


**Fig. 4.24 Simulation results (a) demand power (b) battery reference power**

**(c) engine reference power**

The vehicle controller also determines the operating point of the engine. The engine speed and torque are shown in **Fig. 4.25**. The engine reference speed and torque are zero

before *t*=32 sec. The engine actual torque follows the reference in this period and remains at zero. The engine speed as shown in the figure is not following the reference value. This is due to "releasing" the engine by the PSG controller when the engine is not providing power. When the engine is off, MG1 does not try to control the engine speed. This eliminates unnecessary power consumption by MG1 to keep the engine stationary, when it is not necessary.

At *t*=32 sec, the demand power exceeds the battery maximum power. This causes the engine to turn on end provide power for the drive-train as shown below.

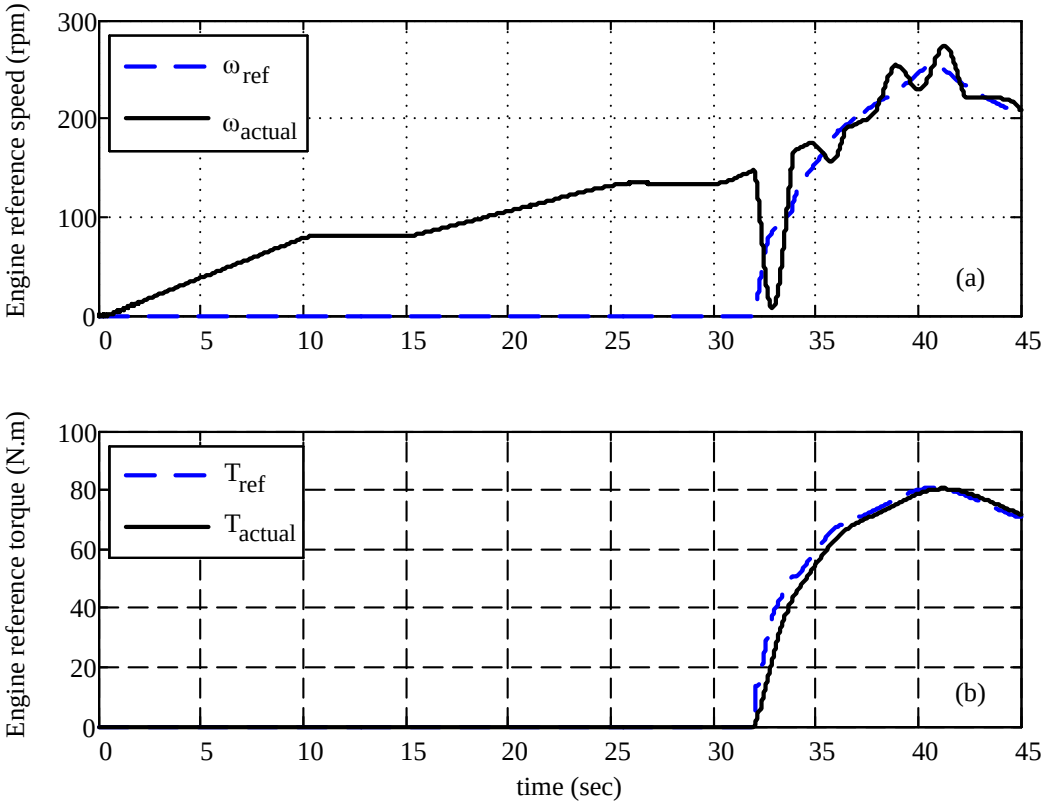


**Fig. 4.25 Simulation results (a) engine speed (b) engine torque.**

As shown in this figure, after *t*=32 sec, both speed and torque of the engine follow the reference value determined by the vehicle controller.

MG1 and MG2 speeds are shown in **Fig. 4.26**. MG1 speed changes to control the engine speed to the value determined by the vehicle controller. The MG1 speed becomes non-zero when the engine reference speed receives a non-zero value for the first time (*t*=32 sec). This speed will vary in a way that engine speed follows its reference value. MG2 speed depends on vehicle speed since it is mechanically coupled to the final drives and wheels. As shown in **Fig. 4.26**, the MG2 speed pattern is identical to vehicle speed pattern.

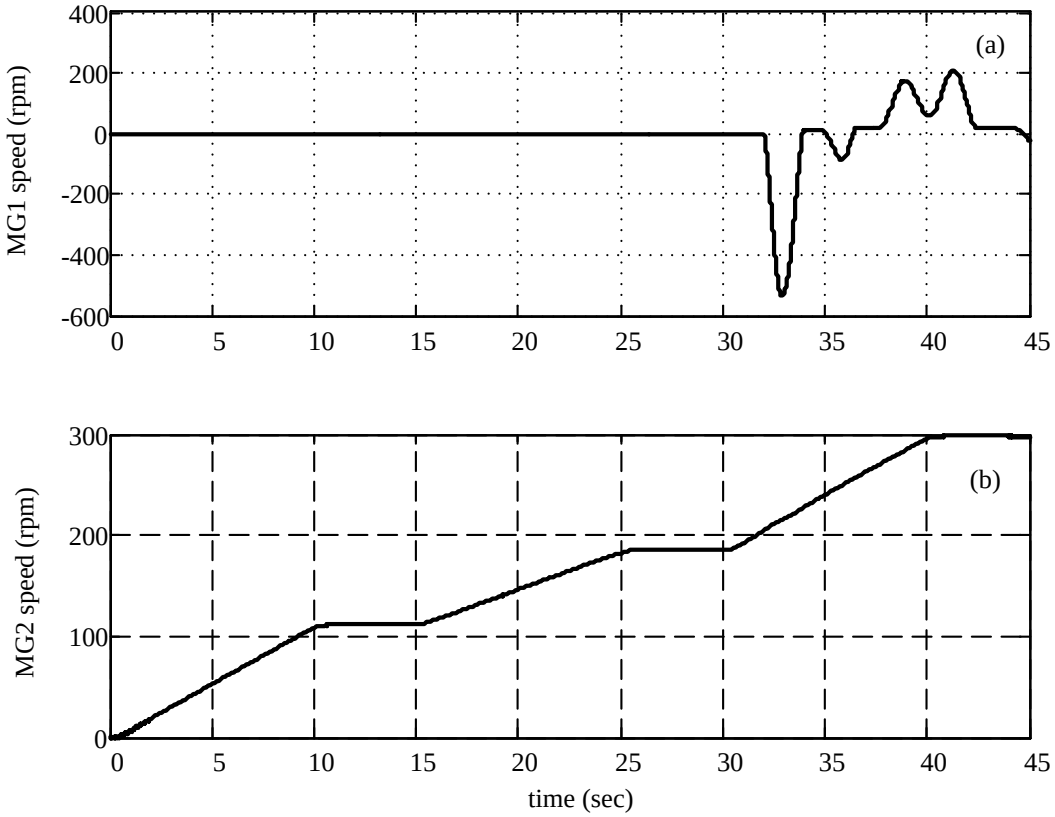


**Fig. 4.26 Electric machines speed (a) MG1 (b) MG2**

**Fig. 4.27** shows the torque produced by MG1 and MG2. MG1 torque is determined by the vehicle controller to control the engine speed. As illustrated in this figure, MG1 does not provide any torque when the engine is not engaged by the vehicle controller. When vehicle controller initiates a command to start the engine, MG1 also operates to keep the

engine in the proper speed. MG2 torque is controlled by the driver model and this torque is directly going to the final drive and wheels. MG2 torque for this driving-cycle is shown in **Fig. 4.27**(b).

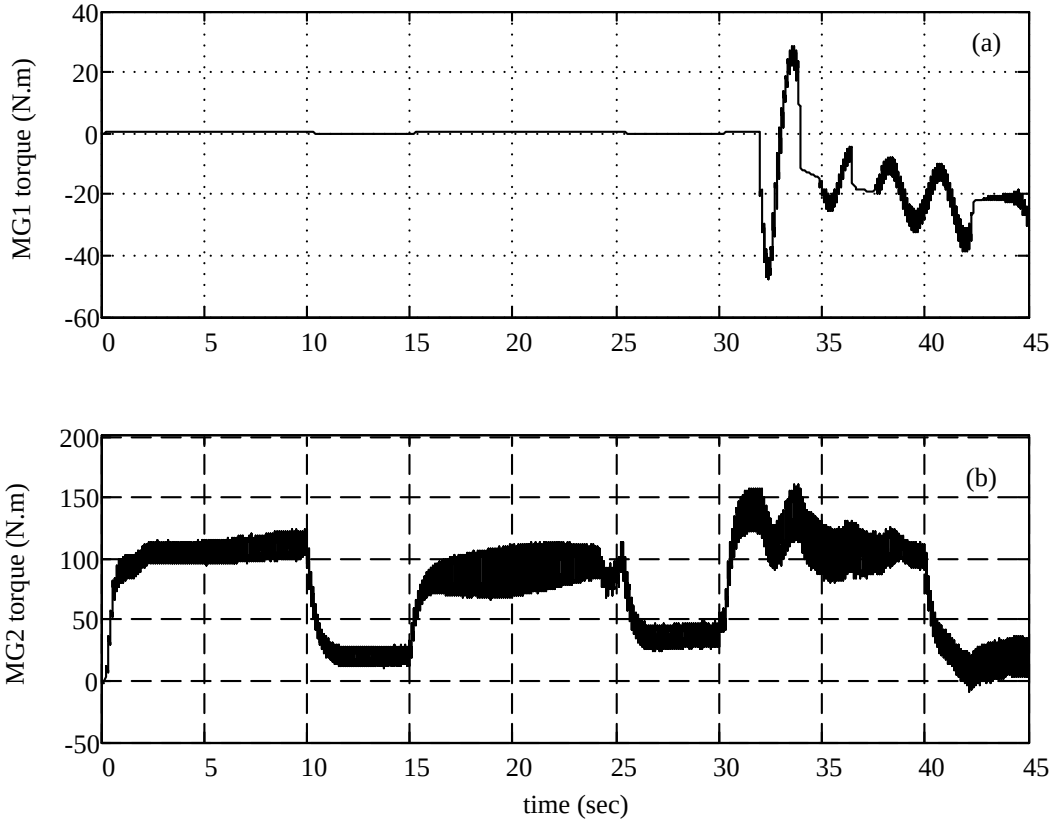


**Fig. 4.27 Electric machine torques (a) MG1 (b) MG2**

Battery current, dc link voltage and battery state-of-charge are shown in **Fig. 4.28**. The battery current for this drive-train is limited to 70A (this limit originates from the maximum battery power limit). The dc-link controller tries to maintain a constant voltage of 650V on the dc-link. This is done by controlling the battery current. When the demand power is more than battery maximum power, the dc-link voltage drops and battery current cannot compensate the current drawn by MG2 from the dc-link. Under this condition, the vehicle controller increases the reference torque of the ICE. This puts MG1 in generating mode and the dc-link voltage improves after $t$=40 sec (**Fig. 4.28**).

The battery state-of-charge has an initial value of 100% in this simulation. The SOC drops though the simulation, since the battery is used for propulsion and there is no charging period.

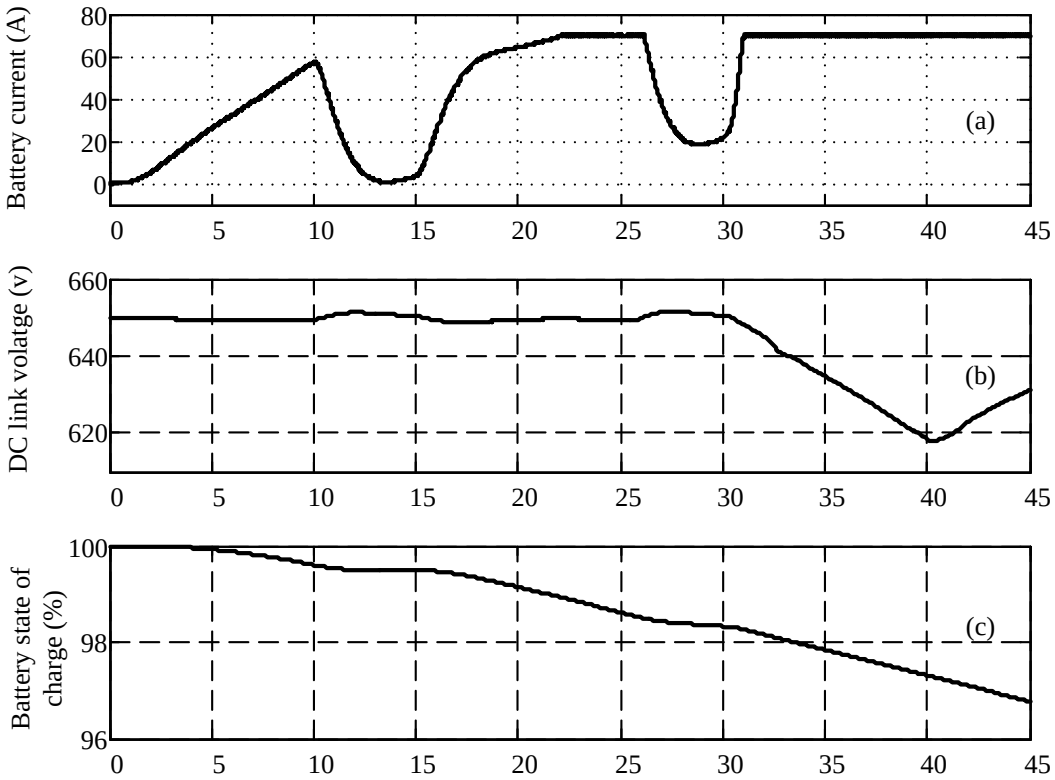


**Fig. 4.28 Simulation results (a) battery current (b) dc-link voltage (c) battery SOC**

The locus of the operating point of the engine is shown in **Fig. 4.29**. This figure shows that for any demand power, the engine has operated in the most efficient point for that power. For example all points on the constant power of 7kW provide 7kW of power but at different efficiencies ranging from 10% (above 500rpm) to more than 30% (point A) the same output power, but only at one point is the engine efficiency the maximum value. The vehicle controller and PSG controller control MG1 in a way that the engine operates in this maximum efficiency point for the determined ICE power given by the vehicle controller.

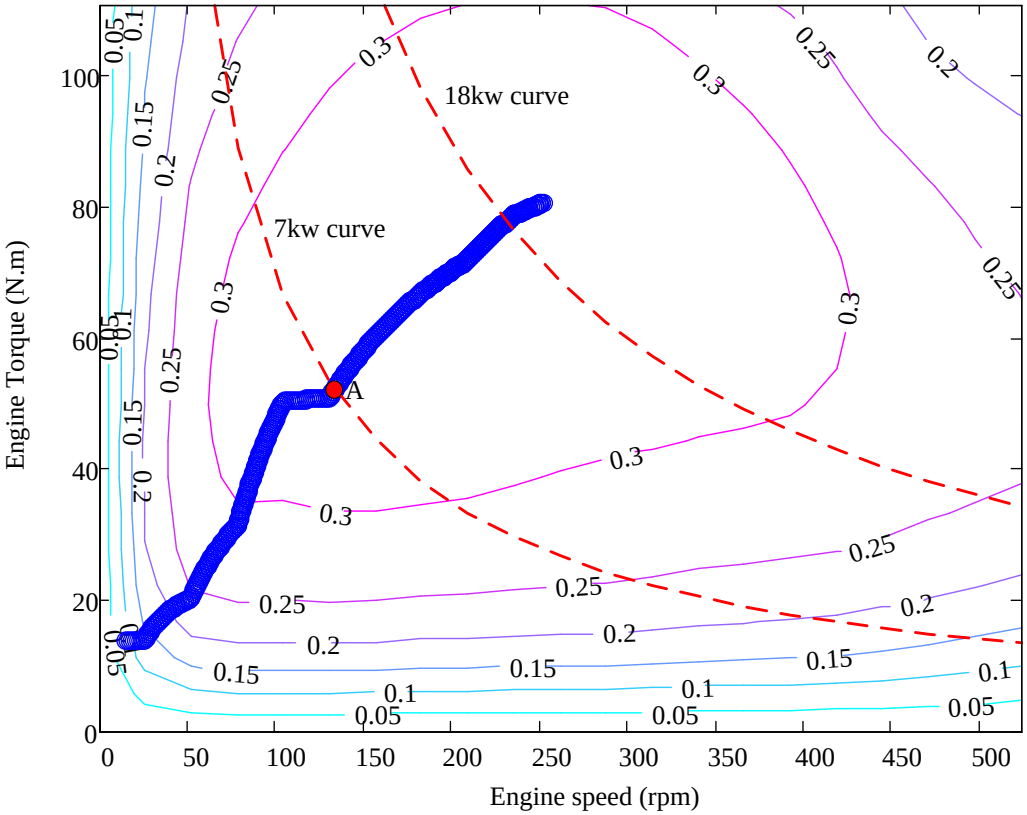


**Fig. 4.29 Engine operating point locus**

## 4.8 Chapter Summary and Contributions

In this chapter a detailed model of PSG based hybrid drive-train was developed in MATLAB/Simulink. This model includes detailed models of the power electronic converters and electrical machines. A prominent use of this transient model is its implementation on a real-time simulator and interfacing with real hardware components in a hardware-in-loop (HIL) setup. In the particular HIL setup developed in this research, actual batteries are interfaced with a real-time simulator; this will allow to study the transient behaviour of the battery as well as to test emerging new battery technologies.

# Chapter 5

# Dynamic Average-Value Modeling of Power Electronic Converters

Modeling and simulation of hybrid vehicular drive-trains is an essential step in their design, concept-evaluation and optimization [70]. As described in Chapter 3, there are different drive-train models tailored for different applications or studies. The model developed in Chapter 4 is a transient model, which simulates the drive-train with a high level of details and is capable of simulating fast transients within the drive-train such as the ones created by switching converters. Using this transient model various studies such as controller tuning, motor-drive torque oscillation minimization or converter transient performance optimization can be done. The transient model, however, has a major drawback, which is its high computational intensity. For a large class of simulation-based studies, a less detailed model with less computational burden and hence a faster simulation time is sufficient.

In many drive-train studies slow-varying variables such as vehicle speed, battery current and dc link voltage are the main variables of interest and fast switching transients and oscillations are ignored due to their typically small magnitudes [71], [72]. These studies often need to simulate the model for a long time, e.g. a few days or weeks.

Simulating the drive-train using a transient model for such lengths of time translates to massive computing requirements due to the complexity of the model. Therefore, the user often has to make a compromise between accuracy of the results for transients and the computational affordability of the simulation.

Traditionally simulators of hybrid vehicular systems have been tailored for specific studies by neglecting the dynamics of certain subsystems. For long-term studies involving fuel economy, acceleration performance and emissions, power-electronic converters and electric motors are often modeled with less detail to reduce the computational intensity of their simulations. On the other hand, when transients within the electrical subsystem are concerned, slower acting mechanical subsystems are treated as in steady state.

With the increasing use of digital transient simulation tools in vehicular power systems studies, it is desirable to include an adequate representation of the electrical subsystem dynamics, particularly of the power electronic converters. A simulation platform of such capability will allow a realistic view of the vehicular power-electronics and will be particularly suited for specialized studies involving repetitive (e.g. simulation-based design [37], [73], [74]) and real-time simulations [75], [76]. It also serves as a platform to interface vehicular models with power system simulators when vehicle-grid interactions need to be studied.

One efficient way to reduce simulation intensity while retaining the dynamic transients is to use the so-called dynamic average-value models for power electronic converters [77]. Such average models preserve the input-output dynamic behavior of the converters but neglect the high-frequency switching phenomena and the associated harmonics. This approximation is deemed sufficient for studying power-electronic-

intensive hybrid drive-trains, as the impact of low-amplitude high-frequency switching ripple on the overall vehicle dynamics is negligible. These models additionally allow much larger simulation time-steps to be used and therefore reduce the computational burden of the simulations. For example, in [78] the inverter component-level switching losses are modeled in an averaged sense.

A computationally-efficient vehicular power system model is also highly desired when fast yet accurate simulation of vehicle-to-grid and grid-to-vehicle is desired. By neglecting the switching artifacts and faster dynamics, one may use a more accurate model of vehicular systems when considering charging station deployment [79], chargers impacts on power quality and transformer life expectancy [80], peak shaving [81], load shedding in dc zonal distribution systems [82], stochastic load-demand formulation of chargers in distribution systems [83], load forecasting [84], PHEV penetration impact [85], and optimal charging profiling and coordination [86].

There is extensive literature on the subject of average modeling for various power electronic converters and for different studies [77], including dc-dc converters [87]-[90], ac-dc rectifiers [91], [92] and voltage source converters [77], [93]. In this chapter, the electrical sub-system of the drive-train is modeled using dynamic averaging techniques for its two dc-ac and one bi-directional dc-dc converters (refer to **Fig. 4.1**).

## 5.1 Average Modeling of Voltage Source Converters

**Fig. 4.14** shows the schematic diagram of the VSC used in the drive-train. This converter employs standard sinusoidal pulse-width modulation (PWM) to synthesize the three-phase voltages with desired magnitude and frequency at the terminal of the motor.

Modeling of this scheme including its switching is straightforward and well documented [64], [65]. In this section mathematical derivation of an average model for the converter is described.

### 5.1.1 Model Derivation

The sinusoidal PWM is based on comparison of a fundamental-frequency sinusoidal reference with a high-frequency triangular carrier waveform as shown in Fig. 5.1(a) for one of the legs of the VSC. The high-frequency switching instants of the converter transistors are determined by the multiple crossings of the two waveforms. To develop a dynamic average model of the sinusoidal PWM converter, it is assumed that the frequency of the triangular carrier waveform is much higher than that of the sinusoidal reference. This implies that the reference waveform can be assumed to have an essentially constant value during each switching interval, i.e. one period of the carrier waveform. **Fig. 5.1** (b) shows in more details the triangular waveform, the reference signal (approximately constant within the shown interval) and the resulting waveform in a pulse-width modulated phase-to-ground voltage $v_{ag}$.

As shown in **Fig. 5.1**(a), the generated firing pulse train will produce a corresponding train of voltage pulses with modulated widths at the output of the converter leg. In the dynamic average modeling, the high-frequency switching phenomena is neglected and the output waveform is represented only using its dynamic average-value, which is calculated during each switching interval and varies depending on the local value of the reference waveform. The dynamic average-value of an arbitrary variable $x(t)$ over period $T_{sw}$ is defined as follows.

$$\hat{x}(t) = \frac{1}{T_{sw}} \int_{t-T_{sw}}^{t} x(u)du \tag{5.1}$$

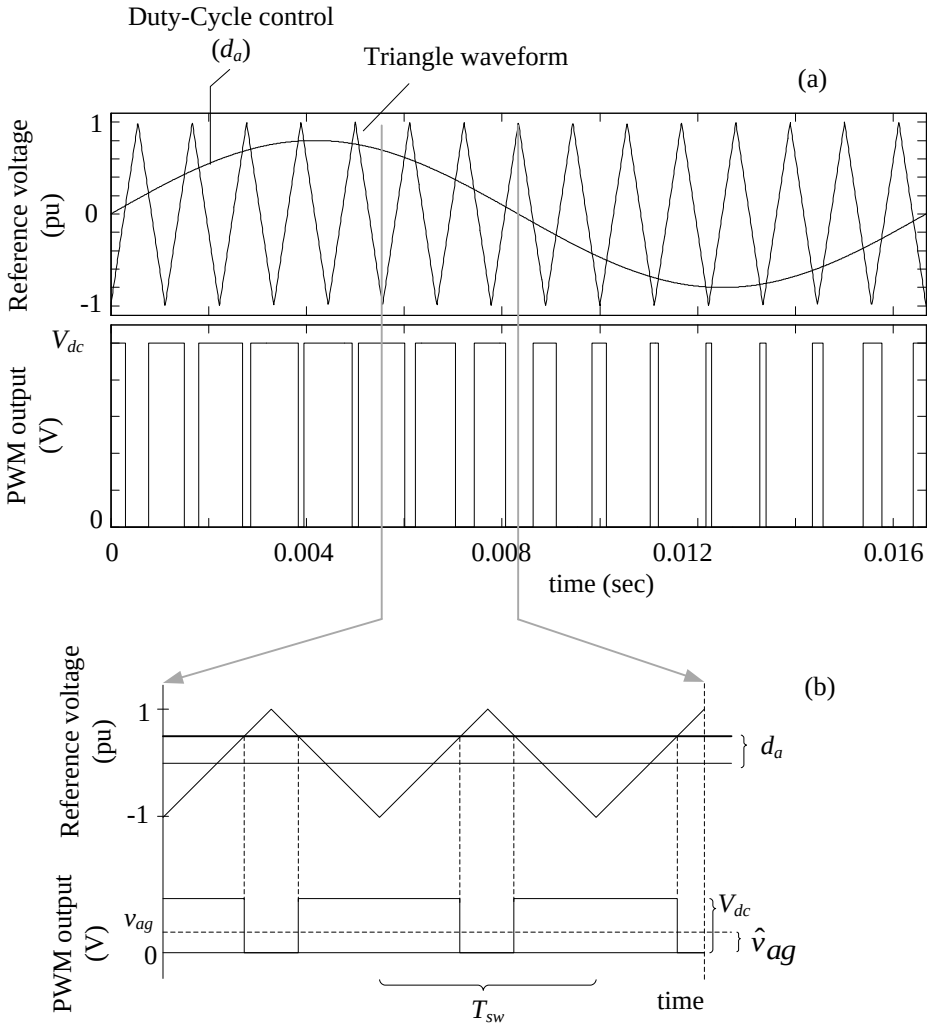


**Fig. 5.1 Sinusoidal PWM firing pulse generation:**

**(a) carrier, modulating and PWM output waveforms; (b) detailed view of a switching interval.**

Using sinusoidal PWM and (5.1), the dynamic average-value of the output phase voltage in **Fig. 5.1**(b) is obtained as follows [64].

$$\hat{v}_{ag} = 0.5(1 + d_a)V_{dc} \tag{5.2}$$

where $\hat{v}_{ag}$ is the average value of the phase *a* to ground voltage, $d_a$ is the duty cycle variable of phase *a*, and $V_{dc}$ is the dc link voltage. Similar equations can be written for other phases as follows.

$$\begin{aligned}\hat{v}_{bg} &= 0.5(1+d_b)V_{dc}\\ \hat{v}_{cg} &= 0.5(1+d_c)V_{dc}\end{aligned} \tag{5.3}$$

In a balanced three-phase system $d_a$, $d_b$ and $d_c$ must sum to zero. Therefore, the average neutral point voltage to the ground ($\hat{v}_{ng}$) is as follows.

$$\hat{v}_{ng} = \frac{1}{3}(\hat{v}_{ag} + \hat{v}_{bg} + \hat{v}_{cg}) = 0.5v_{dc} \tag{5.4}$$

Using (5.1)–(5.4), the average line-to-neutral voltages in this three-phase system are as shown below.

$$\begin{aligned}\hat{v}_a &= \hat{v}_{an} = \hat{v}_{ag} - \hat{v}_{ng} = 0.5d_aV_{dc}\\ \hat{v}_b &= \hat{v}_{bn} = \hat{v}_{bg} - \hat{v}_{ng} = 0.5d_bV_{dc}\\ \hat{v}_c &= \hat{v}_{cn} = \hat{v}_{cg} - \hat{v}_{ng} = 0.5d_cV_{dc}\end{aligned} \tag{5.5}$$

where $\hat{v}_a$, $\hat{v}_b$ and $\hat{v}_c$ are the average values of phase *a*, *b* and *c* voltages, respectively. To produce a balanced three-phase system, the modulation indices should have the same magnitude and be shifted by 120° as follows.

$$\begin{aligned}d_a &= d\cos(\theta_c)\\ d_b &= d\cos(\theta_c - \tfrac{2\pi}{3})\\ d_c &= d\cos(\theta_c + \tfrac{2\pi}{3})\end{aligned} \tag{5.6}$$

where *d* is the modulation index magnitude for the three phase voltages, and $\theta_c$ is the converter voltage angle (determined by VSC controller). Substituting (5.6) into (5.5), the average three phase voltages are as follows.

$$\begin{aligned}\hat{v}_a &= 0.5dv_{dc}\cos(\theta_c)\\ \hat{v}_b &= 0.5dv_{dc}\cos(\theta_c - \tfrac{2\pi}{3})\\ \hat{v}_c &= 0.5dv_{dc}\cos(\theta_c + \tfrac{2\pi}{3})\end{aligned} \tag{5.7}$$

In a so-called converter reference frame whose *q*-axis is locked to $\theta c$ (*q*-axis leads the *d*-axis) the voltage equations in (5.7) will yield the following dq0 components:

$$\begin{bmatrix}\hat{v}_d^c\\ \hat{v}_q^c\\ \hat{v}_0^c\end{bmatrix} = \frac{2}{3}\begin{bmatrix}\sin(\theta) & \sin\left(\theta-\frac{2\pi}{3}\right) & \sin\left(\theta+\frac{2\pi}{3}\right)\\ \cos(\theta) & \cos\left(\theta-\frac{2\pi}{3}\right) & \cos\left(\theta+\frac{2\pi}{3}\right)\\ \frac{1}{2} & \frac{1}{2} & \frac{1}{2}\end{bmatrix}\begin{bmatrix}\hat{v}_a\\ \hat{v}_b\\ \hat{v}_c\end{bmatrix} = \begin{bmatrix}0.5v_{dc}\\ 0\\ 0\end{bmatrix} \tag{5.8}$$

The above expression determines the *d*, *q* and 0 components of the average voltages that the three-phase VSC generates when it is supplied with the voltage $V_{dc}$ (the third component, 0 component, is always equal to zero in a balanced system and it will be neglected from now on). An average model for the VSC in *dq* frame consists of two voltage sources as defined in (5.8).

It should be noted that when the converter exchanges real power with the rest of the system, e.g. when it supplies power to the ac motor or absorbs power during braking, its dc link voltage will rise or fall accordingly. In order to account for the dynamic variations of the dc voltage, its line current must be known and be modeled as a current source that correspondingly charges or discharges the capacitor. The dc line current can be derived using the principle of conservation of energy [77]. The outgoing real power *P* for three-phase system is given as follows.

$$P = \frac{3}{2}\left\|\bar{v}_{dq}\right\|.\left\|\bar{i}_{dq}\right\|\cos(\varphi) \tag{5.9}$$

where $\bar{v}_{dq}$ and $\bar{i}_{dq}$ are the voltage and current vectors in the *dq* reference frame, and $\varphi$ is the load power factor angle. In terms of dc-side quantities, the instantaneous power is as follows.

$$P = V_{dc} I_{dc} \tag{5.10}$$

Assuming a lossless converter and based on (5.9)–(5.10), the dc current can be calculated as follows.

$$i_{dc} = \tfrac{3}{4} d \cos(\varphi) \left\| \bar{i}_{dq} \right\| \tag{5.11}$$

The resulting dynamic average model of the VSC is shown in **Fig. 5.2**.

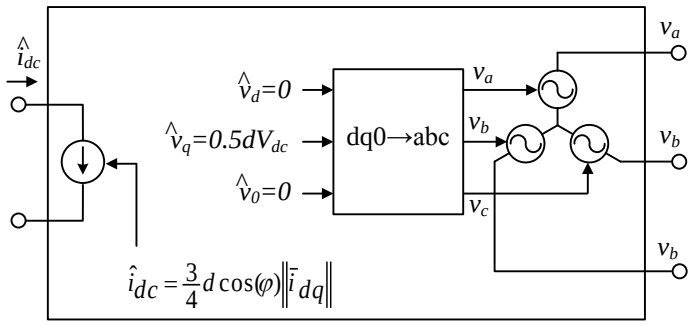


**Fig. 5.2 Dynamic average model of a two-level voltage-source converter with sinusoidal PWM.**

Note that this model is for a loss-less converter. Implementing converter losses in the average model is possible but it makes the model much more complicated [87].

## 5.1.2 Model Verification

To demonstrate the operation of the dynamic average model developed for the VSC, a simple example case is simulated. In the circuit shown in **Fig. 5.3**, a VSC is connected to a permanent magnet synchronous machine. The VSC average model is connected to the dc link, represented by an ideal voltage source in this figure. The motor is fed by three voltage sources that are the outputs of the VSC average model as shown. The motor

current is determined by the machine model (PMSM). The torque of the motor is controlled using a proportional-integral (PI) controller, which controls the motor speed using a negative feedback loop. To control the torque produced by the motor a vector control method [65] is used. This is the same method in the transient model of the drive-train explained in Chapter 4. The vector control unit determines the duty cycle, *d*, and converter angle, $\theta_c$, for the converter. The dynamic averaged model of the converter determines the three-phase voltage on the terminals of PMSM. The PMSM model determines the line currents. The line currents are then transformed to *dq0* reference frame and fed back to the average converter model. Using these currents, the dc current is calculated by the average model (5.11) and is injected into the dc link using a dependent current source. The specifications of this example case system, its controller and motor, are given in **Table 5-1**.

**Table 5-1 Parameters of VSC model verification test**

| Parameter | Value | Description |
|---|---|---|
| $V_{dc}$ | 500 V | DC voltage |
| $f$ | 10 kHz | Switching frequency |
| $L_d$ | 0.8e-3 H | PMSM d-axis inductance |
| $L_q$ | 0.8e-3 H | PMSM q-axis inductance |
| $\lambda$ | 0.192 Wb | PMSM flux induced by magnet |
| $F$ | 0.089 N.m.s | Friction coefficient |
| $J$ | 0.005 kg.m$^2$ | Inertia |
| $P$ | 4 | Pole pairs |

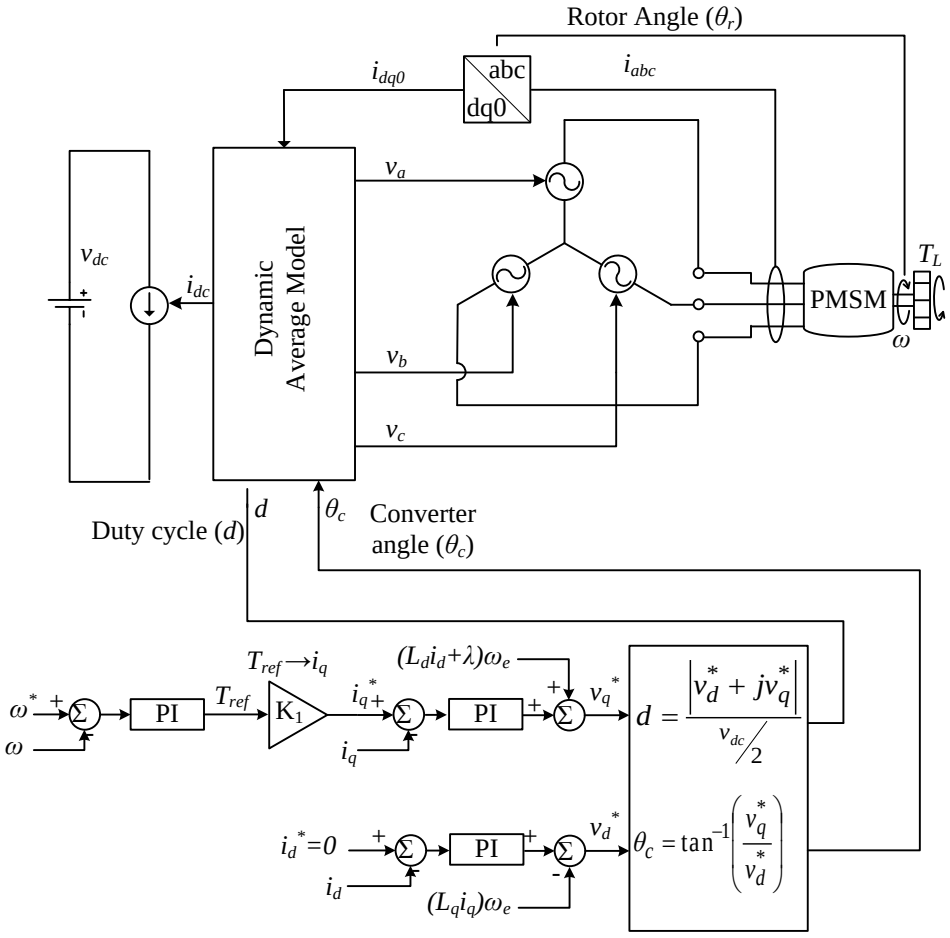


**Fig. 5.3 Average model of motor drive and its control.**

To compare the accuracy of results and also the speed of the dynamic average model, a detailed model for the same circuit is also developed. The detailed model uses a time step of 10 μs, while for the average model a much larger time step of 1 ms is used. Although the time step for the average model is one hundred times larger, both models produce essentially identical results for the slow dynamics of the system as shown in **Fig. 5.4** for the motor speed and torque and the slow variations of the ac current. It must however be noted that the average model does not show the switching nature of the VSC as the switching phenomena has been neglected by the assumptions of the averaging.

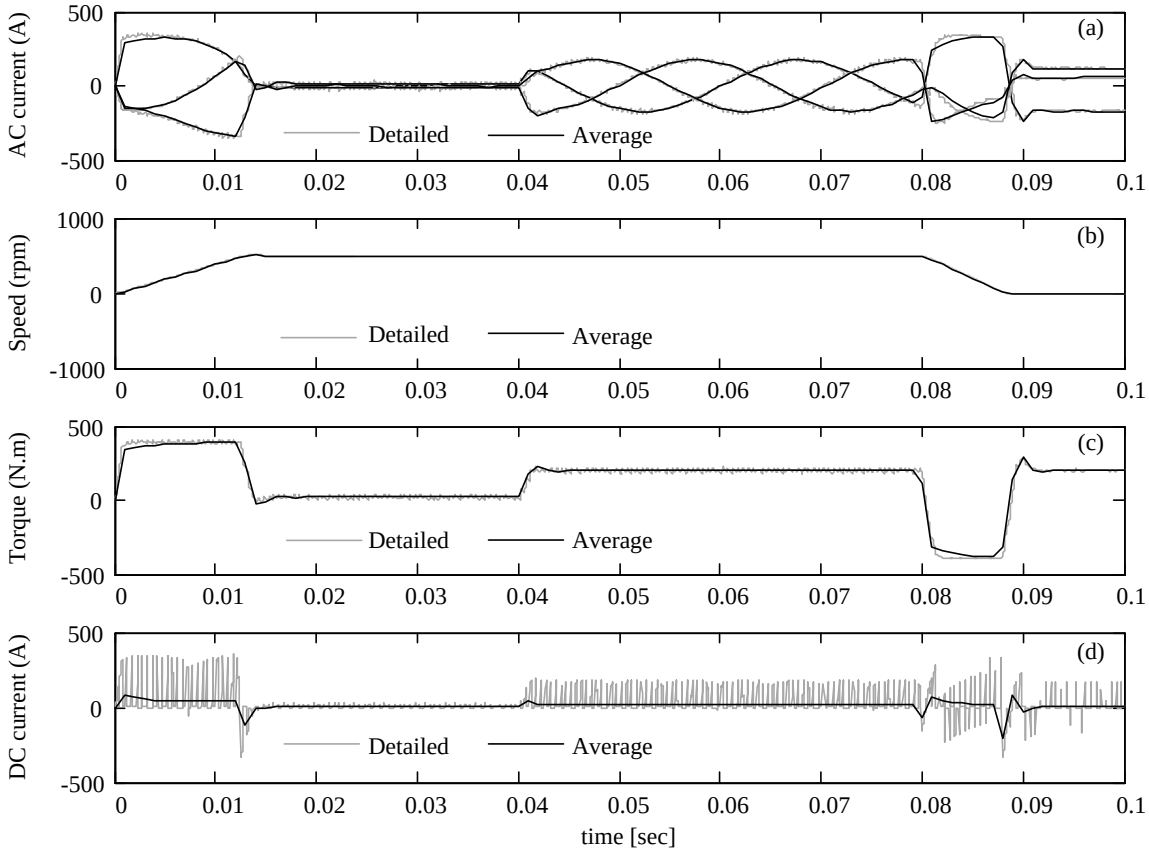


**Fig. 5.4 Simulation results: (a) ac current, (b) speed, (c) torque, (d) dc current.**

## 5.2 Average Modeling of DC-DC Converter

### 5.2.1 Model Derivation

The two general average-value modeling methods for the dc-dc converters are the averaged switch modeling and the state-space averaging [94]-[96]. In the state-space averaged model, a set of state-space equations are derived for each topology created by various permissible switch combinations and then averaged using appropriate weightings [97]. In the average switch modeling, the switching elements are replaced with dependent

current and/or voltage sources to create a circuit that is equivalent to the original in an average sense.

To make the interfacing of the components easier, the average switch modeling method is selected for this thesis. To obtain the average model for the switching cell, the average voltages and current of the switches, i.e. the IGBTs and the diodes, must be determined first. **Fig. 5.5** shows a general switched inductor cell used in dc-dc converters.

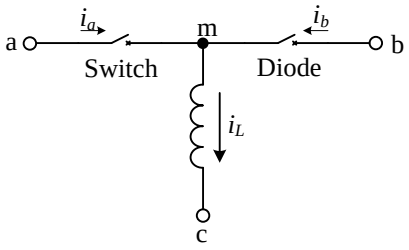


**Fig. 5.5 Basic switched-inductor cell of a dc-dc converter.**

Depending on the mode and conditions of operation, the converter may operate in either discontinuous or continuous conduction mode. To develop a general model that covers both modes of operation, in the following discussion the switch is modeled in discontinuous conduction mode. This model will work well for continuous conduction mode as well. The current waveforms of the switched inductor cell in **Fig. 5.5** in discontinuous mode are shown in **Fig. 5.6**.

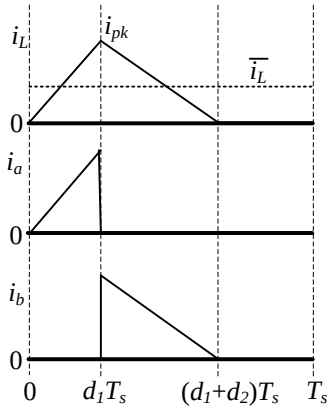


**Fig. 5.6 Current waveforms of the switched-inductor cell in discontinuous conduction mode.**

As shown, the switching interval $[0,T_s]$ is divided into three subintervals, i.e. $[0,d_1T_s]$, $[d_1T_s,(d_1+d_2)T_s]$ and $[(d_1+d_2)T_s,T_s]$. Here, $T_s$ is the switching period, $d_1$ is the duty cycle and $(1-d_1-d_2)\ T_s$ is the time over which the inductor current stays at zero. The switch in **Fig. 5.5** is closed for the $[0,d_1T_s]$ period therefore, $v_{mb}=v_{ab}$. For the period $[d_1T_s,(d_1+d_2)T_s]$ the diode conducts and thus $v_{mb}=0$. In the last period, i.e. $[(d_1+d_2)T_s,T_s]$, both the switch and the diode are open and the inductor current is zero, therefore, $v_{mb}=v_{cb}$. To find an average model for the switched-inductor cell, the switch current, $i_a$ and the diode voltage, $v_{mb}$ are found first in (5.12) and (5.13).

$$i_a = \begin{cases} i_L & 0 < t \le d_1T_s \\ 0 & d_1T_s < t \le (d_1+d_2)T_s \\ 0 & (d_1+d_2)T_s < t \le T_s \end{cases} \tag{5.12}$$

$$v_{mb} = \begin{cases} v_{ab} & 0 < t \le d_1T_s \\ 0 & d_1T_s < t \le (d_1+d_2)T_s \\ v_{cb} & (d_1+d_2)T_s < t \le T_s \end{cases} \tag{5.13}$$

Based on Fig. 5.6, the following expressions for the average switch current and the average diode voltage are obtained over one switching period.

$$\bar{i}_a = \frac{d_1\bar{i}_l}{d_1+d_2} \tag{5.14}$$

$$\bar{v}_{mb} = d_1\bar{v}_{ab} + (1-d_1-d_2)\bar{v}_{cb} \tag{5.15}$$

Note that in continuous conduction mode, $d_1+d_2=1$ and in discontinues conduction mode, $d_1+d_2<1$. An expression to determine the value of $d_1+d_2$ based on the value of $d_1$ (control variable) and other known variables in the system can be obtained as described below. Note that the inductor peak current $i_{pk}$ is expressed as follows.

$$i_{pk} = \frac{v_{ac}}{L} d_1 T_s \tag{5.16}$$

The average inductor current, $\bar{i}_L$ can then be calculated as:

$$\bar{i}_L = \frac{i_{pk}}{2}(d_1 + d_2) \tag{5.17}$$

and therefore, $d_1+d_2$ is equal to the following.

$$d_1 + d_2 = \frac{2L\bar{i}_L}{d_1 T_s v_{ac}} \tag{5.18}$$

Using (5.16), (5.17) and (5.18), the average model for the switch is developed as shown in **Fig. 5.7** [94].

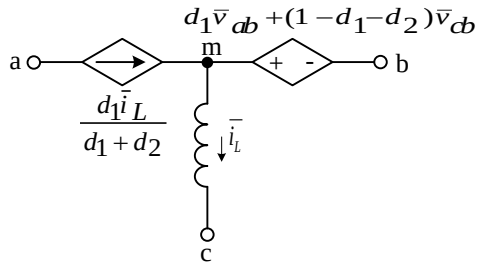


**Fig. 5.7 Averaged circuit model of the basic switched-inductor cell.**

Based on the averaged switch model, the combined average model for the bidirectional dc-dc converter is developed. In the first step, the buck and the boost converters are modeled separately, and in the second step these models are combined to create a single model for the bidirectional converter. **Fig. 5.8**(a) shows the dc-dc converter operating in the buck mode. Using the average model for the switched-inductor cell, the corresponding average model of the converter in this mode of operation is shown in **Fig. 5.8**(b). The converter in its boost mode of operation is shown in **Fig. 5.9**(a). The corresponding average model is shown in **Fig. 5.9**(b).

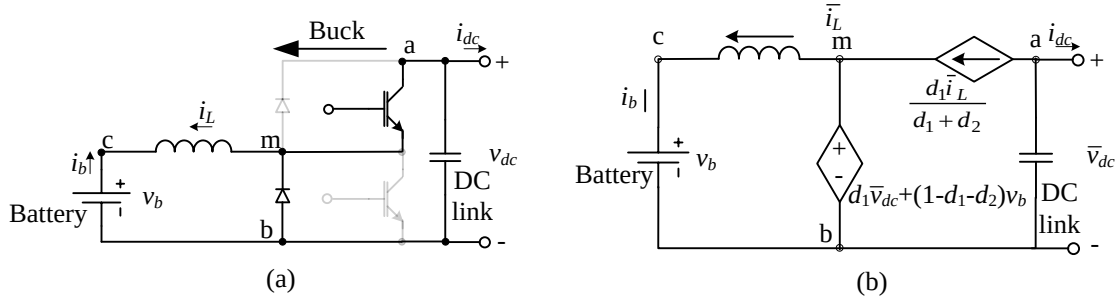


**Fig. 5.8 The dc-dc converter in buck mode, (a) Detailed model, (b) Averaged switch model.**

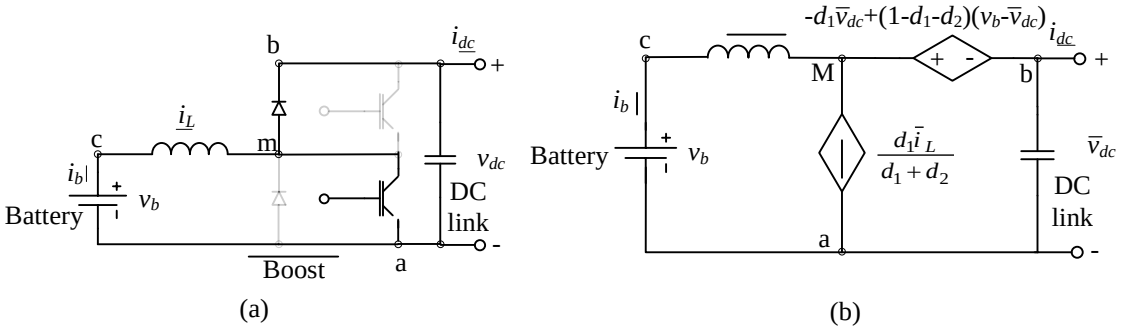


**Fig. 5.9 The dc-dc converter in boost mode, (a) Detailed model, (b) Averaged switch model.**

The combined model for dc-dc converter is shown in **Fig. 5.10**. In this figure, solution of the circuit will include nodes labeled with lower case letters in the buck mode (refer to Fig. 5.8) and nodes labels with upper case letters in the boost mode of operation (refer to Fig. 5.9).

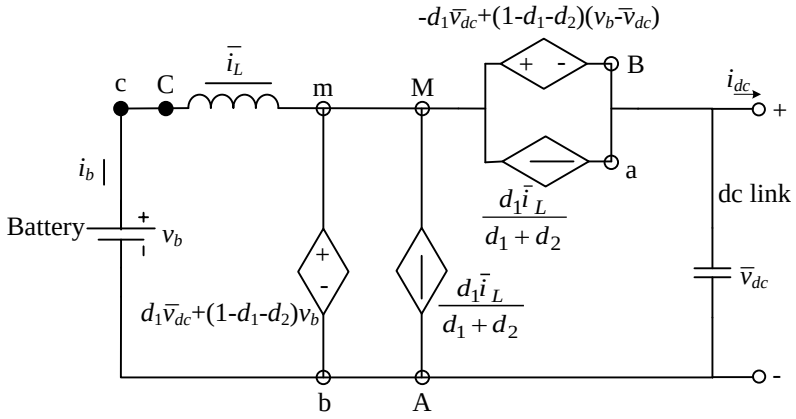


**Fig. 5.10. Averaged switch model for combined bidirectional dc-dc converter.**

### 5.2.2 Model Verification

In this section, the dynamic response of the bi-directional dc-dc converter and its average model are demonstrated in both boost and buck modes of operation. The controller for this converter is the same as the dc-link controller described in Chapter 4 (shown in Fig. 4.17). The converter parameters are summarized in **Table 5-2**.

**Table 5-2 Parameters of dc-dc converter model verification test.**

| Parameter | Value | Description |
|---|---|---|
| $L$ | 0.5 H | Smoothing inductor |
| $C$ | 1 F | Ultra capacitor |
| $V_{\text{battery}}$ | 200 V | Battery voltage |
| $V_{\text{dc}}$ | 650 V | DC link voltage |
| $f$ | 10 kHz | Switching frequency |

The converter connects a 200V battery pack to a dc link with a nominal voltage of 650-V. The load connected to the dc link demands a dc current denoted by $i_{dc}$ in **Fig. 5.10**. The simulated test consists of converter start-up followed by two step changes in the load current as shown in **Fig. 5.11**. During the start-up period of [0,10] s, the converter operates in the boost mode and charges up the dc link capacitor to its nominal voltage, but delivers no current to the load. In the interval [10,20] s, the converter maintains its dc link voltage of 650-V and delivers 50-A to the load (boost mode). In the next interval of [20,25] s, the converter operates as a sink to absorb the power delivered to it while maintain its dc voltage and therefore operates in the buck mode of operation. For the remaining 5 s, the converter ceases to supply or absorb power to its load.

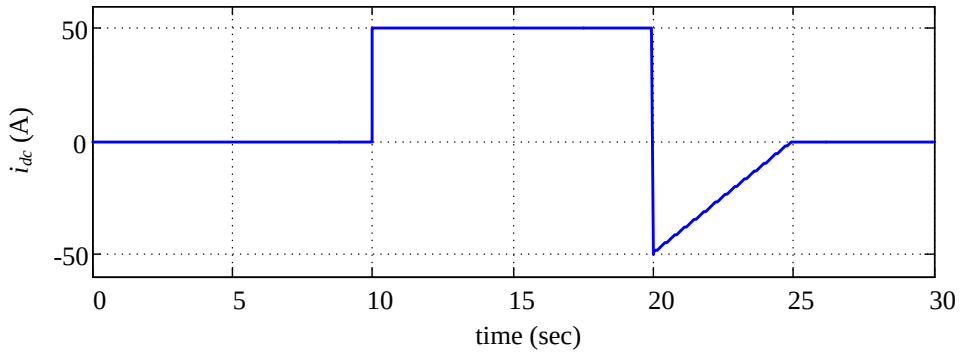


**Fig. 5.11. DC current applied to the converter.**

The response of the converter is shown in **Fig. 5.12**, where traces obtained from the detailed and the average models are shown to essentially overlap. Magnified views of the traces are shown in **Fig. 5.13**. As shown, the average model follows the response of the detailed model. There is a small difference (see Fig. 5.13 (a)) between the actual average of the detailed model's response and the one predicted by the average model. It is due to the resistance of the switch model used in the detailed model. This resistance is neglected in the average model developed here but cannot be entirely eliminated in the detailed model for numerical stability reasons. Despite this difference, the error introduced in the predicted average capacitor voltage due to neglecting the switch losses is negligibly small (less than 0.04%). Energy conservation principle can be used to incorporate conduction and parasitic losses in circuit averaging [87], [98], [99].

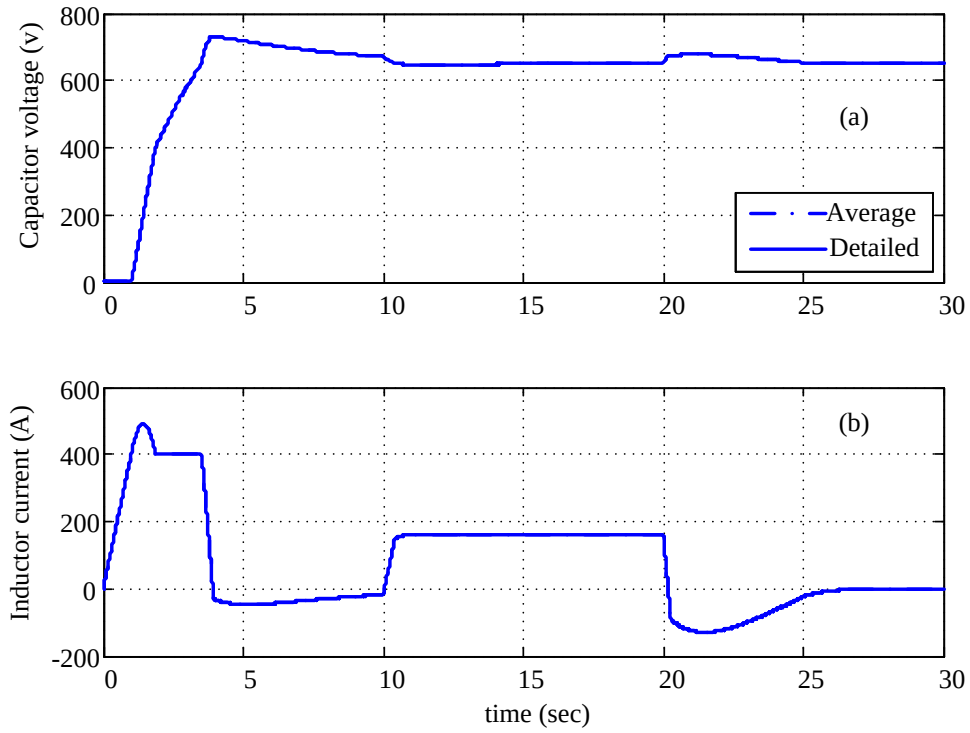


**Fig. 5.12. Converter response, (a) capacitor voltage, (b) inductor current.**

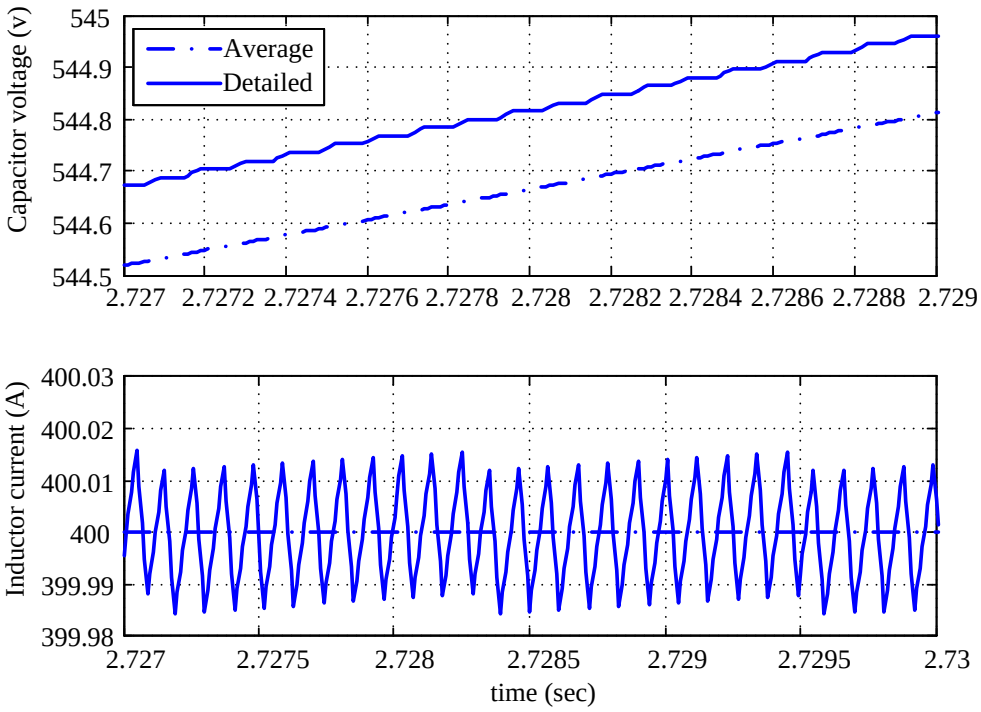


**Fig. 5.13. Magnified converter response, (a) Capacitor voltage, (b) Inductor current.**

## 5.3 Combined Model of the Electrical Subsystem

The average model for the entire electrical sub-system is shown in **Fig. 5.14**. This model includes the battery, dc-dc converter and two sets of VSC controlled permanent magnet synchronous machines. The dc-dc converter model is identical to the model shown in **Fig. 5.10** and it uses the controller shown in **Fig. 4.17**. The VSC dynamic average model is shown in **Fig. 5.2**. The VCS controller provides duty-cycle and converter angle for the VSC model. The output of average model is connected to the electric machine, which provides the torque required by the vehicle controller. The rotor speeds for MG1 and MG2 are fed back to the vehicle controller. The other output of VSC model is the dc current, which is applied to the dc link of the system using a controllable current source.

Using this model, the behavior of the electrical system in the vehicle can be studied without having to recourse to massive computational effort to simulate fast switching of the power electronic converters.

## 5.4 Simulation Results and Discussions

In this section, simulation results for the detailed and dynamic average models of the power-split gear drive-train for a short driving cycle are presented. The driving cycle contains low speed (30 km/h), moderate speed (50 km/h) and high speed (80 km/h) ranges in a driving period of 45 seconds. To verify the accuracy of simulations, different drive-train variables are compared between the two models. These variables include the vehicle speed, the dc currents of MG1 and MG2, the dc link voltage and the battery current. Comparisons include both the accuracy of results and the computer time required to complete the simulations.

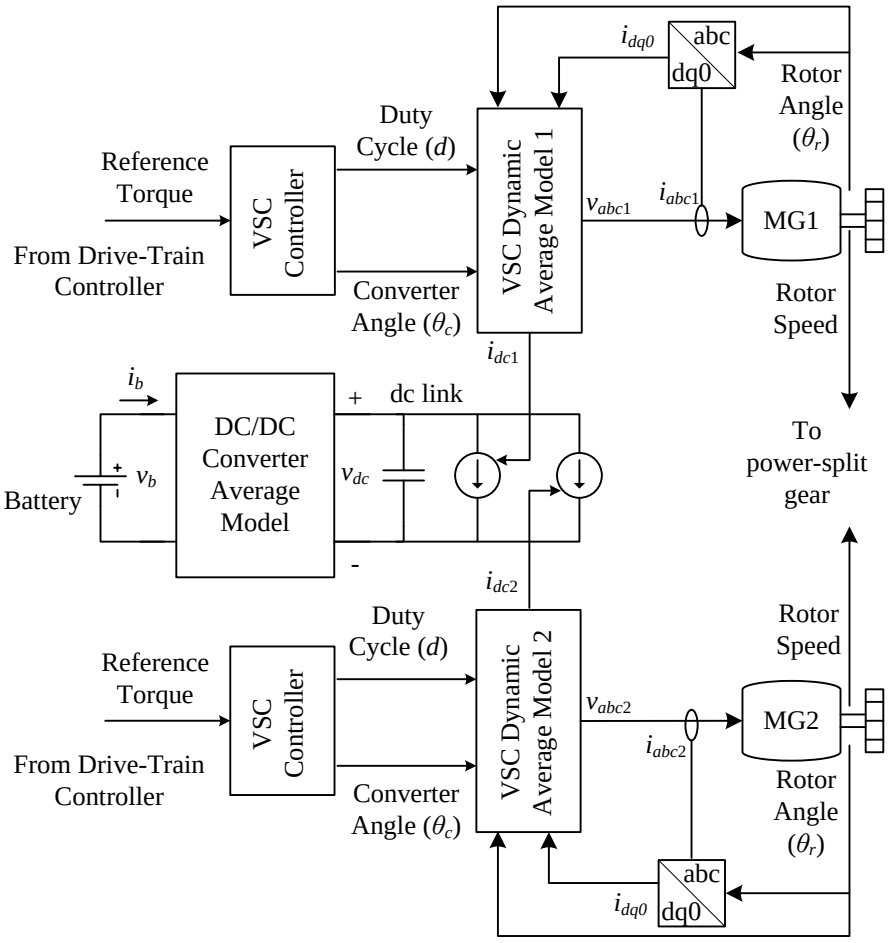


**Fig. 5.14. Combined dynamic average model of the electrical subsystem.**

## 5.4.1 Conformity of Waveforms

The detailed model of the drive-train (refer to Chapter 4) is simulated using a time-step of 10 µs. This small time-step is necessary in order to correctly model the fast switching behavior of the power-electronic converters. The developed average model is simulated using two time-steps of 100-µs and 1-ms to assess both its accuracy in estimating the low-frequency dynamic behavior of the system and its computational intensity. Simulation results of the detailed model and the average model using different time-steps are compared in **Fig. 5.15** to **Fig. 5.19**. Each figure includes three graphs: (a) for simulation

results of the detailed model, (b) for the results of dynamic average model using a 100-μs time-step, and (c) for the dynamic average model results using a 1-ms time-step.

Simulation results for the vehicle speed are shown in **Fig. 5.15**. As shown, results are virtually identical for the three simulations. Therefore, the averaging technique does not cause any appreciable loss of accuracy in predicting the vehicle speed. Note that in many studies the vehicle speed is the primary objective, in which case the average model will give significant time savings as will be shown later.

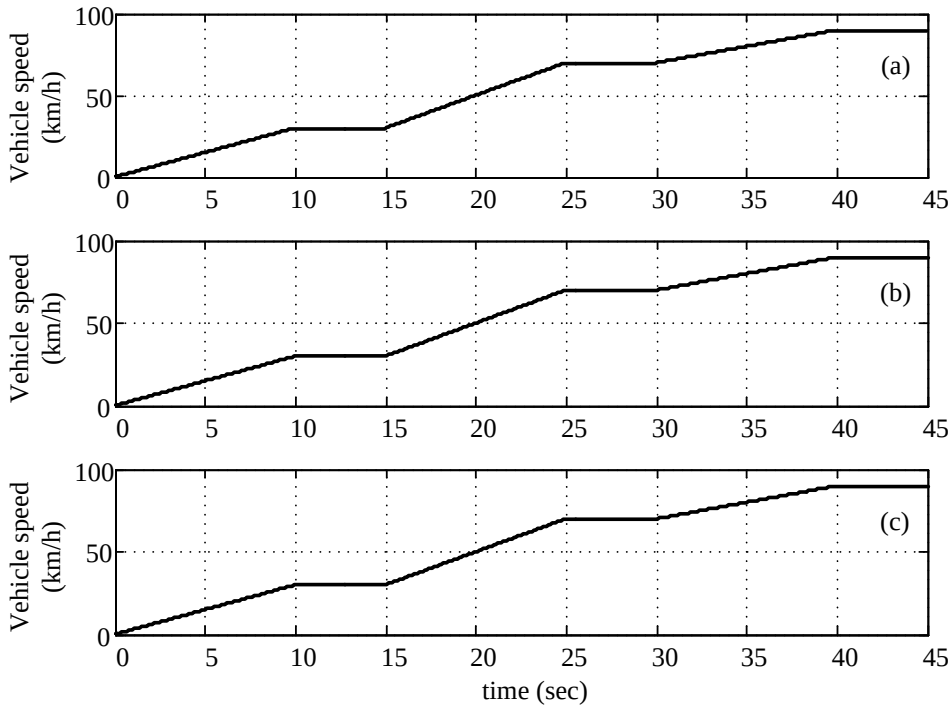


**Fig. 5.15 Simulation results: vehicle speed, (a) detailed model;**

**(b) average model, time-step = 100μs; (c) average model, time-step = 1ms.**

The MG1 and MG2 dc currents (i.e. dc-link side) are shown in **Fig. 5.16** and **Fig. 5.17**, respectively. For these variables, the average model follows the general trend of the detailed model but does not show the high frequency details, as expected. Moreover note that the simulation results of the average model with 100-μs and 1-ms time steps are

essentially identical; however simulation with the longer time step takes significantly less time than the one with a smaller time step, as evidenced in **Table 5-3**. In these figures, the average of detailed model simulation is calculated by dividing the waveform into one hundred sample blocks and averaging every block.

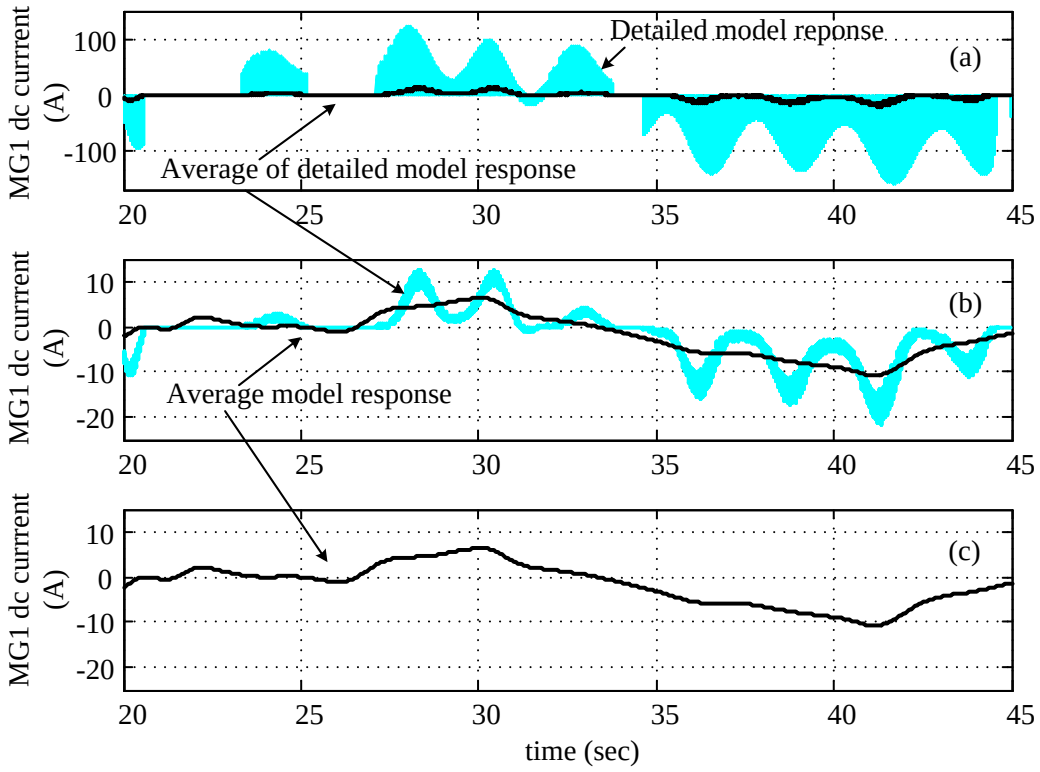


**Fig. 5.16 Simulation results: MG2 dc current, (a) detailed model;**

**(b) average model, time-step = 100μs; (c) average model, time-step = 1ms.**

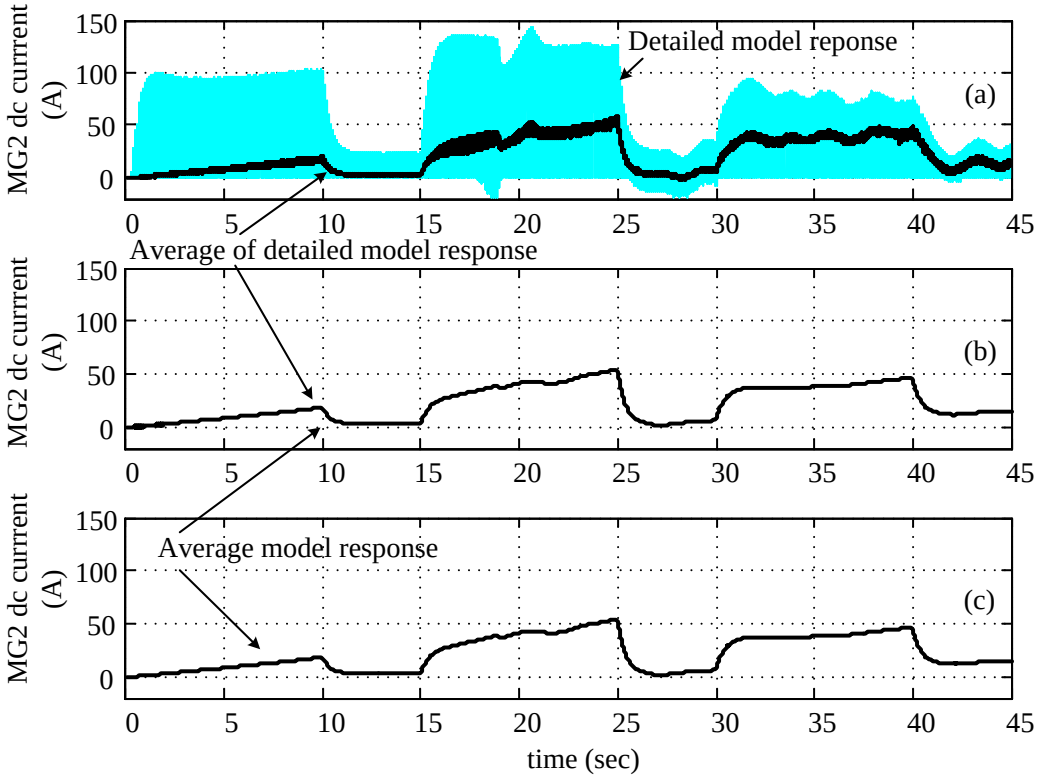


**Fig. 5.17 Simulation results: MG2 dc current, (a) detailed model;**

**(b) average model, time-step = 100μs; (c) average model, time-step = 1ms.**

The dc link voltage is shown in **Fig. 5.18**. Again, the detailed model and average model give results with great agreement. Since the dc link is supported by a large capacitor, high frequency components are not significant even in the detailed model. The battery current is shown in **Fig. 5.19**. For this variable the detailed model and average model with a 100-μs time step produce essentially identical results. Since the battery current flows through a large inductor, high frequency components do not appear to be significant even in the detailed model. High frequency ripple is observed in the simulation results of the average model with a 1-ms step size. This appears as a result of the oscillations of the control system due to the large simulation step size (refer to 5.4.3).

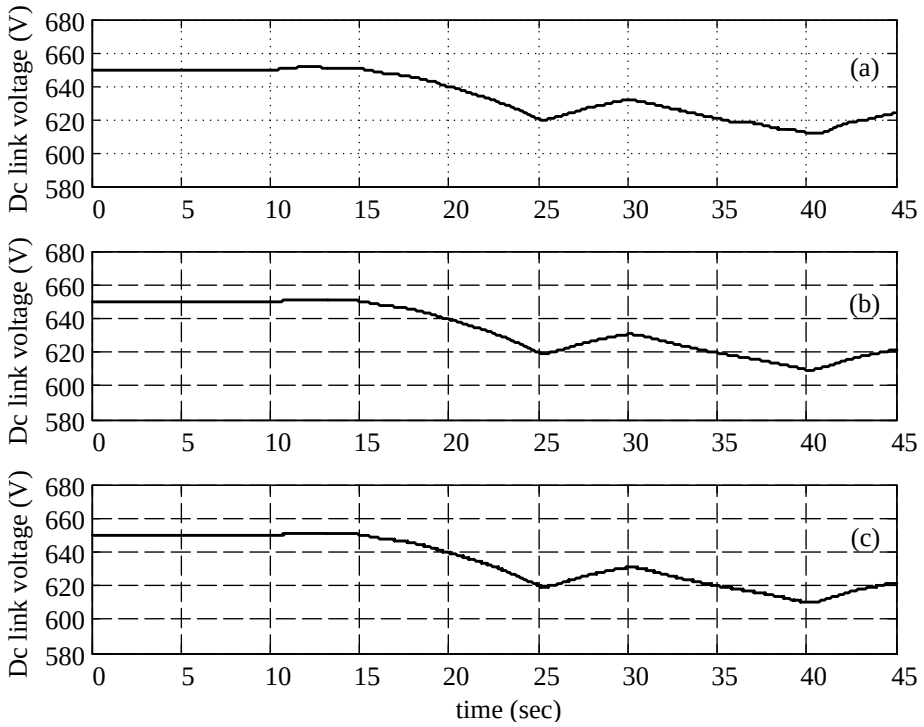


**Fig. 5.18 Simulation results: dc link voltage, (a) detailed model;**

**(b) average model, time-step = 100μs; (c) average model, time-step = 1ms.**

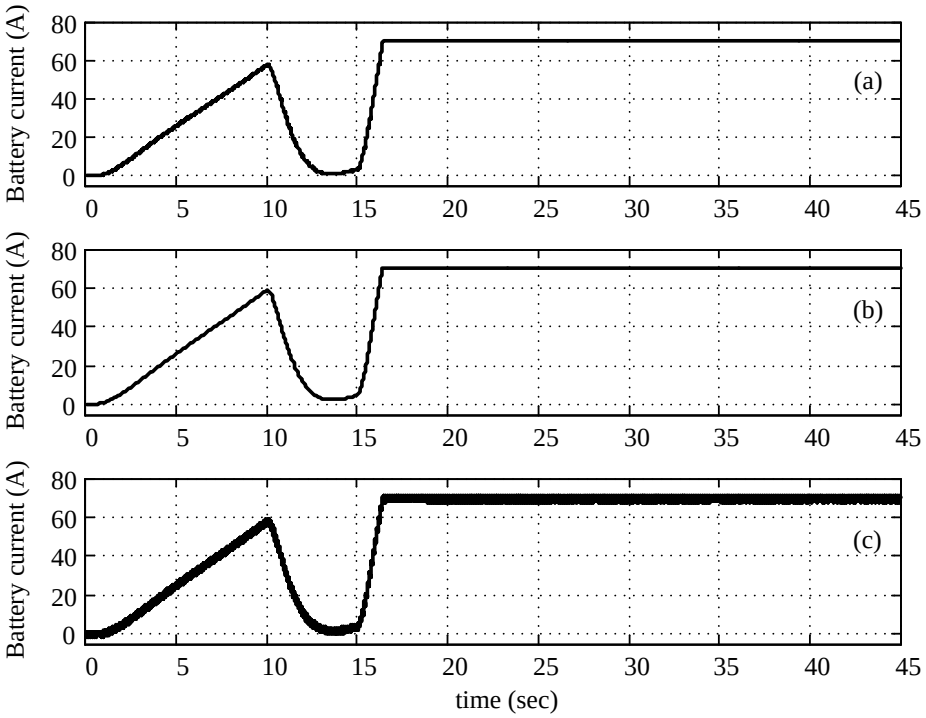


**Fig. 5.19 Simulation results, Battery current, (a) detailed model;**

**(b) average model, time-step = 100μs; (c) average model, time-step = 1ms.**

### 5.4.2 Simulation Time

Simulations are carried out using Matlab/Simulink run on a personal computer with a Intel Core2 Duo processor (2.40 GHz) with 2 GB of RAM. To achieve numerical stability and accuracy, ODE4 (Runge-Kutta) with fixed step-size is used for all simulations. The time to complete a simulation is an indication of the complexity of the model used. To compare the intensity of the detailed and average models developed, they are simulated using a 10-μs time-step initially. As shown in **Table 5-3**, simulation of the original detailed model takes 539 seconds for the 45-s driving cycle, while it takes 479 seconds for the simulation of the average model, which shows a modest gain in the simulation speed. Note that even with a small simulation time-step, the average model does not yield the high-frequency components of the response, as they are ignored in the process of averaging.

The real benefit of dynamic average models is when the variables of interest do not contain appreciable high-frequency components or when such components can be neglected for the purpose of the study at hand. This allows use of a larger step-size, which will in turn reduce the time to complete a simulation.

The largest time-step for use in the simulation of the detailed model is mainly determined by the switching frequency of the power-electronic converters. The switching frequency of the converters used in the detailed model is 10 kHz (i.e. period = 100 μs). A reasonably accurate simulation needs more than ten samples in every switching period. Therefore the maximum time-step for the detailed model is 10 μs to preserve its accuracy. Since the average model does not include the fast switching components, the time-step can be increased to expedite its simulation. Comparative assessment of the

simulation time for the models is shown in **Table 5-3**. As shown the average model offers significant savings in simulation time without appreciable loss of accuracy. Note that reducing the simulation time is especially important for simulations with a repetitive nature such as parameter optimization. Such applications need to run the simulation numerous times to reach to the objectives of the simulation [100], [101]. In addition, a fast simulation is also very useful in the design stage, when the designer changes different parameters many times and runs the simulation to observe the effect of the change.

In addition to general benefits of having a fast model, in this particular study using such model is necessary since the detailed model cannot be implemented on the real-time simulator with the available installed hardware.

**Table 5-3 Simulation time**

| Model type | Step size | Simulation time (sec) |
|---|---|---|
| Detailed | 10 µs | 538.45 |
| Averaged | 10 µs | 478.95 |
| Averaged | 100 µs | 40.372 |
| Averaged | 1ms | 4.0450 |

Simulation time window = 45 s for all simulation.

### 5.4.3 Control System Oscillation

In digital simulation, the simulation time-step should be selected according to the Nyquist rate, which is two times of the bandwidth of the system. It is often recommended to have smaller time-steps. Five to ten samples in the fastest transient of the system is a common practice for selecting the time-step. In the developed average model for the drive-train, increasing the time-step may results in oscillations in the results such as the ones in **Fig. 5.19**. These oscillations are not due to inaccuracy of the average model, but because of control system oscillation. This is shown better in **Fig. 5.20**. This figure shows the duty

cycle and the inductor current in the bidirectional dc/dc converter for two time-steps, i.e. 1ms and 100 µs. As shown, simulation results with 1ms time-step contain oscillations in duty cycle and as a result in inductor current. The same simulation with 100µs time-step results in smooth waveforms for both duty cycle and inductor current.

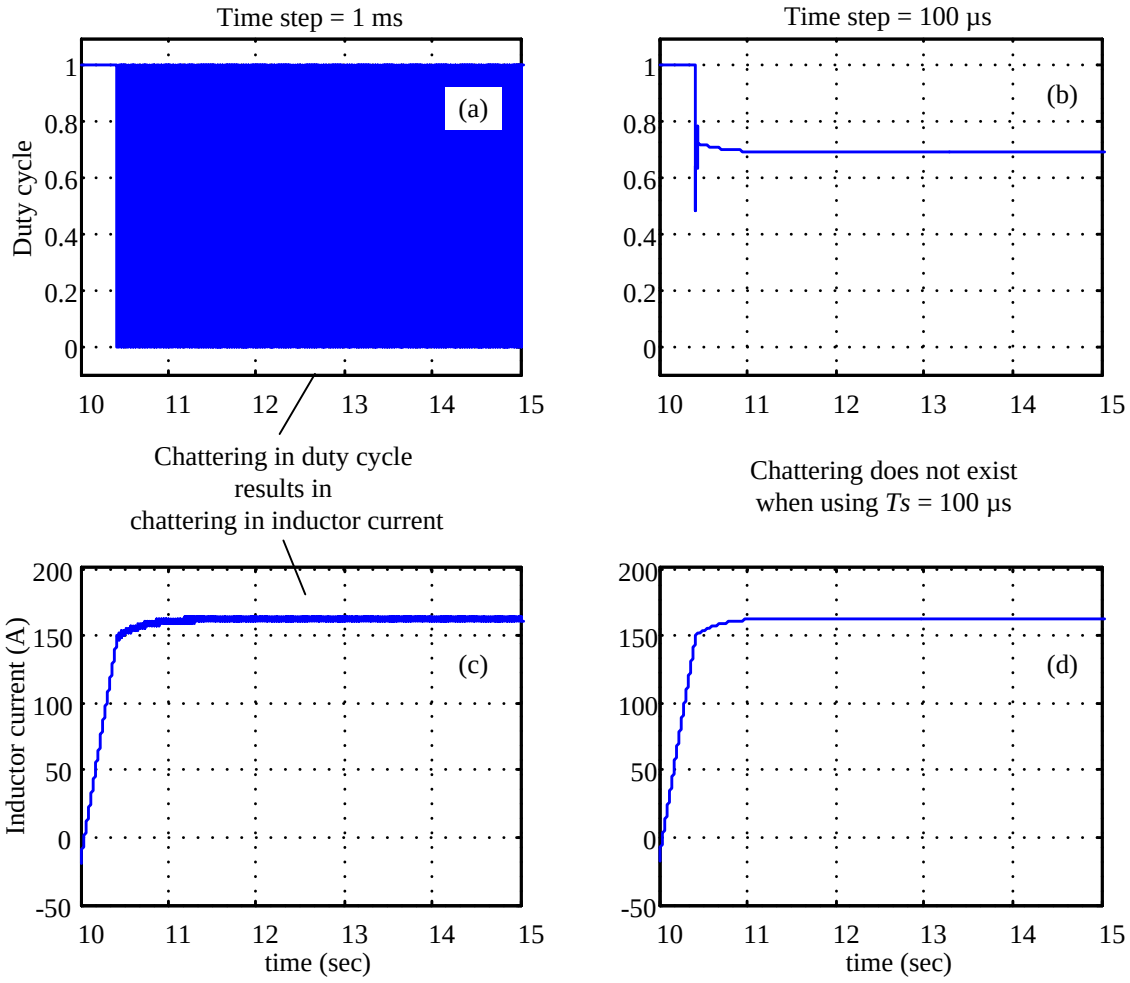


**Fig. 5.20 Control system oscillation demonstration, (a) Duty cycle, Ts = 1ms, (b) Duty cycle, Ts = 100µs, (c) Inductor current, Ts = 1 ms, (d) Inductor current, Ts = 100µs.**

**Fig. 5.21** shows a magnified version of the simulation results. As this figure shows, the sampling rate in simulation with 1ms time-step is not enough for the duty cycle to settle in a steady-state condition. The duty cycle keeps changing between 0 and 1. Using 100 µs

time-step, the sampling rate is ten times larger and this makes the duty cycle to stabilize in steady state condition without oscillating.

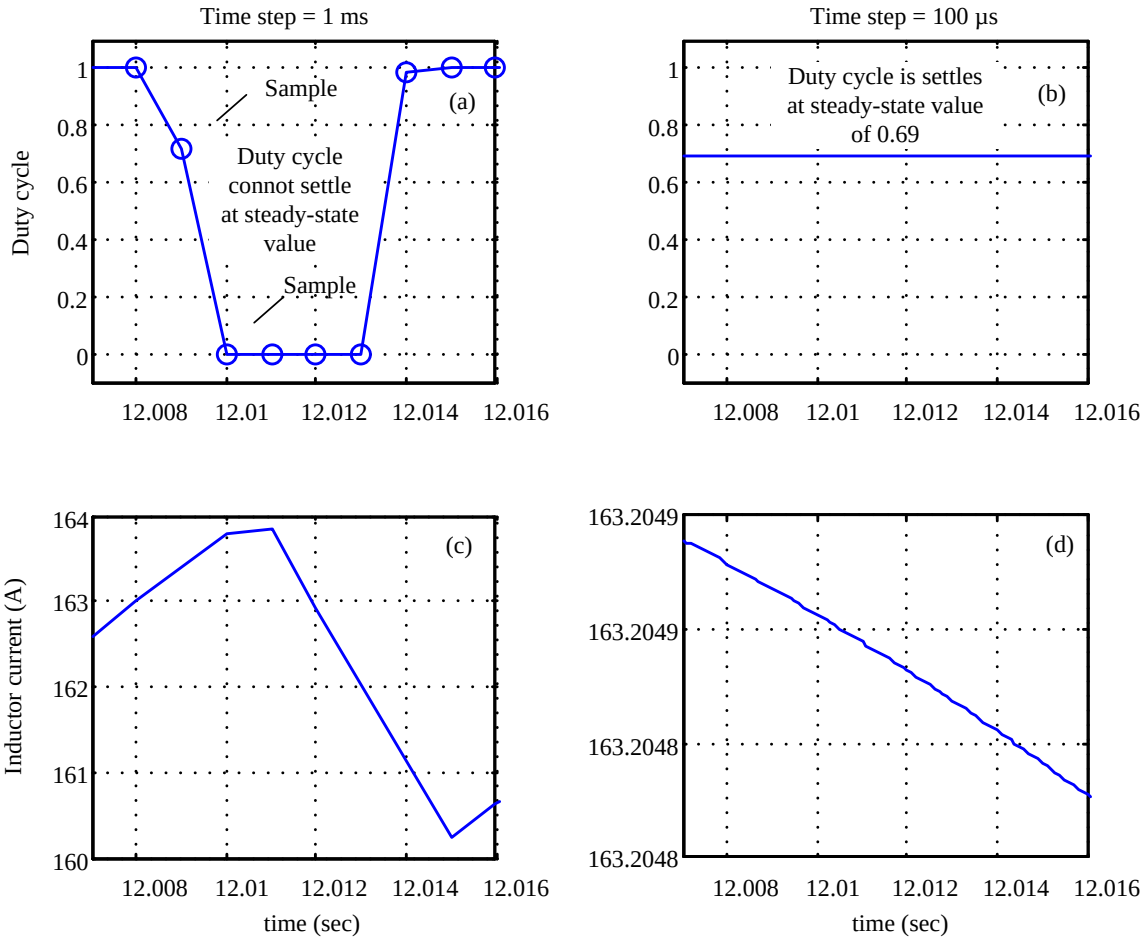


**Fig. 5.21 Control system oscillation demonstration, magnified view, (a) Duty cycle, Ts = 1ms, (b) Duty cycle, Ts = 100µs, (c) Inductor current, Ts = 1 ms, (d) Inductor current, Ts = 100µs.**

## 5.5 Chapter Summary and Contributions

In this chapter the concept of averaged-value modeling is applied to a vehicle model for the first time. The averaging technique is used to make a reduced intensity model that can be implemented on the available real-time simulator. This chapter shows how different

techniques for modeling dc/dc converters and voltage source converters are used to develop the required drive-train model. Simulation results show that using this model, a reasonable response of the drive-train can be simulated in a very short time compared to the detailed model.

The purpose of developing this model is to use it in a real-time simulator to create a hardware-in-loop setup. Although the developed model ignores the switching transients in the power electronic converters, simulation results show that it has great accuracy for the battery current, which is the variable of interest in simulation. Battery current does not include high frequency switching transients since it is flowing through the dc-dc converter inductance. Therefore, this variable does not suffer from inaccuracy introduced by ignoring the switching transients. The hardware-in-loop setup developed based in this model is explained in the next Chapter.

# Chapter 6

# Real-Time, Hardware-in-Loop Simulation

Real-time simulation is a useful approach for study of complex systems. This type of simulation has two benefits. The first benefit is the high speed of real-time simulators. Simulations that can take a long time using a computer can be done in real-time using high speed real-time simulators [76]. The other benefit of real-time simulation is when it is bundled with external equipment to form hardware-in-loop simulation (HIL). Using HIL one can test the performance of a particular actual hardware in a system while the rest of the system is modeled in the simulator. Using HIL method, the actual hardware can be tested under different operating conditions. It might be difficult, time consuming, expensive or impractical to make the same conditions in the actual system. Various applications are proposed for HIL simulation. For example, relay testing is a popular application of HIL [102]. In this application, the relay performance for different fault scenarios can be tested. Such tests are not possible when the relay is connected to the power system. HIL is also widely used in drive-train studies. For example, in [103], a HIL setup is developed to design an automatic steering control, in [104], a HIL setup is used to simulate climate control of a vehicle and [105] uses HIL to design a stability controller for a small vehicle.

In this study, a HIL setup is developed for a hybrid-electric vehicle drive-train. In this setup, the drive-train (including electric machines, power electronic converters, internal

combustion engine and different controllers) is modeled in the simulator and actual batteries are used in the simulation loop. The drive-train is simulated using RT-Lab/Opal-RT real-time simulator [106]. This simulator simulates the model developed in MATLAB-Simulink and also provides analog and digital inputs and outputs, which facilitate hardware-in-loop simulations.

In order to develop a HIL setup, a model of the system should be developed first. In this study, two models are developed: transient model in Chapter 4 and dynamic average model in Chapter 5. The transient model contains detailed power electronic models and thus requires a small time-step for simulation. Experiments using the available Opal-RT simulator showed that the simulator is not capable of running the simulation in real-time with currently installed software and hardware. Therefore, a less mathematically involved model is required for the HIL system. As shown in Chapter 5, the developed dynamic average model is significantly faster than the transient model and at the same time it is accurate enough for a wide range of drive-train studies. The dynamic average model is transferred to the real-time simulator and the simulator is able to run the model in real-time. This real-time simulation is the core of the HIL setup. The HIL setup uses actual batteries and it is a useful platform to test both existing and emerging battery technologies in hybrid-electric drive-train applications. Using this setup, batteries can be tested under different vehicle controller strategies, driving conditions and climate conditions[1]. This setup is explained in the following section.

[1] Different climatic conditions can be tested by installing the batteries in environmental chambers.

## 6.1 Hardware-in-Loop Setup

Block diagram of the HIL system developed in this study is shown in **Fig. 6.1**. The HIL system is based on the dynamic average model developed in Chapter 5. It includes high level controllers (driver model, vehicle controller and PSG controller) and low level controllers (VSC controller). The average-value models of the power electronic converters are interfaced with two electric machines, MG1 and MG2. A power-split gear model interfaces the electric machines and ICE model. The average-value model of the dc-dc converter is placed between the dc-link and a voltage source representing the battery. The model is then interfaced with actual Li-ion batteries using I/O ports available on the real-time simulator, a power amplifier and an HIL controller block in the simulation. The real-time simulator communicates with the command station via an Ethernet protocol. User can change the simulation parameters, such as driving cycle and road condition, and watch the simulation results in real-time using the command station. Simulation result can be stored in the real-time simulator and be transferred to the command station for further studies and for future use. The real-time simulator used in this study is the Opal-RT with two active cores. Matlab/Simulink and Power SystemBlockset are used to develop the model.

**Fig. 6.2** shows a schematic diagram of the hardware used in developing the HIL setup. The real-time simulator's analog I/Os are used to establish the HIL setup. Two analog inputs and two analog outputs are used for this purpose. A current transducer and a voltage sensor are used to measure the battery voltage and current and send it back to the real-time simulator using the analog input ports.

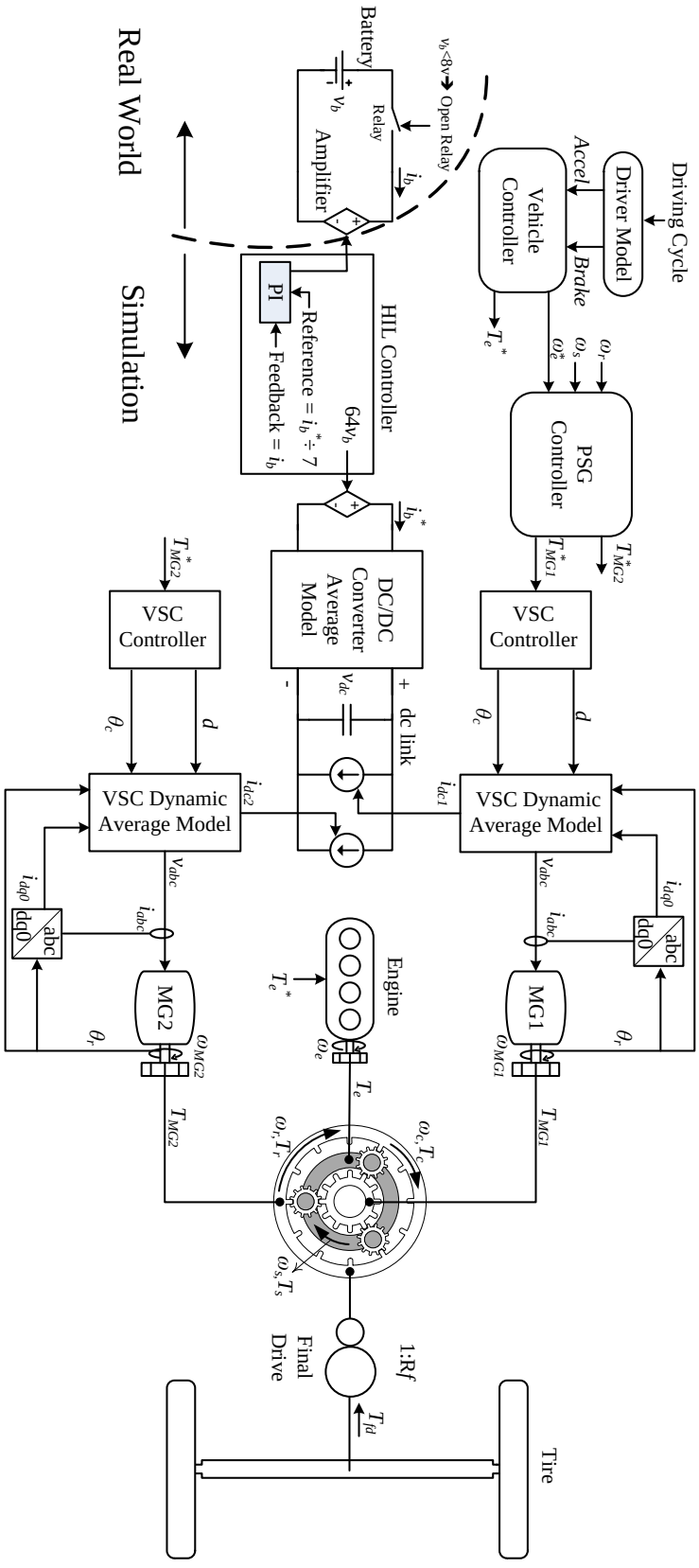


**Fig. 6.1 Block diagram of dynamic average model based HIL system**

The actual battery is connected to a four-quadrant amplifier that works in voltage control mode. Based on the results of simulation in real-time, simulator will generate a signal to indicate how much current the battery must supply or absorb. The amplifier is then controlled through a closed-loop proportional-integral (PI) controller, which manipulates the amplifier's output voltage, such that the battery current meets the specified reference current. This is done in a block called HIL controller (explained in 6.2.1). Note that due to safety reasons, the amplifier cannot be used in current control mode. While working in current control mode, the amplifier may apply large values of voltage to pump current into the connected circuit. The battery technology used in this setup is extremely sensitive to over-voltage and may gas or even explode if it is exposed to high levels of voltage. Therefore, to keep the system safe, a current control algorithm with limited voltage is implemented in the simulator and the amplifier is used in the voltage control mode.

The battery pack used comprises cells of Li-ion battery with the specifications listed in **Table 6-2** and

**Table 6-3**. In the HIL simulation of the vehicle, a total battery capacity of 205 V and 18.2 Ah (for 3.7 kWh) is assumed. Connection of such a battery pack in its entirety poses significant challenges in particular with regard to the cost of the amplifier. Alternatively a smaller battery pack can be assembled using cells identical to the ones used in the 3.7 kWh pack. A pack of batteries with a voltage of 12.8 V and capacity of 2.6 Ah is assembled for this purpose and is interfaced with the real-time simulator as a scaled-down version of the larger battery pack. The measurements taken from this smaller pack will be scaled up before transmission to the real-time simulation model so that it represents the intended larger pack. This is done by multiplying its voltage by 16

(16×12.8 V = 204.5 V) and its current by 7 (7×2.6 Ah = 18.2 Ah). This method of using scaled down battery packs is also used in other studies [54] and is widely accepted as adequately accurate.

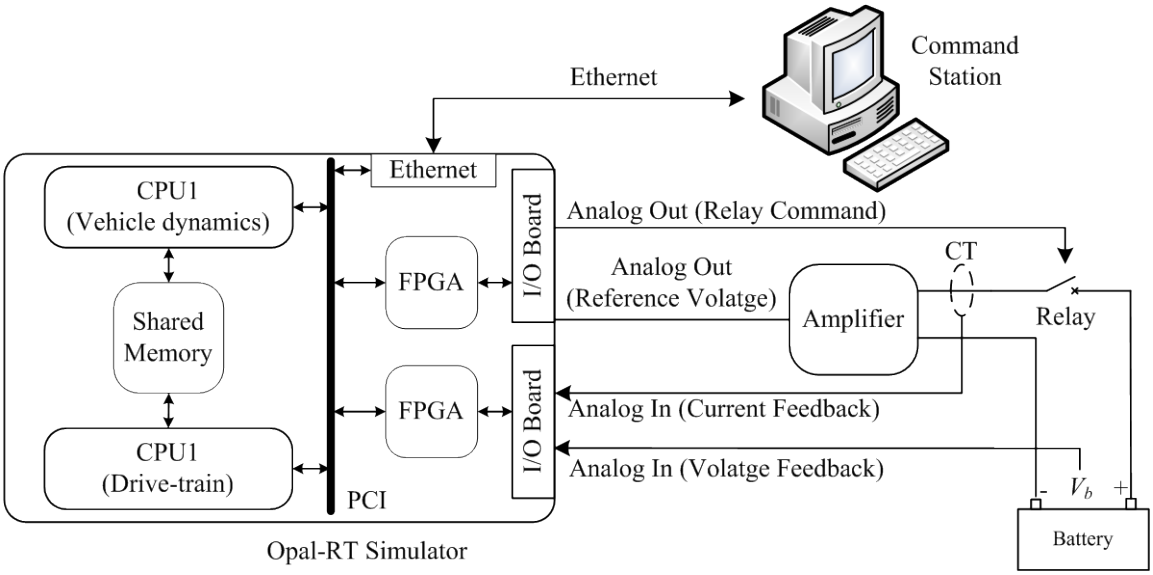


**Fig. 6.2 Hardware-in-loop setup**

### 6.1.1 Opal-RT Simulator

RT-Lab/Opal-RT real-time simulator is used in the developed HIL setup to simulate the dynamic average model of the drive-train, developed in MATLAB/Simulink. **Fig. 6.2** shows the hardware configuration of this simulator. Opal-RT simulator uses two processor cores; each can run a Simulink model separately. Processor cores exchange data using a shared memory. An FPGA board is used to control the I/O ports and also generating the synchronizing clock pulse. The FPGA and CPUs are connected together using a PCI interface. The simulator communicates with the command station using an Ethernet network.

### 6.1.2 Amplifier

The amplifier used in the HIL setup is an AE Techron 7224 amplifier. This amplifier, shown in **Fig. 6.3**, is a four quadrant amplifier that can source and sink power to and from the battery. The amplifier inputs are determined by the simulator and sent via a coaxial cable. This amplifier can work either in current or voltage control mode. In this setup it is configured to operate in voltage control mode.


**Fig. 6.3 AE Techron amplifier**

In this setup the battery current does not have fast transient due to the large smoothing inductor in the dc/dc converter on the battery side (refer to Chapter 5). On the other hand the converter will be providing a dc current for long periods (e.g. an hour) when charging/discharging the battery. Therefore, among the specifications of the converter, the dc specifications are the most important ones for this study. The dc characteristics of the converter are listed in **Table 6-1**. Another important aspect of the amplifier is the minimum required impedance at the terminals of the amplifier. Since battery internal impedance is only a few mili-ohms, a wrong selection of amplifier may result in oscillatory output voltage that can damage the battery. The amplifier used in this setup will not show oscillatory behaviour even if output terminals are shorted.

**Table 6-1 DC specification of the amplifier**

| Terminal Voltage (V) | 5 min<br>Max. Current (A) | 1 hour<br>Max. Current (A) |
|---|---|---|
| 24.0 | 26 | 20 |
| 13.5 | 20 | 16 |

### 6.1.3 Battery

The battery used in this HIL setup is a high power Li-ion battery, LFP26650P, from K2 Energy [107]. As explained in chapter 3, NiMH and Li-ion battery chemistries are both good candidates for hybrid-electric vehicles. Li-ion battery has larger power and energy density and it also costs more. With the new developments in battery manufacturing methods, the cost of Li-ion battery has dropped significantly. Therefore it is becoming more popular in hybrid-electric vehicles. Therefore, the Li-ion battery technology is selected for the hardware-in-loop setup in this thesis. Specification of the battery cell and recommended operating conditions are listed in Table 6-2 and

**Table 6-3.**

**Table 6-2 Battery cell specifications**

| Parameter | Value |
|---|---|
| Normal capacity @ C/5 (Ah) | 2.6 |
| Average operating voltage @ C/5 (V) | 3.2 |
| Internal impedance @ 1kHz (mΩ) | <9 |
| Weight (g) | 80.5 |

**Table 6-3 Battery cell recommended operating conditions**

| Parameter | Value |
|---|---|
| Continuous discharge (A) | <10 |
| Pulse discharge (A) 30 seconds | 26 |
| Charge current (A) | <2.6 |
| Charge voltage cutoff (V) | 3.65 |
| Discharge voltage cutoff (V) | 2.50 |
| High operating temperature ($^{o}$C) | 60 |
| Low operating temperature ($^{o}$C) | -20 |

Four batter cells are connected in series and form a 12.8-V battery pack. The battery pack includes a cell-balancing circuit in parallel with each cell. **Fig. 6.4** shows the battery pack used in HIL setup.


**Fig. 6.4 LFP26650P battery pack**

### 6.1.4 Current and Voltage Sensors

The HIL setup uses battery current and voltage feedback in the simulation. This is done using a current reading board and a voltage reading board. The current measurement is done using a current transducer (CT). The CT output is then amplified and sent back to the simulator. **Fig. 6.5** shows the current measurement board, including the CT and amplifier, used in this study.

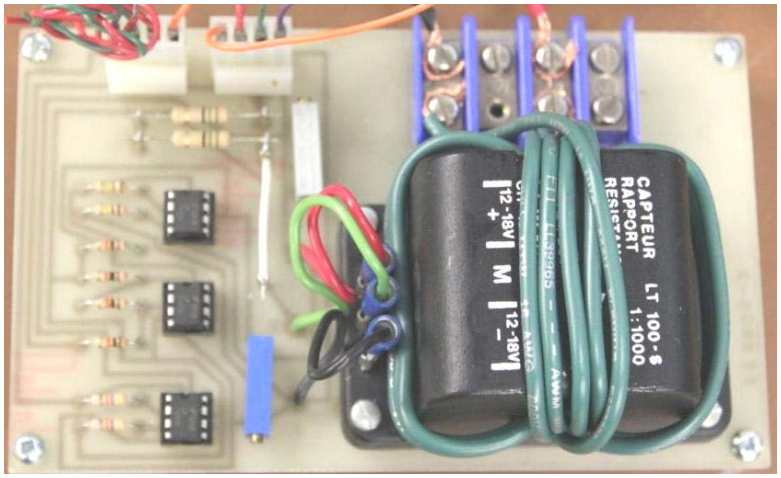


**Fig. 6.5 Current measurement board**

Battery voltage is also necessary for HIL simulation. The terminal voltage is scaled down using a simple resistive voltage divider and then isolated using an isolation amplifier (AD202JN from Analog Devices). The isolated output is then sent to the analog input of the simulator as shown in **Fig. 6.2**. The voltage measurement board is shown in **Fig. 6.6**. This figure also shows the relay that is used to disconnect the battery from the amplifier when it is necessary.

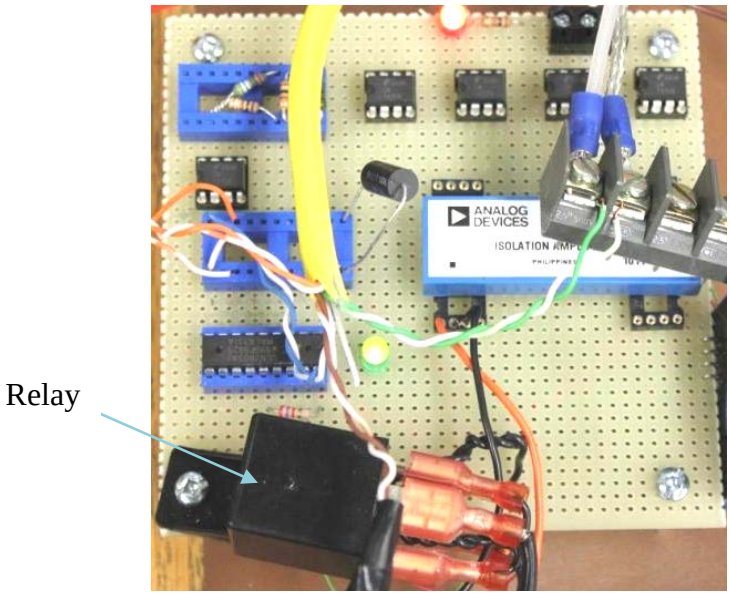


**Fig. 6.6 Voltage measurement board and relay**

## 6.2 Simulation Setup

As shown in **Fig. 6.2**, two CPU cores are available inside the Opal-RT simulator to perform the simulation tasks. In the developed HIL setup, CPU1 is dedicated to simulate the drive-train (shown in **Fig. 6.1**). Models for MG1, MG2, PSG, ICE and tire are identical to the ones described in Chapter 4. Power-electronic converters, i.e. VSC1, VSC2 and dc/dc converter are modeled using the dynamic average modeling technique described in

Chapter 5. HIL controller is the interfacing block between the simulation and actual batteries. This block receives voltage and current feedback signals and send control signal to the power amplifier and the relay. This block is explained in the next sub-section.

CPU2 on the simulator is dedicated to simulate the Vehicle dynamics (shown in **Fig. 4.4**). This block received the force generated in the drive-train, calculates the resistive forces and determines the vehicle speed. This model is identical to the vehicle dynamics block described earlier in Chapter 4.

### 6.2.1 HIL Control Block

The HIL control block is the interfacing block between the actual batteries and the simulated drive-train. The battery under test includes 4 cells of 3.2V with maximum allowable current of 10A (according to the battery recommended operating conditions in **Table 6-3**). It is assumed that the battery in the drive-train is made of 7 parallel branches, each including 64 cells in series (see **Fig. 6.7**). The total battery pack yield 204.8V battery with maximum allowable current of 70A. This allows the vehicle controller to draw 14kW of power from the battery, which is a reasonable value to have all-electric mode for low speed periods (urban driving condition).

The HIL control block translates the real battery voltage and current for the vehicle model and scales these values to the proper values suitable for the drive-train. The measured battery voltage is multiplied by 16 and sent to the drive-train model as the battery voltage, the battery reference current determined by the drive-train model is divided by 7 and used as the reference current in the HIL control block.

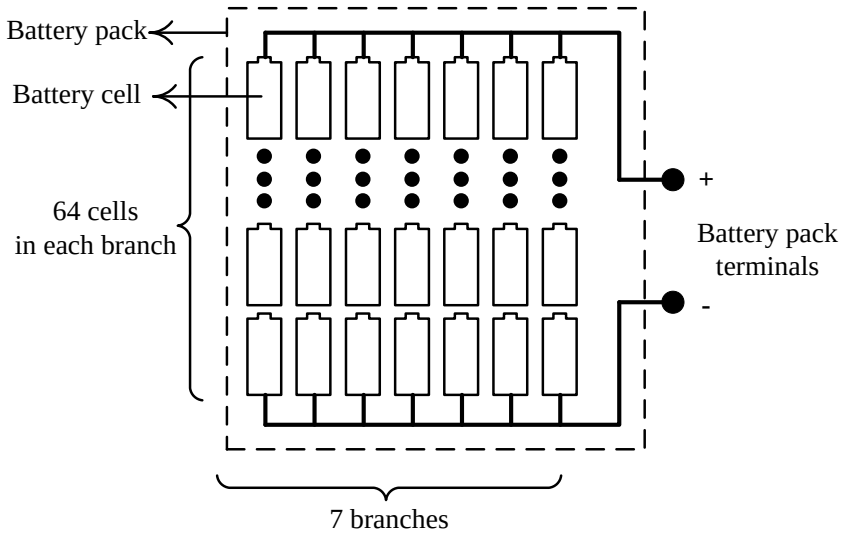


**Fig. 6.7 Battery pack assembly**

The HIL control block also controls the communication of the simulation with the real world. It receives the voltage and current feedback signals from the measurement boards and also sends the command signal to the power amplifier. **Fig. 6.8** shows the controllers used to derive the amplifier and relay command signals based on the feedback received from the measurements boards.

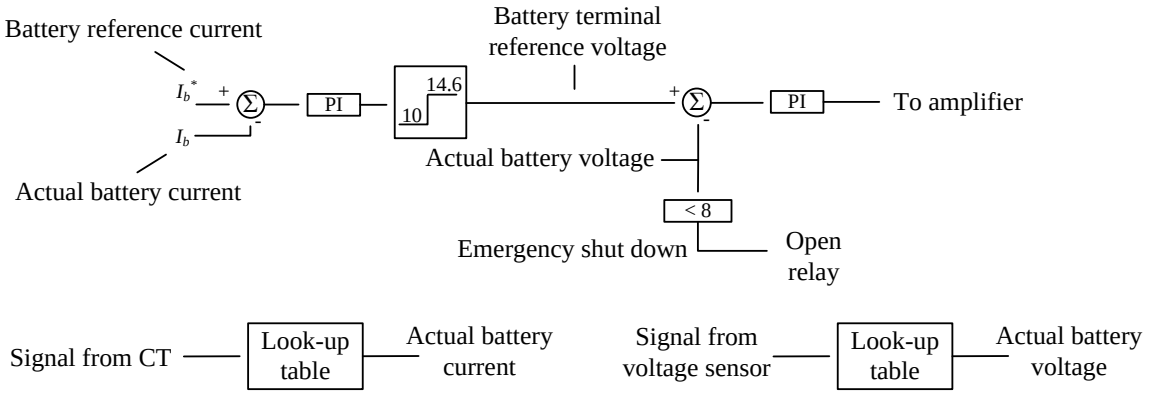


**Fig. 6.8 HIL controller**

An accurate multi-meter is used to form look-up tables to calibrate the readings of current and voltage sensors. The battery reference current is determined by the dc/dc converter and then scaled using the battery block. This reference current is compared

with the battery actual current and the difference is fed to a PI controller in order to obtain the battery terminal reference voltage. The battery reference voltage is compared with the actual battery voltage and the difference is fed to a PI controller to obtain the reference point for the amplifier. Note that due presence of resistances in the loop (amplifier output resistance, battery internal resistance, cable resistance) using two control loops is necessary to control the battery terminal voltage within the desired limits under different currents.

## 6.3 Preliminary Tests on the Battery

The developed HIL simulation requires an estimation of the state of charge (SOC) of the battery in order to ensure that the vehicle controller only operates the battery within the permissible range. In order to devise a reliable SOC estimation method one needs to know the charge and discharge curves of the battery. This section therefore presents the results of the preliminary tests done on the battery to determine its charge and discharge characteristics, estimation of its state-of-charge and also test results of the actual drive-train simulation.

### 6.3.1 Battery Charge/Discharge Curves

There are different charging strategies reported in the literature [60], [108]-[112]. All these methods include constant current and constant voltage regions to charge the battery. **Fig. 6.9** shows a typical charging strategy for Li-ion batteries.

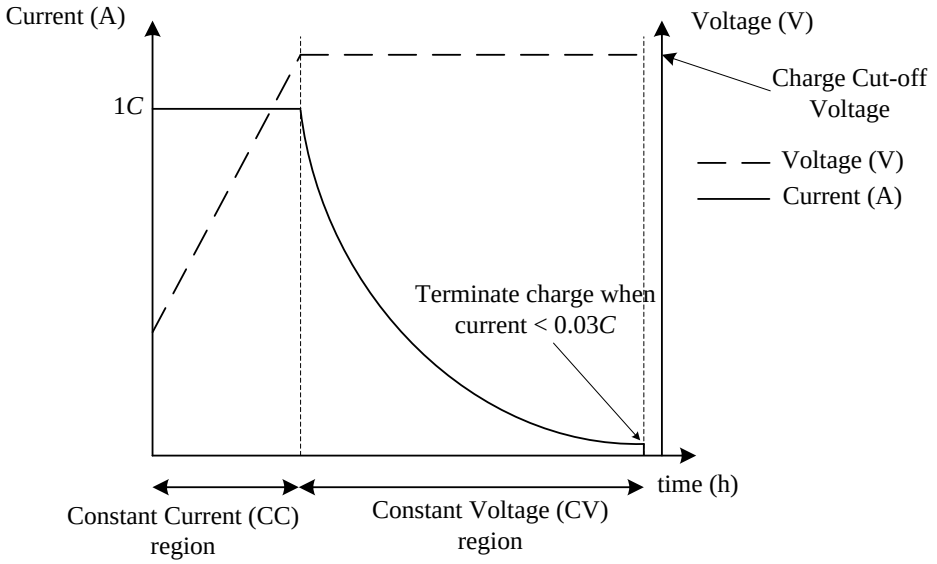


**Fig. 6.9 Typical charging strategy for Li-ion batteries.**

As shown in this figure, charging starts in constant current (CC) mode. In this stage, the battery current is kept constant. The battery voltage rises as the current is pumped into the battery. The current is usually kept below rated capacity of the battery (1*C*), however depending on the battery technology it is possible to increase this current. CC stage is terminated when the battery voltage reaches a certain value, called charge cut-off voltage. This voltage is slightly more than the rated battery voltage. Note that Li-ion batteries are very sensitive to over-voltage exposure. Gassing and explosion can happen if the battery is exposed to higher than permitted voltage. At this point, the battery has absorbed more than 80% of the possible charge. Constant voltage (CV) stage fills the remaining capacity. In CV region the battery voltage is held constant and the current tails off as the battery charges up. Battery charging in constant voltage mode has an exponential nature, therefore, charging current never becomes zero and a full charge can never be achieved. To have a practical system, charging is considered to be done when the battery current becomes smaller than a certain value, typically 3% of the rated current.

For HEV application, charge time is an important factor. A Shorter charging interval means having the battery available for generating power in longer periods and that increases the efficiency of the drive-train. Therefore, for this study the battery is charged in CC region only and the CV mode is not used. The battery state-of charge is at an acceptable value at the end of the CC region. Considering the duration of CV period, the charge that is absorbed in this region is not significant and therefore this region is ignored. In fact for the tested battery, CC mode results in a 90% charge. Considering that the SOC is commonly limited to 80% in the vehicle controller, using the CC mode only is sufficient for this application.

**Fig. 6.10** shows the charging characteristics of the Li-ion battery used in this study. As shown charging is done at a constant current of 1.8 A; the terminal voltage of the battery pack rises nonlinearly. It has steep slopes in the beginning of the charging regime and towards its end. For a relatively wide range in the middle, however, the voltage increases with a small slope. This indicates that the cell voltage is not a completely reliable measure of the battery SOC, due to its negligible change with the SOC. The other outcome of a charge/discharge cycle is to estimate the coulombic efficiency of the battery, defined as the ratio of the charge supplied by the battery during discharge to the charge stored in the battery during charging. Several tests were conducted at charge and discharge currents in the range of 2.5 A to 7.5 A on the Li-ion pack (**Fig. 6.11** to **Fig. 6.13**); the average coulombic efficiency of the pack through these experiments was obtained to be 98%. This value is used in the SOC estimator as outlined below.

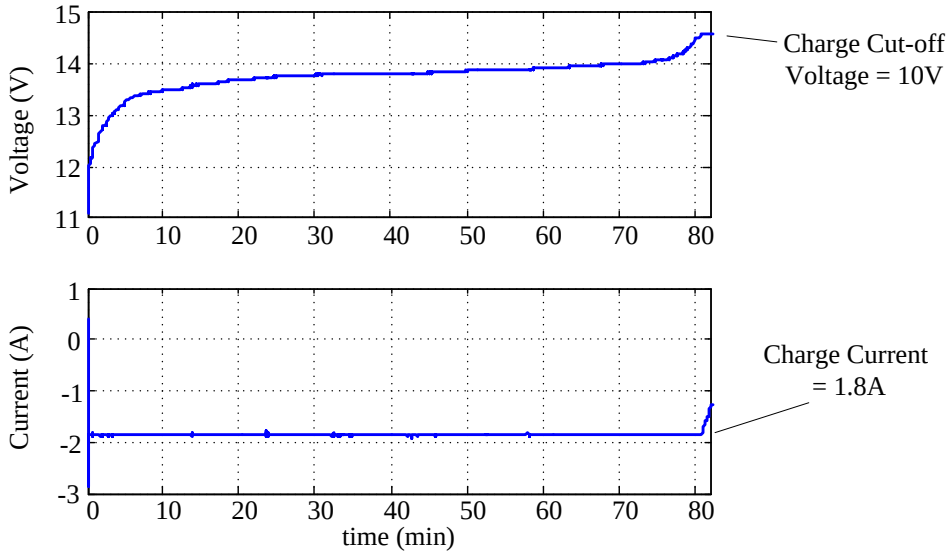


**Fig. 6.10 Battery charging**

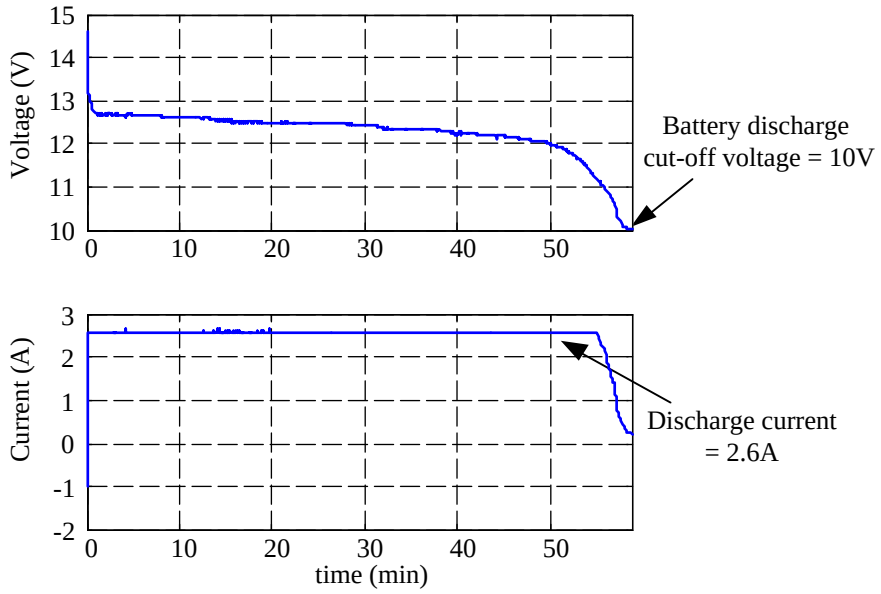


**Fig. 6.11 Battery discharge with 2.6A**

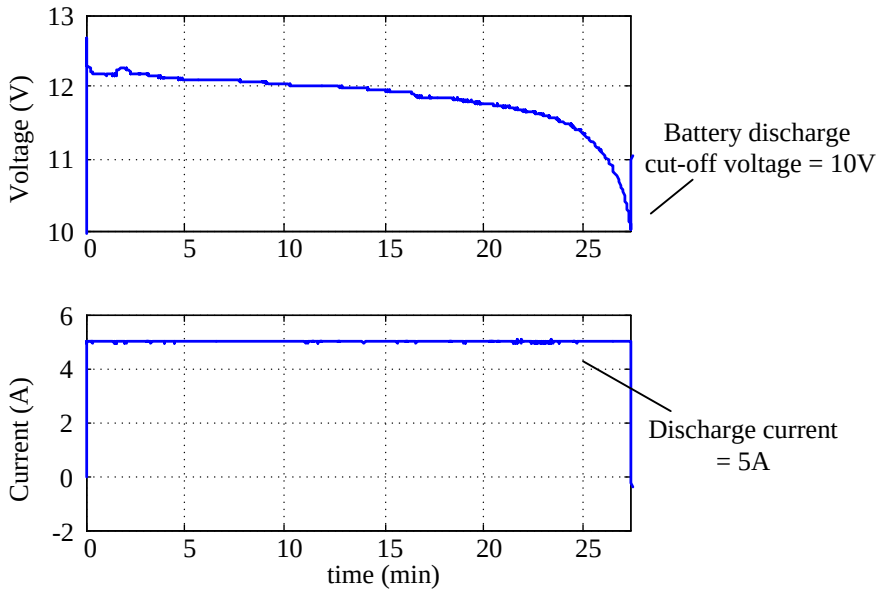


**Fig. 6.12 Battery discharge with 5A**

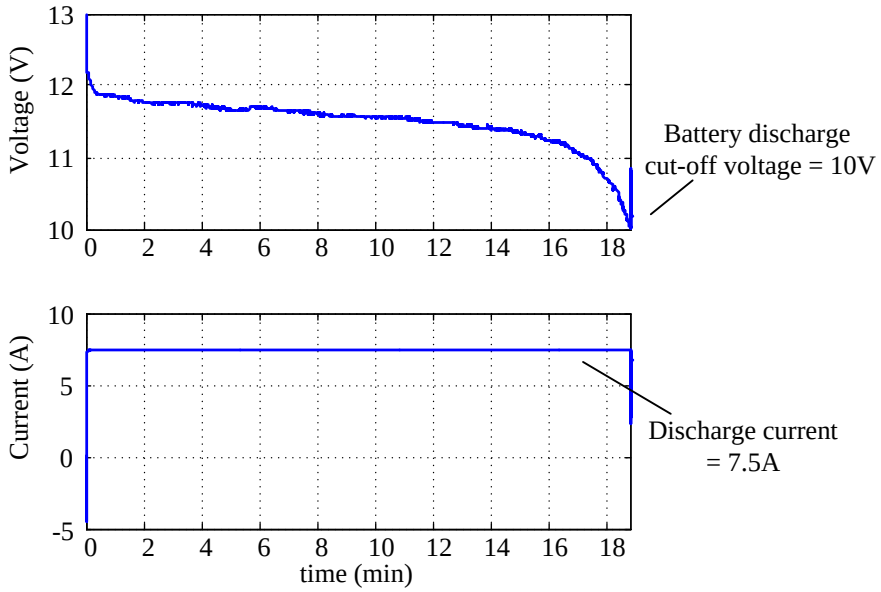


**Fig. 6.13 Battery discharge with 7.5A**

### 6.3.2 Battery State of Charge Estimation

Estimation of the SOC is a difficult task as it is affected by several factors such as temperature, operating point, and battery state of health, to name a few. Various methods

for Li-ion battery SOC estimation are discussed in the literature. These include such methods as estimation using neural networks [113], extended Kalman filters (EKF) [114], fuzzy neural networks [115], and a sliding mode observer [116].

In a hybrid electric drive-train, such as the one considered here, the vehicle controller only needs an estimation of the SOC in order to ensure that the battery is used (either to supply power or to accept charge) within the permissible range (20%-90%). This implies that even a relatively crude estimation of the SOC is normally acceptable in such an application, as it only serves to identify the upper and lower thresholds by the vehicle controller and is not used otherwise [42]. Therefore, a simple method is developed for SOC estimation, which circumvents complexity of neural network and EKF methods.

The SOC estimation is done by calculating the integral of the current over time. The coulombic efficiency of the battery is considered as a constant multiplying the charge current before integration. The state of charge is calculated as follows.

$$SOC = SOC(0) - \int_0^t \alpha \cdot i_b dt \qquad \text{and} \qquad \begin{cases} \alpha = 1 & i_b < 0 \ \text{(charging)} \\ \alpha = 0.98 & i_b > 0 \ \text{(discharging)} \end{cases} \tag{6.1}$$

In this equation, $i_b$ is the battery current in per-unit with the base equal to the rated battery capacity. Battery current is assumed to be negative for charging and positive for discharging. The initial value of the SOC is a challenge for all SOC estimation methods. Since the Li-ion battery has an almost flat SOC vs. terminal voltage characteristics, its open-circuit terminal voltage is not a reliable means for estimating the initial value of the SOC, and holds true for the Li-ion battery used here. For example, **Fig. 6.14** shows the voltage of the battery during rest period after a complete discharge.

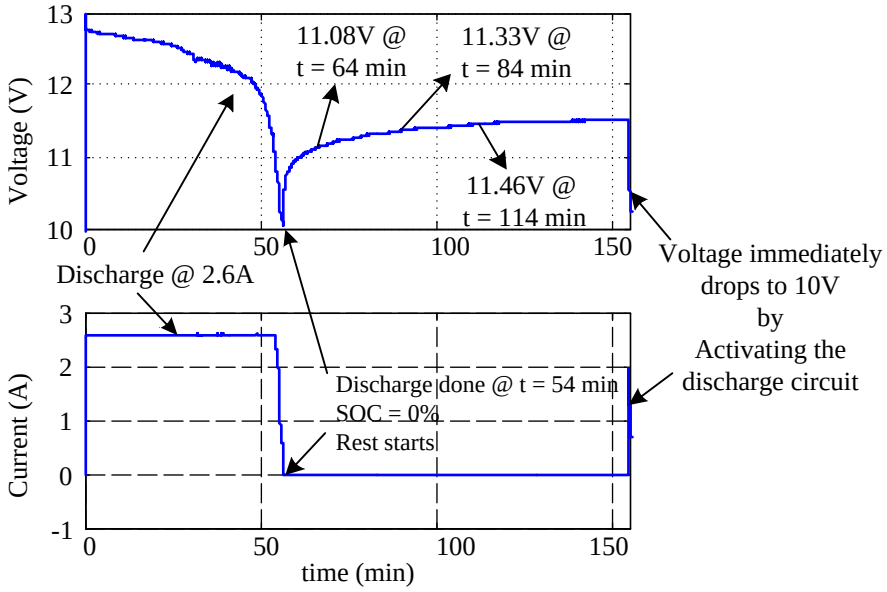


**Fig. 6.14 Battery voltage resting after a discharge**

As seen the battery voltage drops as it is discharged and sharply drops to 10 V just after 50 min, which indicates that the battery is fully discharged. Battery is disconnected at this point and rest period starts. The open-circuit voltage rises rapidly, and is equal to 11.08 V after 10 minutes of rest; it increases to 11.33 V after 30 minutes and eventually 11.46 V after one hour. Note that although the battery voltage is recovering, the SOC is still zero. This is further evidenced by activating the discharge circuit after a long rest. As shown in **Fig. 6.14**, the battery voltage immediately drops to 10V (discharge cut-off voltage) and the discharge stops. It therefore can be concluded that estimating the initial SOC based on the terminal voltage will not be accurate.

In this study, an initial value of 100% (i.e. completely charged) is assumed for the SOC. This allows the vehicle controller to use the battery for propulsion. Correction to the estimated SOC will be made if the battery terminal voltage becomes equal to discharge cut-off voltage of 10 V. At this point the battery SOC is indeed equal to zero and hence the SOC estimator can be accurately re-initialized. A similar correction will

occur if the battery voltage reaches its rated 14.6 V, which indicates that the battery is indeed fully charged. This upper limit for the voltage ensures chemical safety of the battery and prevents excessive charging due to inaccurate coulombic efficiency estimation.

The logic of the SOC estimator is shown in **Fig. 6.15**. Using this logic, the SOC estimation may be inaccurate only until the voltage reaches either the lower or the upper boundary value; at these points the SOC is re-initialized to the corresponding value and is then allowed to swing between the permissible range.

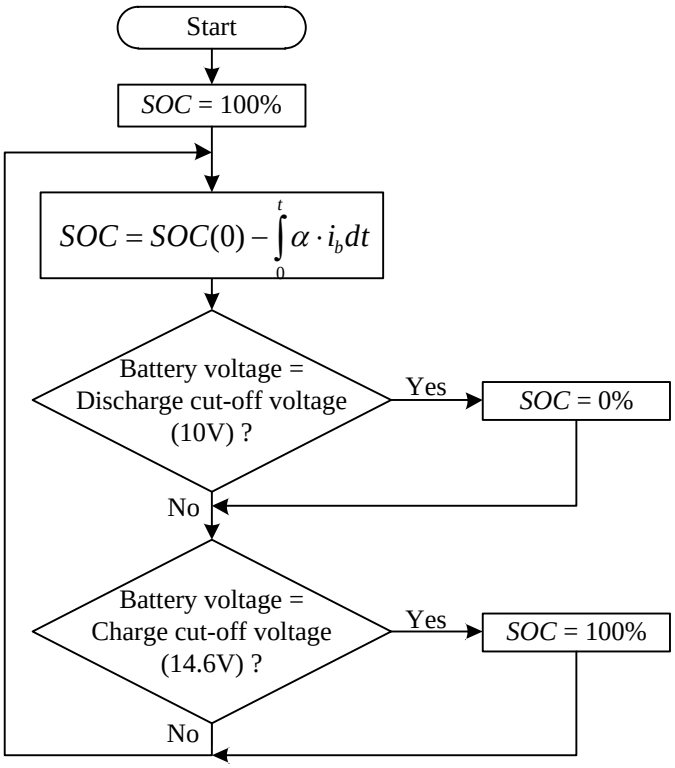


**Fig. 6.15 State-of-charge estimation flowchart**

Battery capacity changes over time, therefore the results may drift if the setup is used for a long period of time. A battery capacity calculator is also implemented in the simulation to overcome this issue. If the rate of change of battery SOC is higher than

expected for a given battery current, it is an indication that the actual battery capacity is lower than assumed capacity. Battery actual capacity is calculated at the end of each charge period and it is used for the following discharge and charge periods.

## 6.4 Battery-In-Loop HIL Simulation Case Study

This section presents the test results obtained using the developed HIL simulation setup for a 600-second driving cycle. The driving cycle includes low speed (30 km/h), moderate speed (50 km/h) and high speed (80 km/h) periods, as well as a braking period to test the regenerative brake in the drive-train. In the simulations the driving cycle is repeated ten times consecutively. Analysis of the simulation results are presented in the following sub-sections.

In another test, the HIL setup is used to simulate the daily driving cycle for the city of Winnipeg (refer to Appendix A). The results of this simulation are reported in 6.4.3. This is an example of using the HIL setup to test the batteries in actual driving condition.

### 6.4.1 Analysis of the Simulation Results

Fig. 6.16 shows the reference speed and the actual vehicle speed for the first 1200 seconds of the HIL simulation. The reference speed (i.e. driving cycle) is shown to be followed closely by the vehicle speed. This is achieved by finely tuning the driver model in the simulation (see Fig. 6.1).

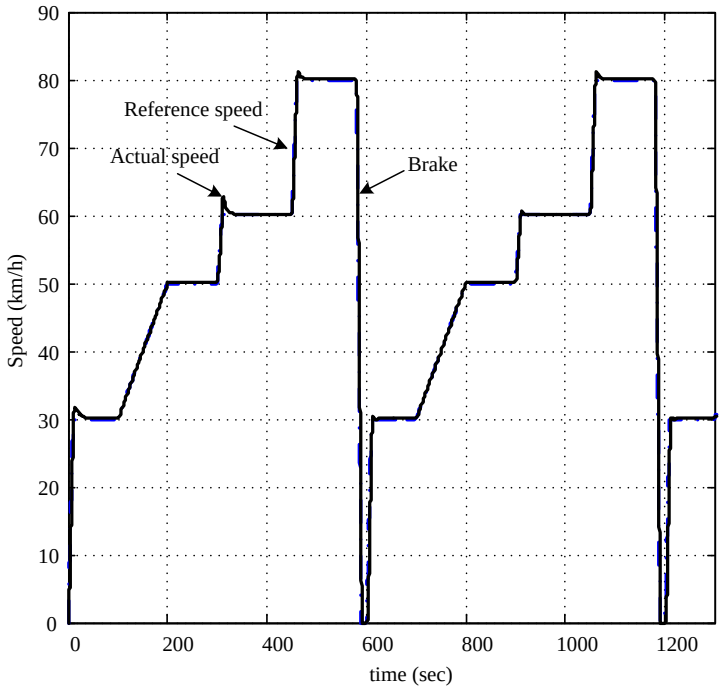


**Fig. 6.16 HIL simulation results, vehicle speed.**

Battery SOC is shown in Fig. 6.17. As stated earlier, the initial SOC is assumed to be 100%; therefore, the vehicle controller engages the battery to provide the required propulsion power. Since the actual battery charge is less than the assumed 100%, the terminal voltage reaches to the discharge cut-off voltage of 10.0 V earlier than the SOC reaches the charge-up level of 20%. At this point, the actual SOC of the battery is equal to zero. The SOC estimator is therefore correctly initialized to zero and the battery starts to charge up. When the battery SOC reaches the upper limit of 90%, charging is terminated and the battery starts to contribute to propulsion. Discharge continues until the battery SOC reaches 20% when it reverts to charging mode.

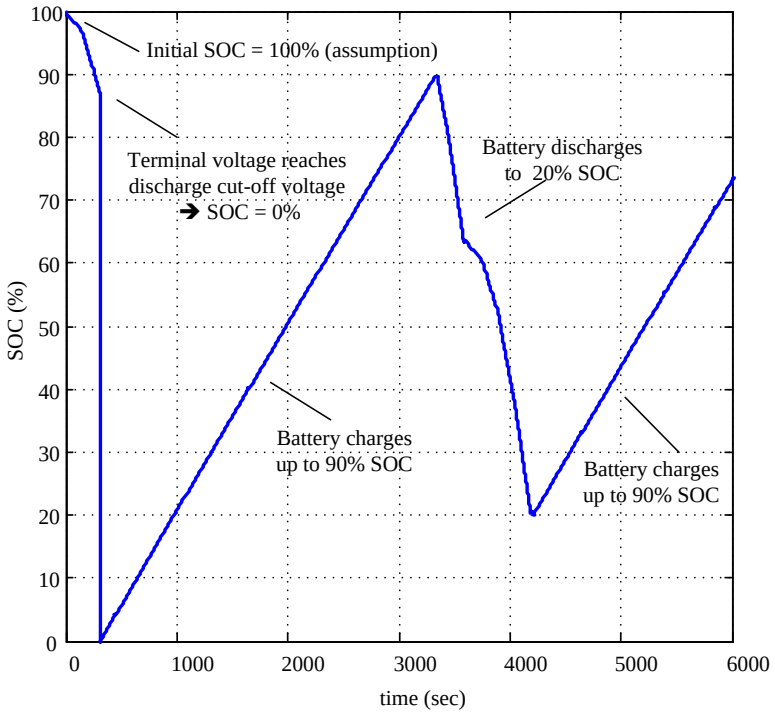


**Fig. 6.17 HIL simulation results, battery SOC.**

MG1 torque, MG2 torque, ICE speed and torque for the first 600 seconds of the simulations are shown in **Fig. 6.18**. As shown, the ICE is idling initially and the vehicle operates in all-electric mode, due to the fact that battery has adequate charge to contribute. When the voltage collapses to 10 V at about 300 sec, i.e. SOC is zero, the ICE is engaged and provides power for propulsion. MG1 torque is then adjusted so that the ICE operates in the most efficient region of its efficiency map. MG1 operates as a generator and feeds the dc link when the ICE is engaged. Prior to this point, MG2 is the only source of power. When the ICE starts, the torque generated by the MG1 drops since part of the required propelling torque is provided by the ICE directly. MG1 torque becomes negative in regenerative braking periods.

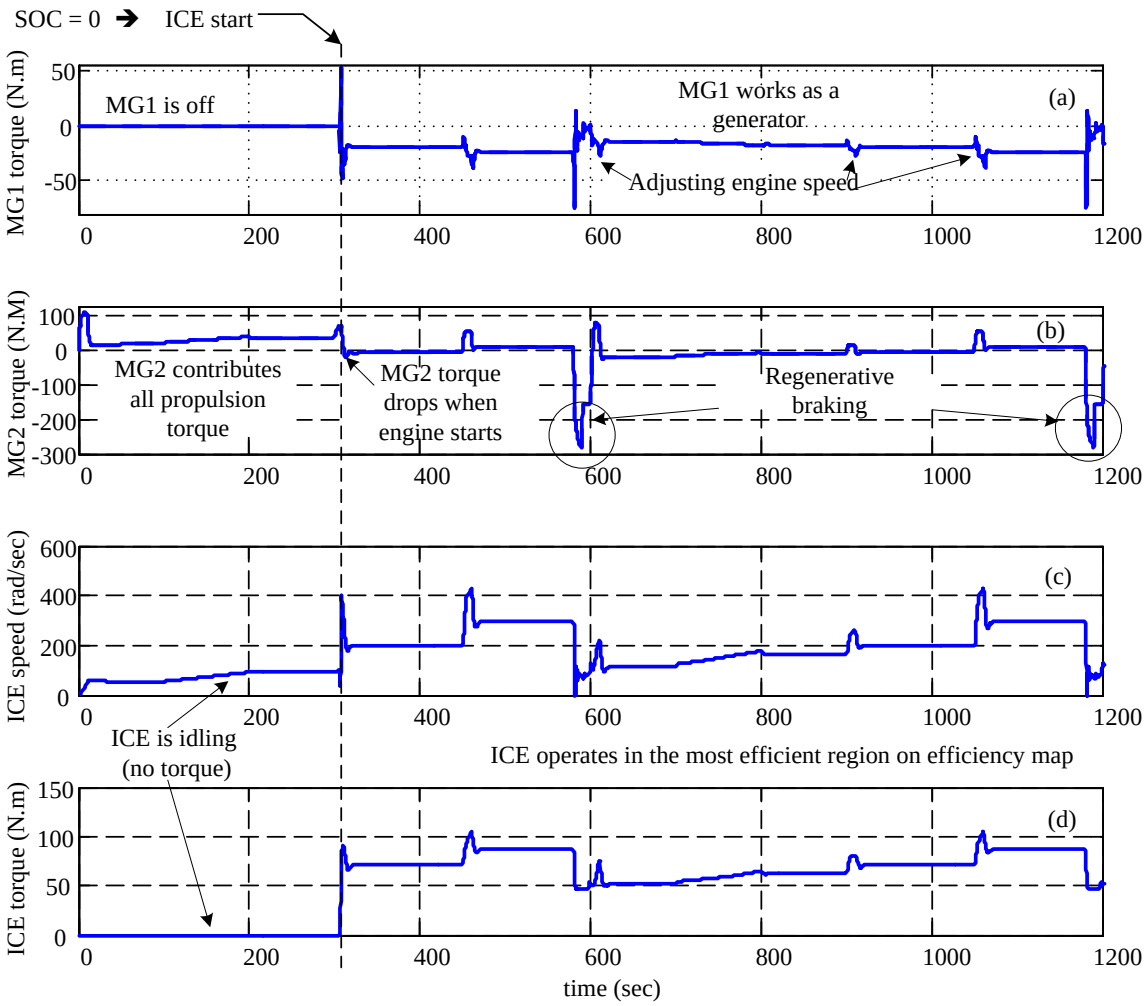


**Fig. 6.18 HIL simulation results, (a) MG1 torque, (b) MG2 torque, (c) ICE speed, (d) ICE Torque**

Battery current is shown in Fig. 6.19. The battery current is positive in discharge and negative in charging periods. The charging and discharging current limits for the battery used in the HIL setup are 2.6 A and 10A, respectively. Due to drive-train dynamics, the battery charging current is not always constant and may vary as shown in **Fig. 6.19.** As stated earlier, the measured values for the battery current and voltage are multiplied by their respective scaling factors as outlined in section 6.2.1 to represent the larger battery pack correctly.

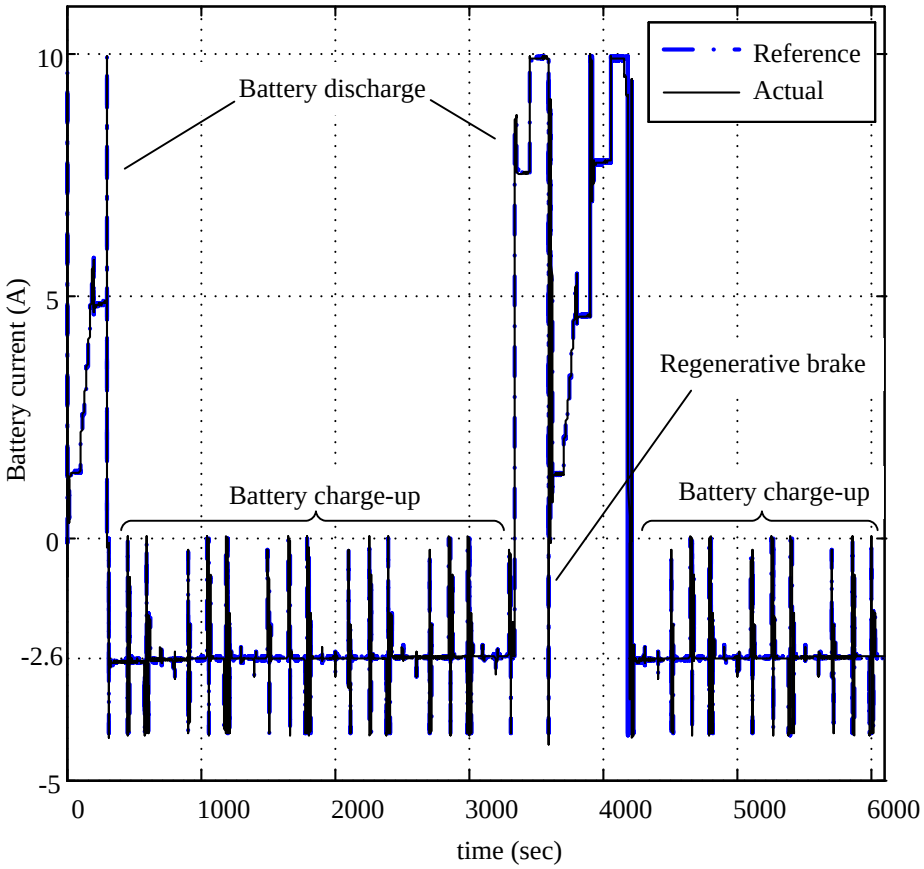


**Fig. 6.19 HIL simulation results, Battery current**

Battery terminal voltage is shown in **Fig. 6.20**. The SOC is reset to zero when the battery voltage has reached the discharge cut-of voltage, and rises during charging period. The voltage waveform, similar to the current waveform, contains sharp transients, which are due to the driving cycle requirements. In the control system of the vehicle a filtered version of the measured terminal voltage is used when comparisons are made to the charge and discharge cut-off voltages to ensure that momentary and transient excursions of the voltage do not unduly interfere with the decisions to stop charging or discharging regimes.

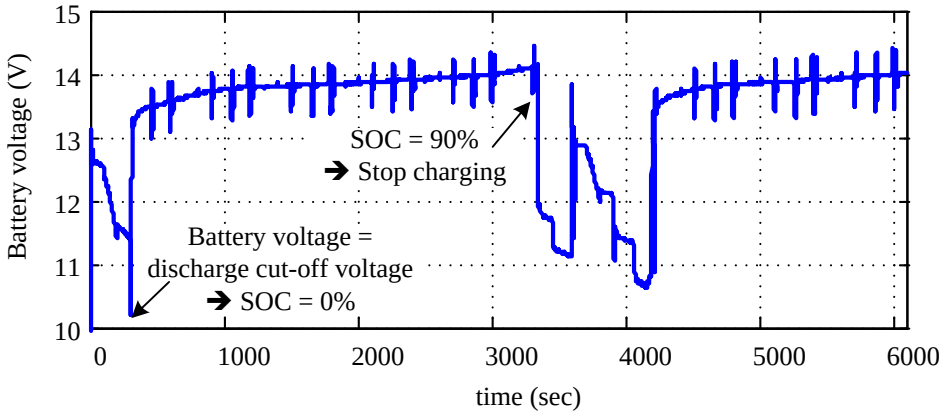


**Fig. 6.20 HIL simulation results, Battery voltage**

### 6.4.2 Battery SOC Estimation Verification

As was mentioned earlier, estimation of the battery SOC is a cornerstone of the developed HIL simulation setup. Therefore it is important to ensure that the developed SOC estimator is indeed reasonably accurate.

To do so the battery-in-loop HIL simulation was started with an unknown initial SOC and was stopped after running the stated driving cycle for 4500 second. Note that the SOC is already correctly initialized (at right after 1000 sec as shown in **Fig. 6.21**) and is calculated using (6.2). At the instant of stoppage, the proposed algorithm has estimated the SOC to be equal to 55.76%. To verify the accuracy of this figure, the actual batteries were discharged at the rated discharge current of 2.6 A, until the batteries were fully depleted. During this period the coulomb counting method of (6.2) was applied, which yielded an estimation of the SOC at the instant of stoppage equal to 56.79%. By fully discharging the battery to an SOC of zero (indicated by its terminal voltage drop to the recommended discharge cut-off value of 10 V) and measuring the initial SOC contents of the unit, this test confirms that the estimation method used in the HIL simulation is reliable and reasonably accurate.

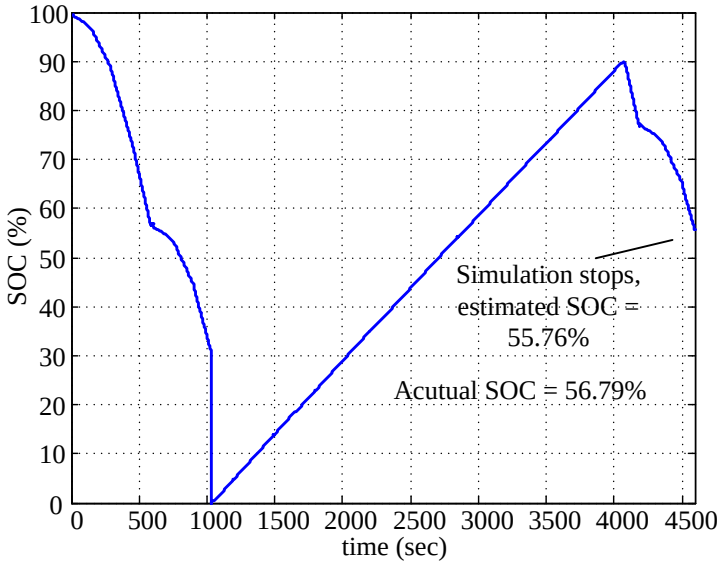


**Fig. 6.21 Battery SOC at the end of drive-train simulation**

Several factors contribute to the actual SOC of a battery pack including aging, temperature and operating conditions. These factors are not directly considered in the proposed SOC estimator and may in fact adversely impact its accuracy in practice. It is however observed that with a decent estimation of the battery efficiency, the proposed method is able to produce acceptable estimations of the SOC.

### 6.4.3 Simulation Results for the Weekday Driving Cycle

In another test, the HIL setup is used to simulate the weekday driving cycle in the city of Winnipeg. This is the same driving cycle that is used in Chapter 3. The weekday driving cycle is a 24 hour cycle. Therefore simulating it on a real-time simulator takes 24 hours. To reduce the simulation time, a modified version of driving cycle is used. In this version, parts of driving cycle corresponding to long off-duty hours (e.g. overnight) are removed. Since the vehicle is powered down during these intervals, removing them does not affect the results. The modified driving cycle is shown in **Fig. 6.22**. Using the

developed HIL setup the performance of the battery can be tested under real driving condition and without installing the battery pack inside an actual vehicle. Battery current, voltage and state-of-charge for the modified weekday driving cycle is shown in **Fig. 6.23**, **Fig. 6.24** and **Fig. 6.25** respectively. Battery current and voltage are measured at the battery terminal and SOC is estimated using the method explained in 6.3.2.

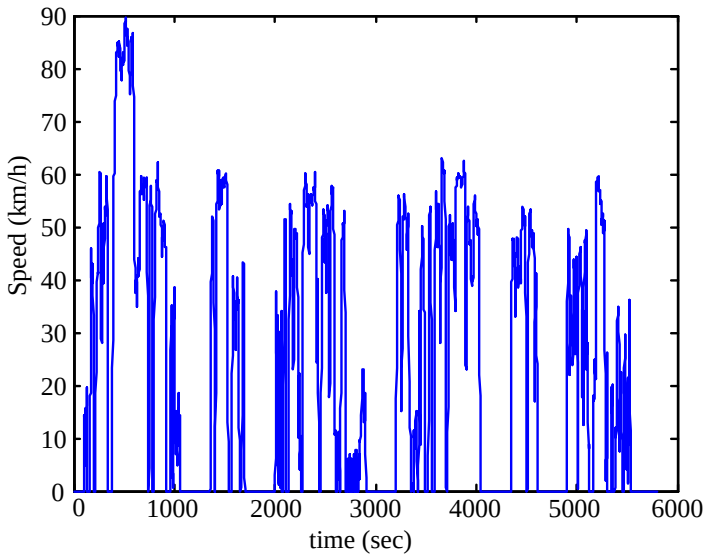


**Fig. 6.22 Modified weekday driving cycle**

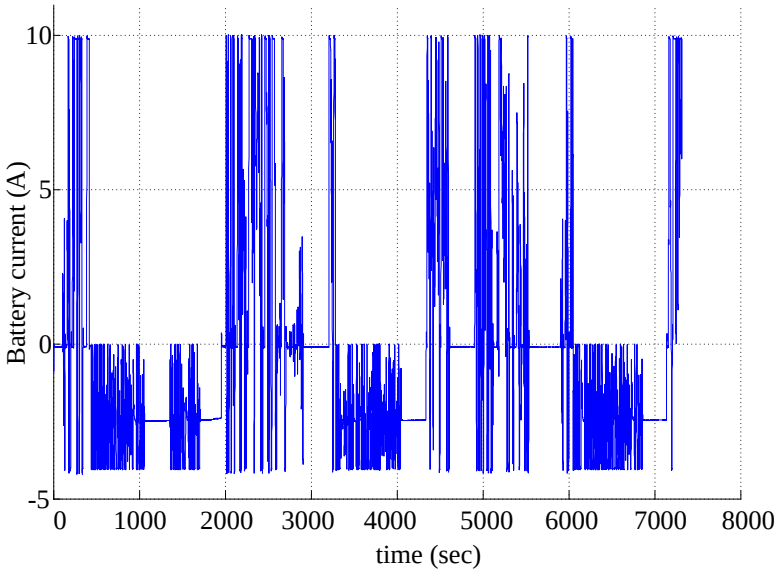


**Fig. 6.23 Battery current for modified weekday driving cycle.**

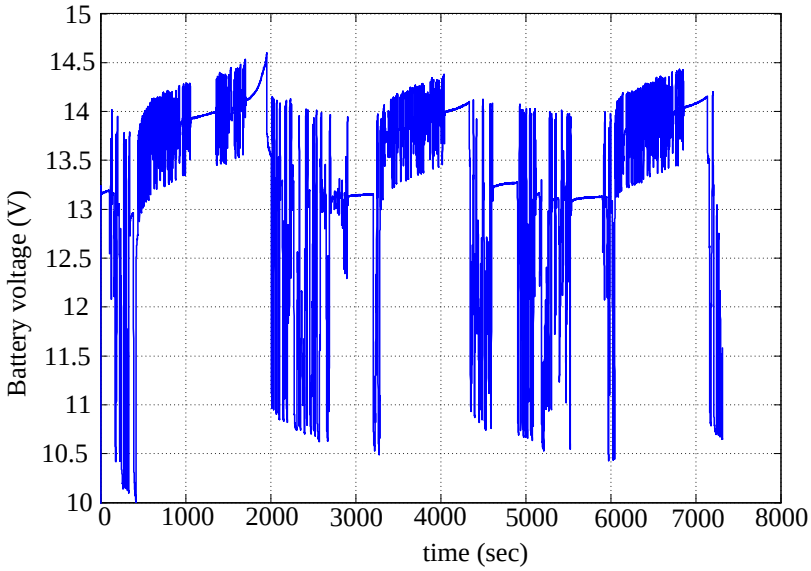


**Fig. 6.24 Battery voltage for modified weekday driving cycle**

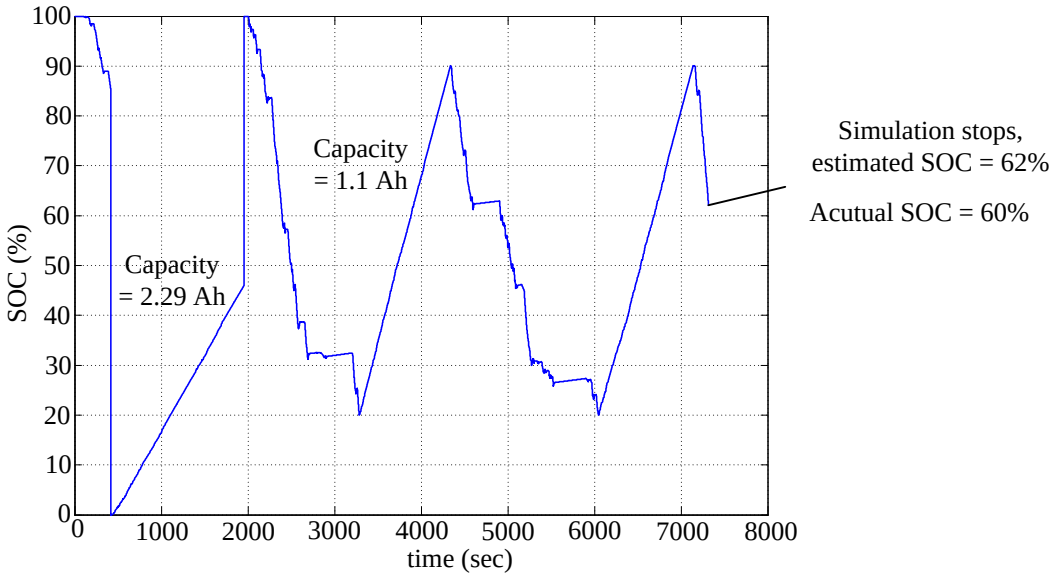


**Fig. 6.25 Battery SOC for modified weekday driving cycle**

During simulations, it was observed that the battery capacity is degraded after numerous charge and discharge cycles. If this change in the battery characteristics is not compensated for in the SOC estimator, charge and discharge of the battery will not happen at the desired SOC levels (20% and 90%). Due to wrong estimation of SOC

battery will operate between 0% and 100% (first discharge and charge cycle in Fig. 6.25). To improve the battery SOC estimator performance and to limit the battery SOC within the desired range, a capacity calculator is added to the SOC estimator. The battery capacity is updated in charging period, if terminal voltage reaches the charge-cut-off voltage before estimator reaches 100 percent. Battery capacity is calculated as follows:

$$C_b = \frac{-1}{3600 \cdot \Delta SOC} \int_{t_0}^{t_1} i_{b,ch} dt \qquad (6.2)$$

where, $C_b$ is the battery capacity, $\Delta$SOC is the change in SOC in the charge period, $t_0$ and $t_1$ are charge start and stop times and $i_{b,ch}$ is the battery charge current (battery current is assumed negative in charge period).

In the results shown in Fig. 6.25, battery capacity is initially set to the nominal value of 2.29 Ah. The actual capacity is lower due to aging. This can be observed in **Fig. 6.24** and **Fig. 6.25**. In the first charging cycle, the battery terminal voltage reaches to charge-cut-off value of 14.6V when SOC estimator shows SOC is around 47%. This shows that the assumed capacity is not correct. The battery capacity is reduced by a factor of 47% and this capacity is used for the rest of simulation. To show the accuracy of the SOC estimator, the simulation is stopped after about two hours at this point the estimated SOC is 62%. The battery is completely discharged and the actual SOC is calculated by coulomb counting. The measured SOC using this method is 60%, which is close to the estimated value.

This simulation shows the importance of HIL simulation with actual batteries in the loop. The battery capacity reduced significantly after a few month of intense use. This has a significant impact on the vehicle performance, and an important test to select a battery for

the drive-train. This phenomenon could not be studied using mathematical battery models.

## 6.5 Chapter Summary and Contributions

In this chapter a hardware-in-loop setup based on Opal-RT simulator is developed for the first time. In this setup a real battery pack is interfaced with the reduced intensity model of hybrid drive-train developed in Chapter 6. The battery behaviour under driving conditions and in different climate conditions (upon using an environmental chamber) can be studied using the developed setup. During the studies it was observed that the battery lost more than half of its capacity over a period of few months. Such observation could not be achieved if mathematical model of the battery was used instead of actual batteries. This emphasises on the importance of HIL simulation with actual batteries in the simulation loop.

A simple SOC estimation technique is proposed and used in this chapter to estimate the state-of-charge of the battery. It is shown that this method has reasonable accuracy for the type of batteries used in the setup. Developing and implementing more accurate SOC-estimation techniques is out of the scope of this research, but can be pursued by other researchers and easily implemented in the developed setup.

# Chapter 7

# Contributions, Conclusions and

# Recommendations for Future Work

## 7.1 Contributions

**i) Developing a steady-state model for a hybrid drive-train**

A steady-state model for a retro-fitted hybrid drive-train was developed in this thesis. This model is able to simulate different battery technologies with variable size. The model utilizes a driving cycle developed for the city of Winnipeg. Using this driving cycle, the results of the simulation are closer to the reality. The ability to model different battery technologies with variable sizes and also inclusion of Winnipeg driving cycle in the model, makes is different from previous works done by other researchers in this field. This part of the thesis is published in IEEE Transactions on Vehicular Technology, in a paper titled: “Battery Storage Sizing in a Retrofitted Plug-in Hybrid Electric Vehicle”, [42].

**ii) Developing a transient model for the hybrid drive-train:**

The power flow model gives a good understanding of the operation of the drive-train but it does not simulate transients of the system. In order to have a better understanding of

the drive-train and also to develop a hardware-in-loop setup for the hybrid drive-train, a transient model for the power-split gear drive-train was developed using Matlab/Simulink for the first time. This model simulates the vehicle drive-train including power-electronic converters with a high level of details and is suitable for Matlab/Simulink based real-time simulators such as Opal-RT.

Part of this section of thesis was presented in the 36th Annual Conference on IEEE Industrial Electronics Society (2010) in a paper titled: "Modeling and simulation of a power-split gear hybrid drive-train", [117].

**iii) Developing a reduced-intensity model for the hybrid drive-train:**

In this thesis, averaging techniques were used for the first time in vehicle drive-train modeling. The reduced-intensity model developed in this thesis models the electric machine drives with lower level of complexity using averaging technique. The resulting model is significantly faster than the detailed model. This allows the real-time simulator to run the model in real-time. Another application of such model is in studies with a repetitive nature, such as parameter optimization. In these studies, use of reduced intensity model will save a significant amount of time. This part of the thesis is published in IEEE Transactions on Power Delivery journal in a paper titled: "Dynamic Average-Value Modeling of Hybrid-Electric Vehicular Power Systems", [118].

**iv) Developing a hardware-in-loop setup for the hybrid drive-train:**

The reduced-intensity model was used to develop a hardware-in-loop setup. This setup uses Opal-RT simulator to run the simulation in real-time and it also uses real Li-ion batteries in the loop of simulation. This setup can be used to study the behaviour of the battery in the vehicle.

The chemical nature of battery makes it difficult to derive a complete model for the battery. Effect of temperature, specially sub-zero temperatures, and also aging of the battery cannot be easily modeled mathematically. This is due to the complexity of the chemical interactions inside the battery and the fact that deriving a simple mathematical model for such interactions is nearly impossible. Therefore it is common practice to use real batteries to study the battery behaviour under different conditions. The hardware-in-loop setup developed in this research can be used to study the behaviour of real battery under different driving conditions.

## 7.2 Conclusions

**i) PSG based hybrid drive-train is a flexible and widely used hybrid drive-train:** Hybrid-electric drive-trains improve overall vehicle efficiency by keeping the engine running in the most efficient way and using the power in the most efficient way. The first step of this project was to study the available hybrid-electric drive-trains. There are three main types of hybrid drive-trains, series, parallel and power-split gear based drive-train. Each drive-train offers some advantages and has some disadvantages. Considering pros and cons of the available drive-trains, the power-split gear based drive-train was selected for this study. This was due to the good performance of this drive-train and the fact that this drive-train is used in many commercially available hybrid electric vehicles. The result of this study is published for general audience in IEEE Canadian review, in an article titled: “Plug-in Hybrid Electric Vehicles: Challenges and Opportunities”, [23].

**ii) Li-ion and NiMH battery chemistries are suitable candidates for hybrid vehicles:** Finding the optimal battery size and chemistry was the next step in this project. A power

flow model of the drive-train was developed for this purpose. The developed model is able to simulate the power flow within the drive-train. The battery technology used in the drive-train and also the size of installed battery pack can be changed in the developed model. Three battery technologies, i.e., Lead-acid, NiMH and Li-ion were studied using this model. The study shows that Lead-Acid battery is not a good candidate for PHEVs. The energy density of Lead-Acid battery is small in comparison with other technologies. Therefore, a large battery pack should be installed on vehicle in order to obtain the required energy storage capability. This introduces extra weight on vehicle and consumes a lot of storage space in vehicle, which is not desirable.

NiMH and Li-ion technologies are both good candidates for PHEV drive-trains. They both offer high energy density and can be used in PHEVs and also electric vehicles. Battery pack cost is usually the determining factor in selecting one of these technologies for the drive-train. Both technologies are used in commercially available hybrid-electric and all-electric vehicles. For instance, Toyota Prius utilizes NiMH battery technology and Mitsubishi i-MiEV uses Li-ion batteries. Li-ion battery is marginally better than NiMH but it comes with a higher price. However, new battery manufacturing methods and also mass production of Li-ion battery technology result in more cost effective Li-ion battery packs. Therefore this technology is selected for this project.

**iii) Averaging technique can be used in drive-train modeling to reduce the computational intensity of the model**

The averaging technique was used in vehicle drive-train modeling for the first time. Simulation results show that the average model gives accurate result in frequencies well below the switching frequency. Therefore, in studies that switching transients are not the point of interest, the average model is a good replacement for the detailed model. This

model can be used to save time in design and optimization stage where multiple simulation runs is necessary. In this thesis this model is used in the hardware-in-loop setup to simulate the vehicle behaviour in real-time.

**iv) Hardware-in-loop simulation shows the actual battery behaviour under different driving conditions.**

In this thesis an HIL setup with real batteries in the simulation loop is developed. The battery pack is made of four Li-ion cells. Using a four quadrant amplifier and signal conditioning modules, a scaled HIL setup is developed. This setup can be used for battery related studies including testing battery performance under different driving conditions and under different climate conditions. HIL setup is also a tool to determine the performance of the vehicle controller and also optimizing it.

Using actual batteries in the simulation loop, the real behaviour of the battery in the vehicle can be studied. For example in the tests done for this thesis over the course of few months, it was observed that the capacity of the battery under test reduced significantly due to aging effect. Such observation was not possible using the mathematical model for the battery.

## 7.3 Recommendations for Future Work

### 7.3.1 Developing an HIL System Using the Transient Model

The HIL system developed in this research is based on an averaged-value model for the drive-train. The average-value model is selected because the available real-time simulator is not able to simulate the transient model in real-time. Although the average-value model

has an acceptable accuracy for this study, the accuracy of the results can be improved using the transient model in the HIL setup. The effect of fast switching transients can be studied using the detailed model for the power electronic converters. These transients are ignored in the average-value model. Implementation of transient model based HIL system requires a real-time simulator with higher computing capability.

### 7.3.2 Vehicle Controller Optimization

The vehicle controller controls all the components in the drive-train and the flow of power between them. Vehicle performance and efficiency can be improved by optimizing the vehicle controller. The developed HIL setup can be used to study the effect of any proposed vehicle controller logic. Using the setup one can also study the long-term effects of the vehicle controller on lifetime of the battery.

### 7.3.3 Study the Vehicle Performance in Cold Climates

One major concern about hybrid-electric and electric vehicles is the poor performance of batteries in sub-zero temperatures. The effect of temperature on vehicle performance can be studied using the HIL setup and an environmental chamber.

### 7.3.4 Apply the concept of hardware-in-loop simulation to other fields

In this thesis the concept of Hardware-in-loop simulation was used to test the batteries in a vehicle. This concept can be extended to other fields, such as robotics or power systems, where battery performance is important.

# Appendix A

# Driving Cycle Development and Description

A real-world daily driving profile has been produced and used for the energy storage optimization of the plug-in hybrid conversion presented in this study. The decision to develop and use an actual driving profile is due to that standard cycles, such as the Urban Dynamometer Driving Schedule (UDDS), have been generated primarily to estimate vehicle emissions inventories and are affected by the restrictions of dynamometer validation tests including limited duration and acceleration/deceleration rates [119].

These standard cycles, therefore, cannot completely emulate the real-world daily power demand of a vehicle. More importantly, they do not provide information on parking times as opportunities for charging in case of PHEVs. Extensive literature survey conducted did not reveal any major reference on the construction of a daily vehicle usage profile for PHEVs; although few works exist that assess the performance of hybrid electric cars in real-world operation. For example, data collected for a fleet in the St. Louis metropolitan area was used in the simulation of energy usage in a PHEV; however no single driving pattern was extracted from the collected data [120]. Fuzzy logic pattern recognition techniques have also been used to perform driving and duty cycle analyses on data collected for a fleet of hybrid electric cars [121].

Another effort to modify standard cycles for better representing real world behavior defined a driver model in simulations using European standard cycle [122]. Driving cycle

generation has also been reported based on the assumption of constant acceleration and deceleration rates and with consideration of the speed limits for road segment in representative areas [123].

## A.2 Drive Cycle Generation and Characterization

In this study data collected from a fleet of 30 cars in the city of Winnipeg has been used to construct a single driving profile representing the average behavior of the fleet. One-month second-by-second time-stamped speed and location of the 30 participant cars are recorded using GPS-based data loggers by the University of Winnipeg. Given that few cities in North America are densely populated over a million people, driving patterns in the city of Winnipeg (with a population of 0.7 million) can be regarded as a reasonable representative of those in the majority of large North American cities. To better represent general driving behavior, data collection in the absence of extreme climate conditions in the month of June has been used to reconstruct the daily driving profiles.

The purpose of this task is to identify two daily driving cycles (one representing weekdays and one for weekends) among the available recorded cycles that most closely represent the *average* behavior of the fleet in terms of a set of characterizing parameters [124]. In addition to the parameters describing kinematics of the cycle, average power demand and average braking power are also used. This is to establish a more comprehensive set of performance measures adequate for evaluation of the power requirements of the driving cycles. This is especially important for power management in hybrid vehicles.

The 900 recorded driving cycles are divided into two groups of weekday and weekend cycles. Average values of the characterizing parameters for the two groups are then calculated. Characteristic parameters of each individual cycle (in both groups) are then measured against their corresponding average values and a figure of merit is calculated and assigned to the individual cycle as follows.

$$\sigma = \left( \sum_{i=1}^{N} \left( \frac{x_i - \overline{x_i}}{\overline{x_i}} \right)^2 / N \right)^{1/2} \qquad \text{(A.1)}$$

where $\sigma$ is the figure of merit, and $N$ is the number of characterizing parameters (17 in this case, as listed in **Table A-1**). The cycles that have the closest set of characterizing parameters to the average values in the weekday and weekend groups are selected and will be referred to as the *candidate cycles* hereinafter.

## A.3 Enhancement of the Candidate Driving Cycles

Note that the two candidate cycles do not necessarily match all the average values uniformly well, although they have the best figures of merit. In order to enhance the quality of the candidate cycles, further processing is done with a view to improve their figure of merit using snippets of other cycles available in the data base. Snippets of driving periods bounded by two consecutive stops, also referred to as micro-trips, are extracted and classified into three traffic groups, namely congested, urban and highway. To classify micro-trips into the three categories, the average speed and acceleration ranges listed in **Table A-2** are used. To improve the figures of merit of the candidate cycles, each of their micro-trips are exchanged with micro-trips of the same traffic group in the data base until the best figures of merit ($\sigma$) are obtained. The average values for the

enhanced candidate cycles are also given in **Table A-1**. The table also shows the relative error between the average values of the fleet and those of the enhanced candidate cycles.

**Table A-1 Characterizing Parameters and Their Values**

| | Parameter | 900 daily driving cycles | | Enhanced representing cycles | |
|---|---|---|---|---|---|
| | | weekday | weekend | Weekday | weekend |
| 1 | Average speed of the entire driving cycle in km/h | 30.9 | 37.2 | 33.0 (6.8%) | 34.8 |
| 2 | Average running speed in km/h | 37.7 | 49.8 | 38.9 | 43.1 |
| 3 | Total daily distance traveled in km | 35.7 | 37.0 | 37.3 | 38.9 |
| 4 | Average acceleration of all acceleration phases in $m/s^2$ | 0.56 | 0.53 | 0.48 | 0.63 |
| 5 | Average deceleration of all deceleration phases in $m/s^2$ | -0.57 | -0.54 | -0.52 | -0.63 |
| 6 | Average number of change in acceleration rate (+/-) in one driving period | 17 | 11 | 15 | 9 |
| 7 | Average daily power demand in kW | 6.4 | 7.5 | 5.5 | 8.9 |
| 8 | Maximum power demand in kW | 33.8 | 57.8 | 28.4 | 52.2 |
| 9 | Total daily energy demand in Mj | 13.3 | 19.7 | 13.7 | 18.8 |
| 10 | Average daily braking power in kW | -5.6 | -6.5 | -5.1 | -7.5 |
| 11 | Root mean square of acceleration in $m/s^2$ | 0.71 | 0.70 | 0.61 | 0.80 |
| 12 | Average length of a driving period in km | 0.44 | 0.90 | 0.48 | 0.97 |
| 13 | Time percentage of Idling (zero velocity) in % | 17.2 | 19.9 | 15.0 | 18.0 |
| 14 | Time percentage of acceleration: acceleration>$0.1m/s^2$ in % | 28.8 | 27.5 | 30.9 | 29.1 |
| 15 | Time percentage of Cruising (acceleration [-0.1,0.1] $m/s^2$, speed>5m/s) in % | 10.2 | 13.1 | 9.1 | 10.7 |
| 16 | Time percentage of deceleration: acceleration <-$0.1m/s^2$ % | 28.0 | 26.5 | 29.1 | 29.0 |
| 17 | Time percentage of creeping (acceleration [-0.1,0.1] $m/s^2$, speed<5m/s) in % | 16.0 | 13.0 | 15.9 | 13.2 |

The variations in the speed and acceleration can change the power demand accordingly, and hence the time percentages spent in various speed and acceleration ranges provide important information about power demand in the modes of driving listed in **Table A-2**. Speed-acceleration frequency distribution (SAFD) plots provide the needed information about the time proportions of individual driving modes; they are used in this

work as an additional measure to demonstrate how well the final driving cycles match the collected data [125].

**Table A-2 Micro-trip Characteristics**

| Traffic category | Average speed | Acceleration |
|---|---|---|
| Congested | Low: < 5 km/h | Mild: [-0.1,0.1] $m/s^2$ |
| Urban | Moderate: [5,40] km/h | Harsh: [-3.0,3.0] $m/s^2$ |
| Highway | High: > 40 km/h | Moderate: [-1.0,1.0] $m/s^2$ |

Note that the use of micro-trips of the same traffic group serves to maintain the matching of the SAFD of the two candidate cycles to that the SAFD of all recorded cycles. A maximum 5% deviation from average daily energy demand for final driving cycles is allowed in the construction of the enhanced candidate cycles. It is important to note that the driving profiles constructed this way are not entirely random combinations of micro-trips, although random combinations of micro-trips has been used by other researchers as a means for constructing representative driving cycles [126].

This feature is particularly important for the study presented here because the sequence of micro-trips from different traffic groups that affect power demand between charging opportunity occasions is essentially determined by the candidate cycles, which have moderate yet realistic patterns. **Fig. A.01** shows the enhanced weekday and weekend candidate driving cycles.

Since parking periods and locations of the vehicles in the fleet under survey are time-stamped, it is possible to statistically analyze the probability, time and duration of parking events. Most probable parking times and average duration for each parking event

are included to adequately reflect daily driving and parking profile for the PHEV design considerations.

Durations of the weekday and weekend cycles are 4071 sec and 4023 sec, respectively. Maximum velocity is higher in the weekend cycle (114 km/hr) while in weekday cycle the maximum velocity is 89.6 km/hr. The driving pattern in the weekend is slightly more aggressive due to higher acceleration and deceleration rates. A consequence of the differences in driving patterns in weekdays and weekends is higher power demand for weekends.

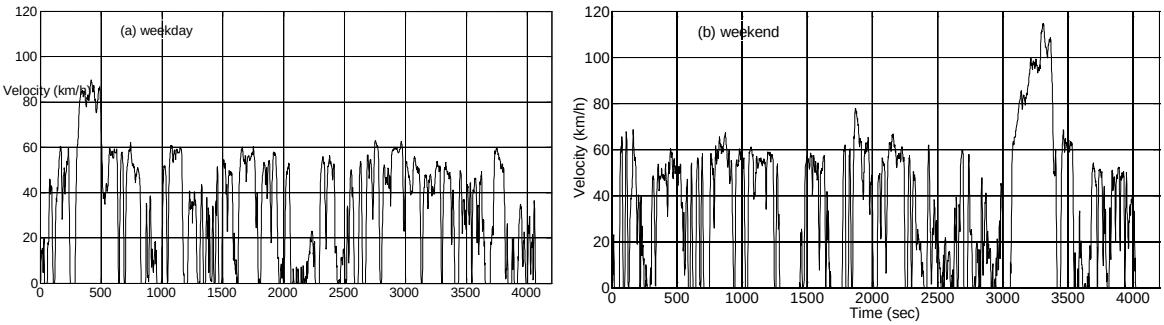


**Fig. A.01 Enhanced candidate driving cycles. (a) weekday; (b) weekend.**

**Fig. A.02** shows the SAFD plot for weekday and weekend enhanced candidate driving cycles. Another difference between the two patterns is the higher probability of driving at moderate speeds (35-50 km/hr) in the weekday pattern. Higher acceleration and deceleration rates in the weekend cycle are also considerable when compared with the weekday driving cycle.

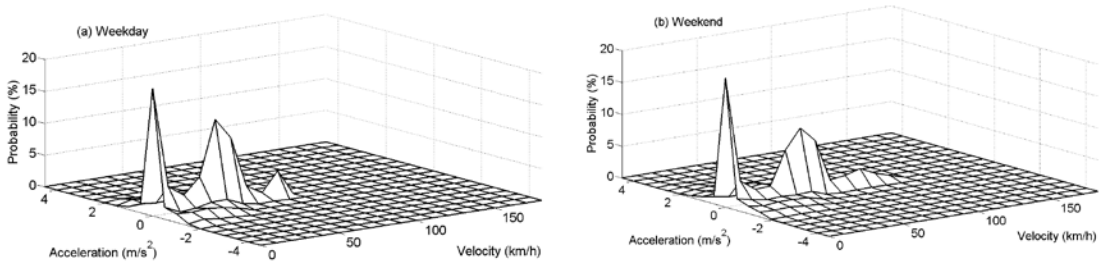


**Fig. A.02 SAFD plots for the enhanced candidate driving cycles. (a) weekday; (b) weekend.**

**Fig. A.003** (a) and (b) show the probability of parking for less than three hours as a function of time for weekday and weekend drive cycles. In this study short parking durations (less than three hours) have not been considered for opportunity charging. As shown in **Fig. A.003** (a) short-duration parking most probably takes place between 12:00 PM to 18:00 in weekdays and between 12:00 PM to 16:00 in weekends. In the opportunity charging scenario used in this paper, it is further assumed that the driver is not reluctant to plug-in during weekends and is equally charge conscious throughout the weekdays. Based on the information obtained about parking times and duration of parking events, several short and long parking events as well as overnight parking periods were included in the driving cycles, resulting in two 86,400-s daily profiles needed for further analysis in the simulations.

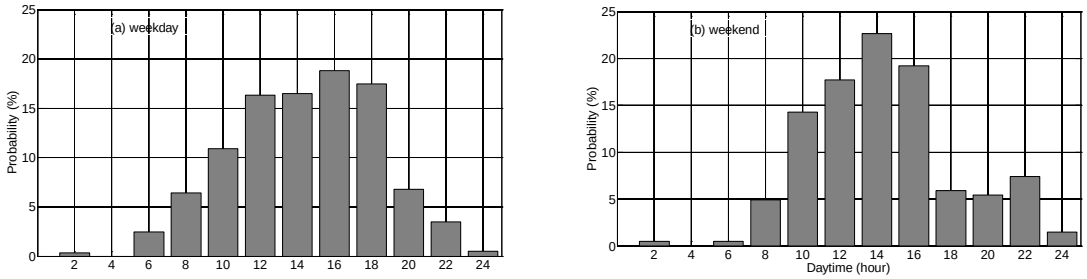


**Fig. A.003 Probability of short duration parking (less than 3 hours) for opportunity charging scenarios. (a) weekday; (b) weekend.**

# Appendix B

# Dynamic AC Machine Modeling

The per-phase model of ac machines is widely used in steady-state analysis and designs [127]. In addition to the steady-state model, a dynamic model is necessary to understand ac machine control methods such as vector control and direct torque control method. The dynamic model is derived from the time-domain equations of the machine and models the transient behavior of an ac machine.

In a salient pole ac machine, parameters such as phase inductance change as the rotor turns in the machine. This introduces a set of time-varying variables to the machine equations. Therefore, the dynamic model consists of a set of time-varying equations for each phase [64]. This time-varying system is hard to analyze but there are some methods to simplify this system to a time-invariant system. R. H. Park in 1929, proposed a matrix transformation that transforms this time-varying system in the time domain to a time-independent system in a new domain [128].

## B.1 DQ0 Transformation

The Park's transform transfers variable from a time-varying domain, i.e. *abc domain*, to a time-independent domain, i.e. *dq0 domain*. The transformation is done as shown below.

$$\vec{f}_{dq0} = K_S \vec{f}_{abc} \tag{B-1}$$

where $\vec{f}_{abc}$ is a vector of variables in abc domain, $\vec{f}_{dq0}$ is a vector of variable in dq0 domain, and $K_S$ is the transformation matrix. These matrices are shown in extended form below.

$$\vec{f}_{dq0} = \begin{bmatrix} f_d \\ f_q \\ f_0 \end{bmatrix}, \quad \vec{f}_{abc} = \begin{bmatrix} f_a \\ f_b \\ f_c \end{bmatrix} \text{ and } K_s = \frac{2}{3}\begin{bmatrix} \cos(\theta) & \cos\left(\theta - \frac{2\pi}{3}\right) & \cos\left(\theta + \frac{2\pi}{3}\right) \\ \sin(\theta) & \sin\left(\theta - \frac{2\pi}{3}\right) & \sin\left(\theta + \frac{2\pi}{3}\right) \\ \frac{1}{2} & \frac{1}{2} & \frac{1}{2} \end{bmatrix} \quad \text{(B-2)}$$

The Park's transform is an invertible transform. This means that any vector in dq0 domain can be uniquely transferred back to its corresponding vector in abc domain. The inverse of Park's transform is as follows.

$$K_s^{-1} = \begin{bmatrix} \cos(\theta) & \sin(\theta) & 1 \\ \cos\left(\theta - \frac{2\pi}{3}\right) & \sin\left(\theta - \frac{2\pi}{3}\right) & 1 \\ \cos\left(\theta + \frac{2\pi}{3}\right) & \sin\left(\theta + \frac{2\pi}{3}\right) & 1 \end{bmatrix} \quad \text{(B-3)}$$

Using Park's transform, the machine equations can be transferred from abc domain to dq0 domain. The flux linkage of the stator and rotor windings in abc domain are expressed as follows.

$$\begin{bmatrix} \vec{\lambda}_{abc} \\ \vec{\lambda}_{abcr} \end{bmatrix} = \begin{bmatrix} L_s & L_{sr} \\ (L_{sr})^T & L_r \end{bmatrix} \begin{bmatrix} \vec{i}_{abcs} \\ \vec{i}_{abcr} \end{bmatrix} \quad \text{(B-4)}$$

where $\lambda_{abc} = [\lambda_{as} \quad \lambda_{bs} \quad \lambda_{cs}]$ is the stator flux linkage and $\lambda_{abcr} = [\lambda_{ar} \quad \lambda_{br} \quad \lambda_{cr}]$ is the rotor flux linkage. The inductance matrix is derived from the geometry of the machine and winding parameters and explained in [64].

The voltage equations are as follows.

$$\begin{aligned} \vec{v}_{abcs} &= \vec{r}_s \vec{i}_{abcs} + {}^{d}\!/_{dt}\, \vec{\lambda}_{abcs} \\ \vec{v}_{abcr} &= \vec{r}_r \vec{i}_{abcr} + {}^{d}\!/_{dt}\, \vec{\lambda}_{abcr} \end{aligned} \tag{B-5}$$

where $\vec{v}_{abcs}$ is the stator voltage vector, $\vec{v}_{abcr}$ is the rotor voltage vector, $\vec{i}_{abcs}$ is the stator current vector, $\vec{i}_{abcr}$ is the rotor current vector, $\vec{r}_s$ is the stator resistance vector, $\vec{r}_r$ is the rotor resistance vector, $\vec{\lambda}_{abcs}$ is the stator flux linkage vector, and, $\vec{\lambda}_{abcr}$ is the rotor flux linkage vector.

Flux linkage and voltage equations can be transferred to dq0 domain using the Park's transform. Transformation and simplification result in following flux linkage equations.

$$\begin{aligned} \lambda_{qs} &= (L_{ls} + L_M) i_{qs} + L_M i_{qr} \\ \lambda_{ds} &= (L_{ls} + L_M) i_{ds} + L_M i_{dr} \\ \lambda_{0s} &= L_{ls} i_{0s} \\ \lambda_{qr} &= (L_{lr} + L_M) i_{qr} + L_M i_{qs} \\ \lambda_{dr} &= (L_{lr} + L_M) i_{dr} + L_M i_{ds} \\ \lambda_{0r} &= L_{lr} i_{0r} \end{aligned} \tag{B-6}$$

where $\lambda_{ds}, \lambda_{qs}$ and $\lambda_{0s}$ are stator flux linkage elements in dq0 domain and $\lambda_{dr}, \lambda_{qr}$ and $\lambda_{0r}$ are rotor flux linkage elements in this domain. Similarly, $i_{ds}$, $i_{qs}, i_{0s}$ are stator current components and $i_{dr}$, $i_{qr}$ and $i_{0r}$ are rotor current components. $L_{ls}$ is the stator leakage inductance, $L_{lr}$ is the rotor leakage inductance and $L_M$ is the mutual inductance between the stator and rotor.

The voltage equations in the dq0 domain are as follows.

$$\begin{aligned}
v_{qs} &= r_s i_{qs} + \omega\lambda_{ds} + {}^{d}\!/_{dt}\,\lambda_{qs} \\
v_{ds} &= r_s i_{ds} - \omega\lambda_{qs} + {}^{d}\!/_{dt}\,\lambda_{ds} \\
v_{0s} &= r_s i_{0s} + {}^{d}\!/_{dt}\,\lambda_{0s} \\
v_{qr} &= r_r i_{qr} + (\omega - \omega_r)\lambda_{dr} + {}^{d}\!/_{dt}\,\lambda_{qr} = 0 \\
v_{dr} &= r_r i_{dr} - (\omega - \omega_r)\lambda_{qr} + {}^{d}\!/_{dt}\,\lambda_{dr} = 0 \\
v_{0r} &= r_r i_{0r} + {}^{d}\!/_{dt}\,\lambda_{0r}
\end{aligned} \tag{B-7}$$

where $v_{ds}$, $v_{qs}$ and $v_{0s}$ are stator flux linkage elements in dq0 domain and $v_{dr}$, $v_{qr}$ and $v_{0r}$ are rotor flux linkage elements in this domain. $r_s$ is the stator winding resistance, $r_r$ is rotor winding resistance, $\omega$ is the rotor speed and $\omega_r$ is the synchronous speed. Shaft torque can be calculated from the flux linkage equations and voltage equations.

$$T_e = \frac{3}{2}\frac{P}{2}\frac{L_M}{L_{lr} + L_M}\left(i_{qs}\lambda_{dr} - i_{ds}\lambda_{qr}\right) \tag{B-8}$$

where $T_e$ is the produced torque and $P$ is the number of poles in the machine. Using the shaft torque and the mechanical equation of the machine, the mechanical dynamics of the machine can be modeled.

$$T_e - T_l = J\frac{d\omega}{dt} + B\omega \tag{B-9}$$

In this equation, $T_l$ is the load torque on the machine, $J$ is the inertia, and $B$ is the friction coefficient.

# Appendix C

# PMSM Model Coefficients

Coefficients $A_1$-$A_4$ and $B_1$-$B_4$ in (4.8) are as follows.

$$A_1 = \frac{\left(\frac{\rho+1}{\rho}\right)\left(1-\frac{J_s}{J_s+\rho^2}\right)}{J_c+J_s-\frac{J_s^2}{\rho^2+J_s}},\ A_2 = \frac{\rho^2+J_s}{\rho^2\left(J_c+J_s\right)+J_cJ_s+2J_s^2} \tag{C-1}$$

$$A_3 = \frac{\frac{J_s(1+\rho)}{J_s+\rho^2}}{J_c+J_s-\frac{J_s^2}{\rho^2+J_s}},\ A_4 = \frac{(1+\rho)\left(\frac{J_s}{R_f}\right)}{\rho^2\left(J_c+J_s\right)+J_cJ_s} \tag{C-2}$$

$$B_1 = \frac{A_1J_s(1+\rho)-\rho}{\rho^2+J_s},\ B_2 = \frac{A_2J_s(1+\rho)}{\rho^2+J_s} \tag{C-3}$$

$$B_3 = \frac{\rho^2}{\rho^2+J_s}+\frac{A_3J_s(1+\rho)}{\rho^2+J_s},\ B_4 = \frac{-\rho^2}{R_f\left(\rho^2+J_s\right)}+\frac{A_4J_s(1+\rho)}{\rho^2+J_s} \tag{C-4}$$

Where $\rho$ is the power-split gear ratio defined as: $\rho = \frac{S}{R}$, $J_s$ is the sun gear inertia, $J_c$ is the carrier inertia and $R_f$ is the final drive ratio.

# References


[1] J. Sousanis. (Aug 2011, World vehicle population tops 1 billion units. *Wards Auto* [online]. Available: http://wardsauto.com/ar/world_vehicle_population_110815.

[2] International Transport Forum. 2011).Transport outlook, meeting the needs of 9 billion people. [online]. pp. 5. Available: http://www.internationaltransportforum.org/Pub/pdf/11Outlook.pdf.

[3] International organization of motor vehicle manufacturers. [online]. Available: http://oica.net/category/economic-contributions/auto-jobs/.

[4] Erik Eckermann, *World History of the Automobile.* SAE, 2001.

[5] B. K. Sovacool, "Early modes of transport in the United States: Lessons for modern energy policymakers," *Policy and Society,* vol. 27, pp. 411-427, March, 2009.

[6] M. Ehsani, *Modern Electric, Hybrid Electric, and Fuel Cell Vehicles : Fundamentals, Theory, and Design.* Boca Raton: CRC Press, 2005.

[7] B.C. Ministry of Environment. 2007).Environmental trends in british columbia [online]. Available: http://www.env.gov.bc.ca/soe/et07/04_climate_change/technical_paper/climate_change.pdf.

[8] M. Lawton and T. Andrews. (July, 1999).Fueling the force in the army after next revolution or evolution? [online]. pp. 8-12. Available: Http://www.env.gov.bc.ca/soe/et07/04_climate_change/technical_paper/climate_change.pdf.

[9] J. B. Heywood. (2006, September). Fueling our transportation future. *Scientific American* pp. 60-63.

[10] L. Nissan website. Nissan leaf performance. [online]. Available: http://www.nissanusa.com/leaf-electric-car/faq/list/performance.

[11] A. Emadi, M. Ehsani and J. M. Miller, "Vehicular electric power systems," vol. 22, pp. 496, 2004.

[12] J. M. Miller, *Propulsion Systems for Hybrid Vehicles.* Stevenage, UK: Institution of Electrical Engineers, 2004.

[13] J. Romm, "The car and fuel of the future," *Energy Policy,* vol. 34, pp. 2609-2614, November, 2006.

[14] J. Voorhees. (July, 2009).Obama favors plug-in hybrids over hydrogen vehicles. *Scientific American* [online]. Available: http://www.scientificamerican.com/article.cfm?id=hybrid-cars-plug-in-obama-stimulus-money.

[15] J. Voelcker, "Plugging Away In A Prius," *IEEE Spectrum,* vol. 45, pp. 30-48, May, 2008.

[16] J. Voelcker, "How green is my plug-in?" *IEEE Spectrum,* vol. 46, pp. 42-58, March. 2009.

[17] S. Dhameja, *Electric Vehicle Battery Systems.* Boston: Newnes, 2001.

[18] Yimin Gao, M. Ehsani and J. M. Miller, "Hybrid electric vehicle: Overview and state of the art," in *Industrial Electronics, 2005. ISIE 2005. Proceedings of the IEEE International Symposium on,* 2005, pp. 307-316.
[19] A. Emadi, *Handbook of Automotive Power Electronics and Motor Drives.* Boca Raton: Taylor & Francis, 2005.
[20] V. Wouk, "Hybrids: then and now," *Spectrum, IEEE,* vol. 32, pp. 16-21, 1995.
[21] A. Emadi, K. Rajashekara, S. S. Williamson and S. M. Lukic, "Topological overview of hybrid electric and fuel cell vehicular power system architectures and configurations," *Vehicular Technology, IEEE Transactions on,* vol. 54, pp. 763-770, 2005.
[22] J. Liu, H. Peng and Z. Filipi, "Modeling and control analysis of toyota hybrid system," in *Proceedings of IEEE/ASME International Conference on Advanced Intelligent Mechatronics,* 2005, pp. 134-139.
[23] S. Filizadeh and E. Tara, "Plug-in Hybrid Electric Vehicles: Challenges and Opportunities," *IEEE Canadian Review,* vol. 59, pp. 11-14, December, 2008.
[24] M. Ehsani, Yimin Gao and J. M. Miller, "Hybrid Electric Vehicles: Architecture and Motor Drives," *Proceedings of the IEEE,* vol. 95, pp. 719-728, 2007.
[25] Li Zhai and Shouquan Dong, "Electronic differential speed steering control for four in-wheel motors independent drive vehicle," in *Intelligent Control and Automation (WCICA), 2011 9th World Congress on,* 2011, pp. 780-783.
[26] Fu Zhumu, Hou Gaolei and Gao Aiyun, "Modeling and simulation for parallel hybrid electric vehicle powertrain," in *Advanced Mechatronic Systems (ICAMechS), 2011 International Conference on,* 2011, pp. 114-117.
[27] Chan-Chiao Lin, Huei Peng, J. W. Grizzle and Jun-Mo Kang, "Power management strategy for a parallel hybrid electric truck," *Control Systems Technology, IEEE Transactions on,* vol. 11, pp. 839-849, 2003.
[28] M. Shams-Zahraei and A. Z. Kouzani, "A study on plug-in hybrid electic vehicles," in *TENCON 2009 - 2009 IEEE Region 10 Conference,* 2009, pp. 1-5.
[29] S. Sasaki, "Toyota's newly developed hybrid powertrain," in *Power Semiconductor Devices and ICs, 1998. ISPSD 98. Proceedings of the 10th International Symposium on,* 1998, pp. 17-22.
[30] J. Liu and H. Peng, "Control optimization for a power-split hybrid vehicle," in *American Control Conference,* 2006, pp. 466-471.
[31] M. Bertoluzzo, P. Bolognesi, G. Buja and P. Thakura, "Role and technology of the power split apparatus in hybrid electric vehicles," in *Industrial Electronics Society, 2007. IECON 2007. 33rd Annual Conference of the IEEE,* 2007, pp. 256-261.
[32] R. Ghorbani, E. Bibeau and S. Filizadeh, "On Conversion of Hybrid Electric Vehicles to Plug-In," *IEEE Transactions on Vehicular Technology,* vol. 59, pp. 2016-2020, May, 2010.
[33] K. B. Wipke, M. R. Cuddy and S. D. Burch, "ADVISOR 2.1: a user-friendly advanced powertrain simulation using a combined backward/forward approach," *IEEE Transactions on Vehicular Technology,* vol. 48, pp. 1751-61, November, 1999.

[34] H. A. Rakha, Kyoungho Ahn, W. Faris and K. S. Moran, "Simple Vehicle Powertrain Model for Modeling Intelligent Vehicle Applications," vol. 13, pp. 770-780, June, 2012.
[35] A. F. Burke, "Batteries and Ultracapacitors for Electric, Hybrid, and Fuel Cell Vehicles," *Proceedings of the IEEE,* vol. 95, pp. 806-820, April, 2007.
[36] R. Sehab, B. Barbedette and M. Chauvin, "Electric vehicle drivetrain: Sizing and validation using general and particular mission profiles," in *Mechatronics (ICM), 2011 IEEE International Conference on,* 2011, pp. 77-83.
[37] S. Fish and T. B. Savoie, "Simulation-based optimal sizing of hybrid electric vehicle components for specific combat missions," *IEEE Transactions on Magnetics,* vol. 37, pp. 485-488, January, 2001.
[38] M. Amrhein and P. T. Krein, "Dynamic simulation for analysis of hybrid electric vehicle system and subsystem interactions, including power electronics," *IEEE Transactions on Vehicular Technology,* vol. 54, pp. 825-836, 2005.
[39] S. R. Cikanek, K. E. Bailey and B. K. Powell, "Parallel hybrid electric vehicle dynamic model and powertrain control," in *Proceedings of the American Control Conference,* 1997, pp. 684-688.
[40] J. Liu and H. Peng, "Modeling and control of a power-split hybrid vehicle," *IEEE Transactions on Control System Technology,* vol. 16, pp. 1242-1251, 2008.
[41] J. P. Aditya and M. Ferdowsi, "Comparison of NiMH and li-ion batteries in automotive applications," in *Vehicle Power and Propulsion Conference, 2008. VPPC '08. IEEE,* 2008, pp. 1-6.
[42] E. Tara, S. Shahidinejad, S. Filizadeh and E. Bibeau, "Battery Storage Sizing in a Retrofitted Plug-in Hybrid Electric Vehicle," *IEEE Transactions on Vehicular Technology,* vol. 59, pp. 2786-2794, July, 2010.
[43] K. Popp and W. O. Schiehlen, *Ground Vehicle Dynamics.* Berlin: Springer, 2010.
[44] S. S. Williamson, A. Emadi and K. Rajashekara, "Comprehensive Efficiency Modeling of Electric Traction Motor Drives for Hybrid Electric Vehicle Propulsion Applications," *Vehicular Technology, IEEE Transactions on,* vol. 56, pp. 1561-1572, 2007.
[45] Yongsug Suh, J. Steinke and P. Steimer, "A study on efficiency of voltage source and current source converter systems for large motor drives," in *Power Electronics Specialists Conference, 2006. PESC '06. 37th IEEE,* 2006, pp. 1-7.
[46] A. Pesaran, "Battery choices and potential requirements for plug-in hybrids," *Proceedings of Plug-in Hybrid Electric Truck Workshop, Hybrid Truck Users Forum, Loas Angeles, Calofirnia,* 2007.
[47] Zhang Bin, Fang Pin and Xu Guoqing, "Simulation of hybrid electric truck and plug-in hybrid electric truck based on ADVISOR," in *Integration Technology, 2007. ICIT '07. IEEE International Conference on,* 2007, pp. 455-458.
[48] S. Onoda and A. Emadi, "PSIM-based modeling of automotive power systems: conventional, electric, and hybrid electric vehicles," *Vehicular Technology, IEEE Transactions on,* vol. 53, pp. 390-400, 2004.

[49] S. Onoda, S. M. Lukic, A. NAsiri and A. Emadi, "A PSIM-based modeling tool for conventional, electric, and hybrid electric vehicles studies," in *Vehicular Technology Conference, 2002. Proceedings. VTC 2002-Fall. 2002 IEEE 56th*, 2002, pp. 1676-1680 vol.3.

[50] Jun Hou and Xuexun Guo, "Modeling and simulation of hybrid electric vehicles using HEVSIM and ADVISOR," in *Vehicle Power and Propulsion Conference, 2008. VPPC '08. IEEE*, 2008, pp. 1-5.

[51] A. C. Baisden and A. Emadi, "ADVISOR-based model of a battery and an ultra-capacitor energy source for hybrid electric vehicles," *Vehicular Technology, IEEE Transactions on*, vol. 53, pp. 199-205, 2004.

[52] T. Markel and K. Wipke, "Modeling grid-connected hybrid electric vehicles using ADVISOR," in *Applications and Advances, 2001. the Sixteenth Annual Battery Conference on*, 2001, pp. 23-29.

[53] A. I. Antoniou, J. Komyathy, J. Bench and A. Emadi, "Modeling and Simulation of Various Hybrid-Electric Configurations of the High-Mobility Multipurpose Wheeled Vehicle (HMMWV)," *Vehicular Technology, IEEE Transactions on*, vol. 56, pp. 459-465, 2007.

[54] M. J. Tavernini, B. A. Niemoeller and P. T. Krein, "Real-time low-level simulation of hybrid vehicle systems for hardware-in-the-loop applications," in *IEEE Vehicle Power and Propulsion Conference*, 2009, pp. 890-895.

[55] F. U. Syed, M. L. Kuang, J. Czubay and Hao Ying, "Derivation and Experimental Validation of a Power-Split Hybrid Electric Vehicle Model," *IEEE Transactions on Vehicular Technology*, vol. 55, pp. 1731-1747, November, 2006.

[56] L. Guzzella and C. H. Onder, *Introduction to Modeling and Control of Internal Combustion Engine Systems.* (2nd ed.) Springer, 2010.

[57] H. B. Pacejka, *Tyre and Vehicle Dynamics.* (2nd ed.) Oxford: Butterworth-Heinemann, 2006.

[58] O. Tremblay and L. Dessaint, "Experimental Validation of a Battery Dynamic Model for EV Applications," *Word Electric Vehicle Journal*, vol. 3, May, 2009.

[59] M. Durr, A. Curden, S. Gair and J. R. McDonald, "Dynamic model of a lead acid battery for use in a domestic fuel cell system," *Journal of Power Sources*, vol. 161, pp. 1400-1411, October, 2006.

[60] Min Chen and G. A. Rincon-Mora, "Accurate, Compact, and Power-Efficient Li-Ion Battery Charger Circuit," *IEEE Transactions on Circuits and Systems II: Express Briefs*, vol. 53, pp. 1180-1184, November, 2006.

[61] C. Shepherd M., "Design of Primary and Secondary Cells, Part 2. An equation describing battery discharge," *Journal of Electrochemical Society*, vol. 112, pp. 657-664, July, 1965.

[62] O. Tremblay, L. -. Dessaint and A. -. Dekkiche, "A generic battery model for the dynamic simulation of hybrid electric vehicles," in *The Proceedings of IEEE Vehicle Power and Propulsion Conference*, 2007, pp. 284-289.

[63] V. Rajagopalan, *Computer-Aided Analysis of Power Electronic Systems.* CRC Press, 1987.

[64] P. C. Krause, O. Wasynczuk, S. D. Sudhoff and P. C. Krause, *Analysis of Electric Machinery and Drive Systems.* (2nd ed.) New York: IEEE Press, 2002.

[65] R. Krishnan, *Electric Motor Drives : Modeling, Analysis, and Control.* Upper Saddle River, N.J.: Prentice Hall, 2001.

[66] M. Salman, N. J. Schouten and N. A. Kheir, "Control strategies for parallel hybrid vehicles," in *In Proceedings of the American Control Conference,* 2000, pp. 524-528 vol.1.

[67] N. J. Schouten, M. A. Salman and N. A. Kheir, "Energy management strategies for parallel hybrid vehicles using fuzzy logic," *Control Engineering Practice,* vol. 11, pp. 171-177, February, 2003.

[68] S. Cho, K. Ahn and M. L. Jang, "Efficiency of the planetary gear hybrid powertrain," in *Proceedings of the Institution of Mechanical Engineers, Part D (Journal of Automobile Engineering),* 2006, pp. 1445-1454.

[69] J. -. Park, Y. -. Park and J. -. Park, "Optimal power distribution strategy for series-parallel hybrid electric vehicles," in *Proceedings of the Institution of Mechanical Engineers, Part D (Journal of Automobile Engineering),* 2008, pp. 989-1000.

[70] D. W. Gao, C. Mi and A. Emadi, "Modeling and simulation of electric and hybrid vehicles," in *Proceedings of the IEEE,* 2007, pp. 729-745.

[71] Li Meng-liang, Wang Ling-hui, Qin Kong-jian, Du Qian and Xu Da, "Heavy-duty hybrid vehicle emission contrast research under different modes," in *Proceedings of the IEEE Vehicle Power and Propulsion Conference,* 2008, pp. 1-3.

[72] Di Wu and S. S. Williamson, "A novel design and feasibility analysis of a fuel cell plug-in hybrid electric vehicle," in *Proceedings of the IEEE Vehicle Power and Propulsion Conference,* 2008, pp. 1-5.

[73] S. Filizadeh, A. M. Gole, D. A. Woodford and G. D. Irwin, "An Optimization-Enabled Electromagnetic Transient Simulation-Based Methodology for HVDC Controller Design," *IEEE Transactions on Power Delivery,* vol. 22, pp. 2559-2566, October, 2007.

[74] J. Van Mierlo and G. Maggetto, "Innovative iteration algorithm for a vehicle simulation program," *IEEE Transactions on Vehicular Technology,* vol. 53, pp. 401-412, March, 2004.

[75] Y. Liu, M. Steurer and P. Ribeiro, "A novel approach to power quality assessment: real time hardware-in-the-loop test bed," *IEEE Transactions on Power Delivery,* vol. 20, pp. 1200-1201, April, 2005.

[76] R. Kuffel, J. Giesbrecht, T. Maguire, R. P. Wierckx and P. McLaren, "RTDS-a fully digital power system simulator operating in real time," in *Proceedings of the International Conference on Energy Management and Power Delivery,* 1995, pp. 498-503.

[77] S. Chiniforoosh, J. Jatskevich, A. Yazdani, V. Sood, V. Dinavahi, J. A. Martinez and A. Ramirez, "Definitions and Applications of Dynamic Average Models for Analysis of Power Systems," *IEEE Transactions on Power Delivery,* vol. 25, pp. 2655-2669, October, 2010.

[78] S. S. Williamson, A. Emadi and K. Rajashekara, "Comprehensive efficiency modeling of electric traction motor drives for hybrid electric vehicle propulsion applications," *IEEE Transactions on Vehicular Technology,* vol. 56, pp. 1561-72, May, 2006.

[79] M. Etezadi-Amoli, K. Choma and J. Stefani, "Rapid-Charge Electric-Vehicle Stations," *IEEE Transactions on Power Delivery,* vol. 25, pp. 1883-1887, July, 2010.

[80] J. C. Gomez and M. M. Morcos, "Impact of EV Battery Chargers on the Power Quality of Distribution Systems," *IEEE Transactions on Power Delivery,* vol. 22, pp. 63-981, December, 2002.

[81] S. Rahman and G. B. Shrestha, "An investigation into the impact of electric vehicle load on the electric utility distribution system," *IEEE Transactions on Power Delivery,* vol. 8, pp. 591-597, Apil, 1993.

[82] J. G. Ciezki and R. W. Ashton, "Selection and stability issues associated with a navy shipboard DC zonal electric distribution system," *IEEE Transactions on Power Delivery,* vol. 15, pp. 665-669, April, 2000.

[83] Kejun Qian, Chengke Zhou, M. Allan and Yue Yuan, "Modeling of Load Demand Due to EV Battery Charging in Distribution Systems," *IEEE Transactions on Power Systems,* vol. 26, pp. 802-810, May, 2011.

[84] W. Di, D. C. Aliprantis and K. Gkritza, "Electric Energy and Power Consumption by Light-Duty Plug-In Electric Vehicles," *IEEE Transactions on Power Systems,* vol. 26, pp. 738-746, May, 2011.

[85] L. Pieltain Fernández, T. Gómez San Román, R. Cossent, C. M. Domingo and P. Frías, "Assessment of the Impact of Plug-in Electric Vehicles on Distribution Networks," *IEEE Transactions on Power Systems,* vol. 26, pp. 206-213, February, 2011.

[86] K. Clement-Nyns, E. Haesen and J. Driesen, "The Impact of Charging Plug-In Hybrid Electric Vehicles on a Residential Distribution Grid," *IEEE Transactions on Power Systems,* vol. 25, pp. 371-380, February, 2010.

[87] A. Davoudi, J. Jatskevich, P. L. Chapman and A. Khaligh, "Averaged-Switch Modeling of Fourth-Order PWM DC–DC Converters Considering Conduction Losses in Discontinuous Mode," *IEEE Transactions on Power Electronics,* vol. 22, pp. 2410-2415, November, 2007.

[88] A. Davoudi, J. Jatskevich and T. De Rybel, "Numerical state-space average-value modeling of PWM DC-DC converters operating in DCM and CCM," *IEEE Transactions on Power Electronics,* vol. 21, pp. 1003-1012, July, 2006.

[89] Sung-Soo Hong and Byungcho Choi, "Technique for developing averaged duty ratio model for DC-DC converters employing constant on-time control," *Electronics Letters,* vol. 36, pp. 397-399, March, 2000.

[90] E. Van Dijk, J. N. Spruijt, D. M. O'Sullivan and J. B. Klaassens, "PWM-switch modeling of DC-DC converters," *IEEE Transactions on Power Electronics,* vol. 10, pp. 659-665, November, 1995.

[91] H. Kanaan, K. Al-Haddad and F. Fnaiech, "Modelling and control of three-phase/switch/level fixed-frequency PWM rectifier: State-space averaged model," in *IEE Proceedings of Electric Power Applications*, 2005, pp. 551-557.

[92] Wei Keyin, Liu Dezhi, Ou Yangbing, Zhai Xiaofei and Yan Ming, "State-space average-value model of 3-phase 4-wire diode-bridge rectifier," in *IEEE International Symposium on Industrial Electronics, 2009*, 2009, pp. 1634-1638.

[93] K. Corzine, Xiaomin Kou and J. R. Baker, "Dynamic average-value modeling of a four-level drive system," *IEEE Transactions on Power Electronics*, vol. 18, pp. 619-627, March, 2003.

[94] Jian Sun, D. M. Mitchell, M. F. Greuel, P. T. Krein and R. M. Bass, "Averaged modeling of PWM converters operating in discontinuous conduction mode," *IEEE Transactions on Power Electronics*, vol. 16, pp. 482-492, July, 2001.

[95] Jian Sun and H. Grotstollen, "Symbolic analysis methods for averaged modeling of switching power converters," *IEEE Transactions on Power Electronics*, vol. 12, pp. 537-546, May, 1997.

[96] P. T. Krein, J. Bentsman, R. M. Bass and B. L. Lesieutre, "On the use of averaging for the analysis of power electronic systems," *IEEE Transactions on Power Electronics*, vol. 5, pp. 182-190, April, 1990.

[97] R. W. Erickson and D. Maksimović, *Fundamentals of Power Electronics.* (2nd ed.) Norwell, Mass.: Kluwer Academic Publishers, 2001.

[98] S. Akkihal and M. W. Thompson, "Generalized switched inductor model (GSIM): accounting for conduction losses," *IEEE Transactions on Aerospace and Electronic Systems*, vol. 38, pp. 681-687, April, 2002.

[99] D. Czarkowski and M. K. Kazimierczuk, "Energy-conservation approach to modeling PWM DC-DC converters," *IEEE Transactions on Aerospace and Electronic Systems*, vol. 29, pp. 1059-1063, July, 1993.

[100] M. Heidari, S. Filizadeh and A. M. Gole, "Support Tools for Simulation-Based Optimal Design of Power Networks With Embedded Power Electronics," *Power Delivery, IEEE Transactions on*, vol. 23, pp. 1561-1570, 2008.

[101] W. Gao and C. Mi, "Hybrid Vehicle Design Using Global Optimization Algorithms," *International Journal on Electric and Hybrid Vehicles*, vol. 1, pp. 57-70, July, 2007.

[102] Bin Wang, Xinzhou Dong, Zhiqian Bo, A. Klimek, B. Caunce, A. Perks, B. Smith and L. Denning, "RTDS environment development of ultra-high-voltage power system and relay protection test," in *IEEE Power Engineering Society General Meeting*, 2007, pp. 1-7.

[103] Em Poh Ping, K. Hudha, M. H. B. Harun and H. Jamaluddin, "Hardware-in-the-loop simulation of automatic steering control: Outer-loop and inner-loop control design," in *Proceedings of 11th International Conference on Control Automation Robotics & Vision*, 2010, pp. 964-969.

[104] D. Michalek, C. Gehsat, R. Trapp and T. Bertram, "Hardware-in-the-loop-simulation of a vehicle climate controller with a combined HVAC and passenger

compartment model," in *Proceedings of International Conference on Advanced Intelligent Mechatronics*, 2005, pp. 1065-1070.

[105] S. Oncu, S. Karaman, L. Guvenc, S. S. Ersolmaz, E. S. Ozturk, E. Cetin and M. Sinai, "Robust yaw stability controller design for a light commercial vehicle using a hardware in the loop steering test rig," in *IEEE Intelligent Vehicles Symposium*, 2007, pp. 852-859.

[106] "Opal-RT Website," .

[107] "K2 Energy website, [online] Available: http://www.peakbattery.com/products-26650P.html," .

[108] B. Do Valle, C. T. Wentz and R. Sarpeshkar, "An Area and Power-Efficient Analog Li-Ion Battery Charger Circuit," *IEEE Transactions on Biomedical Circuits and Systems*, vol. 5, pp. 131-137, April, 2011.

[109] Jiann-Jong Chen, Fong-Cheng Yang, Chien-Chih Lai, Yuh-Shyan Hwang and Ren-Guey Lee, "A High-Efficiency Multimode Li–Ion Battery Charger With Variable Current Source and Controlling Previous-Stage Supply Voltage," *IEEE Transactions on Industrial Electronics*, vol. 56, pp. 2469-2478, July, 2009.

[110] Liang-Rui Chen, Jin-Jia Chen, Neng-Yi Chu and Gia-Yo Han, "Current-Pumped Battery Charger," *IEEE Transactions on Industrial Electronics*, vol. 55, pp. 2482-2488, June, 2008.

[111] G. Pellegrino, E. Armando and P. Guglielmi, "An Integral Battery Charger With Power Factor Correction for Electric Scooter," *IEEE Transactions on Power Electronics*, vol. 25, pp. 751-759, March, 2010.

[112] Yuh-Shyan Hwang, Shu-Chen Wang, Fong-Cheng Yang and Jiann-Jong Chen, "New Compact CMOS Li-Ion Battery Charger Using Charge-Pump Technique for Portable Applications," *IEEE Transactions on Circuits and Systems I: Regular Papers*, vol. 54, pp. 705-712, April, 2007.

[113] M. Charkhgard and M. Farrokhi, "State-of-Charge Estimation for Lithium-Ion Batteries Using Neural Networks and EKF," *IEEE Transactions on Industrial Electronics*, vol. 57, pp. 4178-4187, December, 2010.

[114] Hongwen He, Rui Xiong, Xiaowei Zhang, Fengchun Sun and JinXin Fan, "State-of-Charge Estimation of the Lithium-Ion Battery Using an Adaptive Extended Kalman Filter Based on an Improved Thevenin Model," *IEEE Transactions on Vehicular Technology*, vol. 60, pp. 1461-1469, May, 2011.

[115] I-Hsum Li, Wei-Yen Wang, Shun-Feng Su and Yuang-Shung Lee, "A Merged Fuzzy Neural Network and Its Applications in Battery State-of-Charge Estimation," *IEEE Transactions on Energy Conversion*, vol. 22, pp. 697-708, September, 2007.

[116] Il-Song Kim, "Nonlinear State of Charge Estimator for Hybrid Electric Vehicle Battery," *IEEE Transactions on Power Electronics*, vol. 23, pp. 2027-2034, July, 2008.

[117] E. Tara and S. Filizadeh, "Modeling and simulation of a power-split gear hybrid drive-train," in *Proceedings of the 36th Annual Conference on IEEE Industrial Electronics Society*, 2010, pp. 3097-3102.

[118] E. Tara, S. Filizadeh, J. Jatskevich, E. Dirks, A. Davoudi and M. Saeedifard, "Dynamic Average-Value Modeling of Hybrid-Electric Vehicular Power Systems," *IEEE Transactions on Power Delivery,* vol. 27, pp. 430-438, January, 2012.

[119] Federal test procedure review project: Preliminary technical report. [online]. Available: http://www.epa.gov/oms/regs/ld-hwy/ftp-rev/ftp-tech.pdf.

[120] Anonymous Using global positioning system travel data to access real world energy use of plug in hybrid electric vehicles. Available: http://www.nrel.gov/docs/fy07osti/40858.pdf.

[121] B. Y. Liaw and M. Dubarry, "From driving cycle analysis to understanding battery performance in real-life electric hybrid vehicle operation," *Journal of Power Sources,* vol. 174, pp. 76-88, November, 2007.

[122] A. Froberg and L. Nielsen, "Efficient drive cycle simulation," *IEEE Transactions on Vehicular Technology,* vol. 57, pp. 1442-53, May, 2008.

[123] Q. Gong, Y. Li and Z. Peng, "Trip-based optimal power management of plug-in hybrid electric vehicles," *IEEE Transactions on Vehicular Technology,* vol. 57, pp. 3393-3401, November, 2008.

[124] W. Hung, K. Tam, C. Lee, L. Chan and C. Cheung, "Comparison of driving characteristics in cities of Pearl River Delta, China," *Atmospheric Environment,* vol. 39, pp. 615-625, February, 2005.

[125] E. Milkins and H. Watson, "Comparison of urban driving patterns," in *Proceedings of the Motor Vehicle Technology: Progress and Harmony (2nd International Pacific Conference on Automotive Engineering).* 1983, pp. 735-745.

[126] T. C. Austin, F. J. DiGenova, T. R. Carlson, R. W. Joy, K. A. Gianolini and J. M. Lee, *Characterization of Driving Patterns and Emissions from Light-Duty Vehicles in California.* The Division, 1993.

[127] S. J. Chapman, *Electric Machinery Fundamentals.* (2nd ed.) New York: McGraw-Hill, 1991.

[128] R. H. Park, "Two-reaction theory of synchronous machines generalized method of analysis-part I," *Transactions of the American Institute of Electrical Engineers,* pp. 12-727, July, 1929.